Short Circuit Protection of Microgrids Integrating Inverter-Based Distributed Energy Resources

Ehsan Dehghanpour

Department of Electrical and Computer Engineering

McGill University, Montreal, Quebec

September 2023

First published on 9th December 2024

A thesis submitted to McGill University in partial fulfillment of the requirements of the degree of Doctorate of Philosophy in Electrical Engineering.

Abstract

By utilizing distributed renewable energy resources, Microgrid is considered as an alternative to solve the energy crisis and decrease carbon dioxide emissions. Recently, inverters are employed as the interface between the distributed energy resources (DER) and the electric grid. Employing Inverters can improve the controllability of DERs. However, inverter-based resources are different from conventional synchronous generators; inverters adopt different control schemes which make their fault current analysis and estimation more complex; inverters have limited fault current. Moreover, the fault current magnitude varies significantly when a microgrid transfers from the grid-connected mode to the island mode of operation; because of the mentioned features the fault detection and protection of the microgrids that include inverter-based distributed resources is challenging.

This thesis proposes a protection scheme for microgrids integrating inverter-based DERs which detects different types of faults including impedance faults in the microgrid in both operating modes. Firstly, two parameters named voltage phase angle shift and *D* parameter are introduced for fault detection. Then, by using the proposed parameters, a fault detection element is proposed. In addition to fault detection, determination of the fault current direction is essential to have selective protection. Because of the inverters' specific fault current characteristics, conventional directional elements may maloperate in the presence of inverter-based DER in a microgrid. Therefore, a directional element is introduced in this thesis to determine the current direction during fault. The proposed directional element determines the fault current direction based on the current phase angle shift.

In addition to fault detection and directional elements, a coordination element and a backup protection element are also proposed in this thesis to have a coordinated protection scheme that can provide backup protection in case of primary relay's breaker failure or communication loss. Then, it is explained how the proposed elements are working together as a protection relay, and the protection scheme implemented by the proposed relay is introduced.

The performance of the proposed scheme is evaluated by simulating different scenarios in different microgrid configurations. The results are also verified through Controller Hardware In the Loop setup. The obtained results confirm the high performance of the proposed protection scheme in microgrids.

Résumé

Les onduleurs construits en utilisant l'électronique de puissance sont utilisés comme interface pour les sources d'énergie renouvelable distribuées (DER) afin d'améliorer la contrôlabilité de ces sources d'énergie. Cependant, ces sources, utilisant des onduleurs, ne se comportent pas comme des générateurs synchrones classiques ; les onduleurs contrôlables peuvent adopter différents modes de contrôle, ce qui rend complexe l'analyse des courants de défauts et l'estimation de leur amplitude; de plus, ils ont aussi un courant de défaut plutôt limité. La détection des défauts et la protection des microréseaux deviennent alors plus difficiles à gérer. Ainsi, la protection utilisée pour les ressources distribuées basées sur des onduleurs ne peut être faite aussi aisément.

Cette thèse propose une méthode de protection pour les microréseaux qui détecte différents types de défauts, y compris les défauts de haute impédance dans le microréseau, et ceci, dans les modes reliées au réseau ou en mode autonome. Tout d'abord, on introduit deux paramètres: le décalage d'angle de phase de tension, ainsi que le paramètre D utilisés pour la détection des défauts. Ensuite, en utilisant les paramètres proposés, une méthode de détection de défaut est proposée. En plus de la détection de défaut, la détermination du sens du courant de défaut est essentielle afin d'avoir une protection sélective. Étant donné que les éléments directionnels conventionnels opèrent mal dans le cas des microréseaux en raison des caractéristiques de courant de défaut spécifiques des onduleurs, un élément directionnel est introduit dans cette thèse pour déterminer la direction du courant pendant le défaut. L'élément directionnel proposé détermine la direction du courant de défaut en fonction du décalage d'angle de phase du courant.

En plus des éléments de détection de défaut et d'éléments directionnels, un élément de coordination ainsi qu'un élément de protection de secours sont également proposés dans cette thèse afin d'obtenir un mode de protection coordonné qui peut fournir une protection de secours en cas de défaillance du disjoncteur, du relais primaire, ou lors d'une perte de communication. Ensuite, on explique comment les éléments proposés fonctionnent ensemble en tant que relais de protection. Le mode de protection mis en œuvre par le relais proposé est présenté.

La performance du mode de protection proposé est évaluée par la simulation de différents scénarios pour différentes configurations de microréseaux. Les résultats sont également vérifiés par le matériel du contrôleur dans la configuration de la boucle. Les résultats obtenus confirment la haute performance de ce mode de protection proposé pour les microréseaux à onduleurs.

Acknowledgments

First of all, I would like to express my deep appreciation and gratitude to my supervisor Professor Geza Joos for his effective guidance, patient instructions, and stringent requirements during my Ph.D. study. His insightful and thought-provoking comments always provide inspiring ideas. Meanwhile, I really appreciate all the opportunities he gave me to participate in projects and share ideas with other people.

I would like to thank my supervisory committee members including Prof. Geza Joos, Prof. Xiaozhe Wang, and Prof. James Richard Forbes for their valuable insights into my research work. Some of their ideas opened the door to a new perspective for me. I am also thankful to Mr. Michel Normandeau from Hydro-Qu´ebec Research Institute. His kindness, constructive feedbacks, and practical suggestions expedited the progress of my research. I wish to also thank Mr. Yves Brissette from IREQ for his help in the first stage of my Ph.D.

Moreover, the following financial support is acknowledged: the McGill Engineering Doctoral Award, and the NSERC/Hydro-Quebec Industrial Research Chair on the Integration of Renewable Energies and Distributed Generation into the Electric Distribution Grid. These supports have helped me during my research from September 2018 to Dec. 2022, and I am thankful for their support.

I would also like to convey my gratitude to all my lab mates at McGill University for the great time we shared. For brevity, I cannot list their names here. I want to thank the staff at the Electrical and Computer Engineering Department for helping me smoothly complete the Ph.D. program.

I would like to dedicate the dissertation to my father, my mother, and my brother. None of this would have been possible without their constant love and encouragement, and I cannot emphasize enough how important their support has been to me.

Original Contributions

The contribution of this dissertation provides the original solutions for protecting microgrids that include inverter-based distributed energy resources. As shown in the referenced peer-reviewed papers, the main contributions of the thesis are highlighted below:

- Two parameters named voltage Phase Angle Shift (*PAS*) and *D* parameters are introduced, and a fault detection method is presented. The method detects the fault by measuring the *PAS* and *D* parameters and employing a new relay characteristic. The *PAS* parameter is a shift in the voltage phase angle following a fault which is mainly caused by three factors: (a) the active power and reactive power variation following a fault and their effects on frequency and voltage levels, (b) the variation in the *X/R* ratio between the source and the faulted feeder, and (c) the transformation of the sag to lower voltage levels as a result of a fault. The *D* parameter is defined as the difference between the predicted and the actual current samples.

- A method to determine the fault current direction in microgrids integrating inverter-based distributed energy resources is introduced, after demonstrating the problems with conventional directional elements in microgrids. The method determines the fault current direction based on a new parameter named current phase angle shift (*CPS*) and the direction of the current before the fault.

Preface and Contributions of the Author

The research presented in this dissertation was carried out in the Department of Electrical and Computer Engineering (ECE) of McGill University under the supervision of prof. Geza Joos. The main contributions by the candidate involve identifying problems, proposing solutions, executing software simulations, executing hardware in-the-loop validations, compiling results, and composing the thesis article. The publications from this thesis and the contributions of the co-authors are listed below.

Journal Paper:

1. E. Dehghanpour, M. Normandeau, G. Joós and Y. Brissette, "A Protection System for Inverter Interfaced Microgrids," in *IEEE Transactions on Power Delivery*, vol. 37, no. 3, pp. 2314-2325, June 2022, [1]

Mr. Michel Normandeau contributed by giving technical comments on the paper. Prof. Geza Joos is responsible for supervisory guidance to the candidate. Mr. Yves Brissette contributed by giving technical comments on the paper.

Conference Paper

1. E. Dehghanpour, M. Normandeau and G. Joos, "Protection of Inverter Interfaced Microgrids: Challenges and Solutions," 2022 IEEE/PES Transmission and Distribution Conference and Exposition (T&D), 2022, pp. 1-4, [2]

Mr. Michel Normandeau contributed by giving technical comments on the paper. Prof. Geza Joos is responsible for supervisory guidance to the candidate.

Table of Contents

List of Figures

List of Tables

List of Acronyms

3P	3 Phase fault
AC cycle	Alternating Current cycle (0.016 sec)
AI	Artificial Intelligence
BES	Battery Energy Storage
BF	Bolted Fault
C-HIL	Controller-Hardware In the Loop
CPS	Current Phase Shift
CTI	Coordination Time Interval
DER	Distributed Energy Resource
DG	Distributed Generation
DOR	Directional Overcurrent Relay
FCL	Fault Current Limiter
FPGA	Field-Programmable Gate Array
IBR	Inverter-Based Resource
IED	Intelligent Electronic Device
IF	Impedance Fault
I/O	Input/Output
MD	Mahalanobis Distance
PCC	Point of Common Coupling
PAS	voltage Phase Angle Shift
PG	Phase to Ground fault
PP	Phase to Phase fault
PPG	Phase to Phase to Ground fault
SCC	Short Circuit Capacity

SG	Synchronous Generator
SNR	Signal-to-Noise Ratio
VF	Voltage-Frequency

Chapter 1

Introduction

Power system protection is crucially important for the operation of the power system as it protects personal safety and power equipment. If a short circuit fault occurs in the system, the protection system must be able to detect the fault, determine the fault zone, and remove it from the system so that the system remains stable and continues its normal operation after the fault. To provide a reliable and continuous power supply, efforts are being made to improve protection devices in terms of their speed, sensitivity, security, and selectivity. Nowadays integration of renewable energy resources into the distribution system as a solution to reduce carbon dioxide emissions has attracted a lot of attention. Integration of renewable energy resources into the distribution system has made fault detection and protection of the distribution system a rigorous task [3], [4].

This thesis is seeking an innovative technique for short circuit protection of active distribution systems, in particular microgrids integrating inverter-based resources. In this chapter, some background information on microgrids and a literature review on the current microgrid fault detection methods are presented. Then the problem statement and the original contributions of the thesis are briefly discussed.

1.1 Research Background

1.1.1 Microgrid

Microgrid is defined as a group of interconnected loads and Distributed Energy Resources (DERs) with clearly defined electrical boundaries that acts as a single controllable entity with respect to the grid and can connect and disconnect from the grid to enable it to operate in both grid-connected and island modes [5]. Microgrid is a good solution to utilize renewable energies such as solar energy, wind power, etc., and is considered as an alternative to solve the energy crisis and decrease carbon dioxide emissions [6], [7]. A typical microgrid is demonstrated in Figure 1-1. The microgrid has specific features making it different from the traditional distribution network. Unlike

Figure 1-1: Typical microgrid

traditional distribution systems, Distributed Generators (DGs) are connected to different buses in microgrids, and this practice makes the power flow bi-directional. This means the power flow direction is not just from the transmission lines to the distribution system; the power-flow direction can be from the microgrid to the transmission lines as well. The bi-directional power flow can result in a bi-directional current during fault conditions which directly affects the fault detection process. The current that passes through the lines during a short circuit fault is referred to as fault current. In a microgrid, the fault current is large in the grid-connected mode as compared to the island mode [8], [9]. Compared with the traditional distribution systems which are mostly radial, microgrids can have diverse network configurations including radial, looped, and meshed [10].

1.1.2 Integrating Inverter-based DERs in Microgrids

Nowadays, inverters are employed as an interface between the microgrid and the DER [11]. Inverter is a power electronic device that converts direct current to alternating current or vice versa. Inverters are used to improve the controllability of DERs [12].

Inverter-based DERs have some features that are mostly related to the use of the inverter in the system. These features include inconsistent behavior under fault conditions, limited kinetic energy, and inconsistent transient behavior [13]. The control functions of inverter-based DGs are different from those of Synchronous Generators (SG) in terms of speed and mechanism, and because of adopting different control schemes, inverters' fault current analysis and estimation is more complex [14]. In other words, the behavior of SGs under fault conditions can be modeled as a voltage source in series with an impedance. However, the behavior of inverter-based DGs under fault conditions can be different depending on the control system of the inverter and its manufacturer [13]–[15].

Because of the presence of power electronic devices and low inertial time constant, inverters' response time is much faster than SGs [13]. Owing to their fast speed, the controllers of an inverter-based DG react quickly to faults and affect its response depending on the severity of faults [12]. The first major difference between an inverter-based DG and SG is the inverters' current control loop that limits the fault current to 1.5 to 2 times its nominal current (per unit[1]) [16], [17]. This fault current magnitude is very close to the nominal current, and it can be lower than 1.5 per unit depending on the current control loop [18]. Due to the fast response of power electronic interfaces, this limitation applies within two alternating current cycles (within 32 milliseconds). During these two cycles, current waveforms typically have high-frequency transients. Therefore, inverters cannot be considered as linear sources in a faulted microgrid. Another major difference is that inverters can operate in any desired power factor while working in normal or faulted conditions [19]. Typically, the inverters work with a unity power factor, but the power factor can be changed during fault and ride-through[2] conditions. This causes the phase of the inverter's fault current to be different from the SG's fault current. This is important because conventional protection methods are designed based on the SG's behavior under fault conditions; conventional directional elements in particular relay on the fault current phase angle to determine the fault zone. Besides, the inverters are usually ungrounded and, in most cases, only generate positive sequence currents even during unbalanced faults [4], [20].

1.1.3 Protection Challenges with Inverter-based DERs

This section discusses some of the main challenges in the protection of microgrids integrating inverter-based DERs. One of the protection challenges in such microgrids is the inability of

[1] "Per unit (pu)" is a method used to represent the magnitude of a quantity in terms of a reference or base quantity; here, the based quantity is the nominal current of the device or the system.

[2] Fault ride-through (or Low Voltage Ride-Through- LVRT) is the ability of electric generator to remain connected during short periods of lower electric network voltage such as fault consitions.

inverters to provide a high-magnitude current in case of a fault in the system. This is problematic because most conventional protection schemes rely on high-magnitude fault current to detect the fault. As an illustration, consider the microgrid shown in Figure 1-2. The nominal current in the system is considered to be 1 pu. If a three-phase fault is applied at point F2 in the system in the island mode of operation, the fault current magnitude is about 2 pu for one AC cycle after the fault occurrence; then, it is limited to about 1 pu. This is because the control system of the inverter limits the fault current to protect the power electronic switches of the inverter. The issue still exists for the microgrid side relays in the grid-connected mode. For example, when a fault occurs at point F1 in the grid-connected mode of operation, the fault currents measured by relays R8, R6, and R4 are still limited because relays R8, R6, and R4 only see the current coming from DG2. Therefore, it is not possible to differentiate the normal events in the system such as switching events and overload conditions from the fault conditions based on the current magnitude in the microgrid [2].

Employing under-voltage protection may seem a reasonable practice to detect the fault in a microgrid at first glance. This is due to a significant voltage drop expected following a fault in the microgrid. Since microgrids have short lines as compared to transmission lines, the voltage drop is not significantly different throughout the different lines under fault conditions. This makes distinguishing the faulty line and coordinating the primary relay and backup relay unfeasible. Apart from the protection coordination problems associated with under-voltage protection especially in microgrids that usually have short lines, under-voltage protection is not able to detect the impedance faults in the microgrid [2] [21]. The protection system must be able to detect the fault with the minimum fault current. This minimum fault current value is not a bolted fault

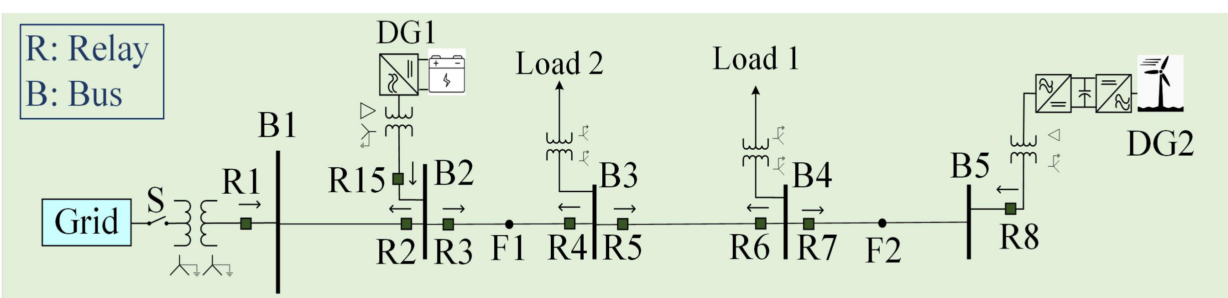

Figure 1-2: Microgrid

calculation since there is always an impedance in the fault path. The minimum fault impedance is usually calculated using some stated values of fault impedance, and it is assumed to be pure resistance (R_f) [22], [23]. If the fault resistance could be measured in a large variety of fault situations the value would be found to be statistically distributed over a wide range [22], [23]. A study conducted in [24] on 1375 faults on various 26kV to 220 kV systems states that the faults with the apparent fault resistance ranging from 5 to 25 ohms are the most frequently occurring faults., A rural electrification administration bulletin [25] recommends using 40 ohms for R_f in minimum line-to-ground fault calculations. These studies can be applied to microgrids as well since microgrids are essentially medium voltage distribution systems that integrate distributed energy resources [8]. Therefore, Rf=40 ohms is used as the designed criteria in this thesis. As mentioned, under-voltage protection is not able to detect impedance faults in the microgrid. For example, the voltage magnitudes measured by relay R8 in the system shown in Figure 1-2 will be above 0.95 percent of the nominal voltage following the fault when an impedance phase to ground fault with $R_f = 40$ ohms occurs at point F2 in the grid-connected mode; consequently, the under-voltage protection cannot detect the fault.

In addition to overcurrent and under voltage based protections, negative sequence-based protections [26] may also be ineffective to detect the fault in microgrids. It is because inverter-based DERs operate as current control resources, and a generic voltage source converter control system usually suppresses negative sequence current. As an illustration, the negative sequence current magnitude measured by relay R8 following a bolted phase to ground fault at point F2 is negligible in the grid-connected mode because inverter interfaced DG2 does not generate any negative sequence current following a fault, and it is not possible to detect the fault by measuring the negative sequence current in this case [2].

Moreover, the directional element is an integral part of the protection of any system with bi-directional fault currents including microgrids [27], [28]–[30]. The directional element determines the fault current direction and enables the relay to operate for forward faults. This is shown in Figure 1-2 through a vector above each relay. For example, for a fault at point F1, relays R3 and R4 are the primary relays and should operate first; R1 is the backup relay for R3, and R6 is the backup relay for R2. The backup relay will operate in case the primary relay does not respond to the fault. However, R2 should not operate for a fault at F1 since the fault current is in the backward direction for R2 when a fault occurs at F1; this will be determined by the directional element. The directional element is a basic prerequisite for selective protection in a non-unit relaying scheme. Traditional directional elements including negative sequence, positive sequence, and phase directional elements are all prone to malfunction in microgrids in the presence of inverter-based DERs. Inverters have no negative sequence current, and a generic current control loop of the inverter does not regulate the negative sequence current; moreover, inverters limit the current under fault conditions. All the mentioned features lead to the malfunction of the traditional directional elements [3], [4], [31], [32]; it is because they are designed based on the behavior of synchronous generators. Since the inverter-based resources act differently under fault conditions, the presence of inverter-based resources in the system can cause the malfunction of these elements.

1.1.4 Literature Review

This section provides a review of fault detection, calcification, and protection schemes in the microgrid. The focus of the discussion is placed on the protection challenges with the presence of inverter-based distributed generation in microgrids.

In [16], a negative-sequence resistance-based fault detection approach to detect the fault in the islanded microgrid is proposed, but the method only detects faults in the island mode of operation. Fault detection and classification schemes for the microgrid based on the wavelet transform and deep neural network are presented in [33], [34]. In [35], [36], a combined wavelet analysis and data mining-based approaches are proposed to detect faults in the microgrid. The combination of wavelet transform and differential faulty energy has been used in [37] for microgrid fault detection. Fault detection and classification based on the wavelet transform are also presented in [38]–[40]. In [41], a fault detection and classification strategy based on AdaBoost classifier-based data mining model is presented for microgrids. Authors in [10], [42] proposed a method based on Hilbert-Huang Transform and a machine learning algorithm to detect faults in the microgrid. By using machine learning and Artificial Intelligence (AI), authors in [43] proposed an AI and support vector machine-based fault detection technique. Besides, machine learning based approaches for fault classification in microgrids are also presented in [44]–[47]. However, these methods use many branches' current measurements, and the missing data and the resolution of the training dataset can affect their performance.

A unified impedance relay for a combined ac/dc microgrid is proposed in [48], but the method requires an extra parallel LC circuit in series with the existing relay. A protection scheme introduced in [49] uses principles of synchronized phasor measurements and microprocessor relays to detect all types of fault conditions in a microgrid. The presented method is based on differential protection, and it relies on communication. Also, a comprehensive digital protection scheme for low-voltage microgrids is presented in [50]. For line and feeder protection, a differential protection unit is proposed that is based on the information on two sides of the line. Hybrid adaptive protection schemes based on differential principles are also presented in [28], [51]–[61]. Because of its nonsusceptibility to bidirectional power flow, the number of DGs in the microgrid, the differential protection principle may meet the requirements to protect the microgrid. However, differential protection relies on high-bandwidth communication to detect the fault, and a relay is required at every node of the protection zone. The system also needs to be equipped with local backup relays, such as directional overcurrent and distance relays, which increases the implementation cost [4], [60], [62].

A centralized microgrid protection is presented in [63]. In this method, if any change happens in the microgrid, the overcurrent relays' setting will be reset. In [64], an adaptive multiagent approach for industrial power distribution systems is proposed. In this method, different agent groups including DG agents, relay agents, and equipment agents are defined. In [65], adaptive protection coordination in active distribution networks is presented. In the method presented in [65], several over-current relay settings are obtained offline for several possible configurations. Then, all these settings will be stored in the overcurrent device called an intelligent electronic device. Also, a centralized controller, installed at the substation with IEC 61850-based communications, is considered which checks the status of the switches and DGs and determines a new setting group for overcurrent relays. The methods presented in [63]–[65] require an extensive communication platform which has a high implementation cost.

A multi-agent-based scheme for fault diagnosis in power distribution networks with distributed generators is proposed in [66]. In the proposed scheme, the distribution network is divided into several network segments, where each network segment can be isolated from the rest of the system in case that a fault occurs inside the segment. In [67], the authors proposed a protection scheme based on an integrated impedance angle; the method uses wide-area positive sequence components of voltages and currents to detect the faults. In [68], an agent-based protection scheme is presented for distribution networks. In this method, Clarke components of the fault currents and their wavelet coefficients are used to determine fault direction. In this paper, the distribution system is divided into different segments for fault isolation purposes. It also proposed a flowchart for fault segment location. A communication-based dual-setting relay protection scheme is introduced in [9]. In this scheme, a dual-setting relay is used to protect the microgrid in both modes of operation. In addition, low bandwidth communication is used to coordinate backup and primary relays. The proposed scheme decreases the total operating time of DORs and eliminates the need for FCL. In [69], techniques for making a multi-function monitor-style protection system aware of the operation of “healthy” loads are presented. It permits to adapt protection thresholds and detects difficult-to-identify faults. The proposed monitoring techniques help to identify faulted zones. Although some of the methods presented in [66]–[69] use low bandwidth communication and consider the communication failure scenario, they did not investigate the performance of the proposed methods in a microgrid with inverter-based DERs.

Protection issues of LV microgrids are explained in [70], and a new LV-microgrid protection concept is developed. The paper discusses the fundamental properties of future LV-microgrid protection which include: 1) adaptation capability and 2) utilization of high-speed communication. The paper also explained the operation curve of protection devices in LV microgrids. Architectures and concepts for future electric energy systems are reviewed in [71]; important automation architectures, smart devices, control concepts, energy management principles enabling intelligence, decentralization, robustness in the field of future electric energy systems, and involved components are discussed in this paper. As claimed in [71], the most important functions and services of a smart grid include: advanced monitoring and diagnostics, optimization/self-optimization capabilities, automatic grid (topology) reconfiguration, adaptive protection, distributed power system management, islanding possibilities/microgrids, distributed generation/distributed energy resources with ancillary services, demand response/energy management support, advanced forecasting support, self-healing and asset management/condition-dependent power system maintenance.

In [72], an adaptive overcurrent protection scheme is presented. In this method, the relay setting is adapted by the knowledge of DER status and the average load line estimate. It should be mentioned that this scheme cannot be implemented with available protection devices; moreover, it uses a differential method that requires communication between relays. In [73], a communication-assisted overcurrent protection scheme is presented to protect the microgrid; it needs a central protection unit to update relay settings based on configuration changes. Overcurrent-based methods are also presented in [74]–[78], but the performance of these methods has not been investigated in the presence of inverter-based DERs, and the problem associated with the limited fault current of inverter-based resources has not been addressed in these methods.

An adaptive fault detection method based on positive and negative superimposed currents is proposed in [79], [80], but the characteristic of the sequence impedance in IBRs has not been considered. In [81], a protection scheme is presented to detect faults in looped microgrids. In this scheme, the impedance of the microgrid is calculated at the output of each DER. Although this method is implemented without expensive protective devices or communication links, it is only able to detect faults in looped microgrids, and a supercapacitor energy storage system should be connected to the DC link of each inverter-based DER in case of using a renewable energy source. Authors in [82] demonstrated that the directional element in DOR may not be able to detect fault current direction because of the specific fault current properties of IBRs and introduced a new directional element to prevent the misoperation of DORs in microgrids. The issue with the directional element presented in [82] is the threshold values selection needed to detect the direction of the current. Two different methods are presented for balanced and unbalanced faults with different approaches to determine the threshold values. In addition, detailed modeling and simulation of the system are required to determine the settings. Even though the proposed directional element improves the performance of DORs, the low fault current problem still exists, preventing DORs from a fast operation.

A selectivity mechanism is proposed in [83], which is based on the location of the Intelligent Electronic Devices (IEDs) and feeder characteristics. This method is based on the use of IEDs and communication platforms which are categorized as expensive options. An adaptive protection scheme for the distribution system is developed in [84]. In this method, the system is divided into different zones. A zone is formed such that it has a reasonable balance of load and DG, and one DG in each zone works in VF mode to regulate frequency and voltage. These zones should be separated by breakers. When a fault occurs, the faulted zone will be separated from other zones and the DG in the faulted zone will also be disconnected from the grid. The problem with this method is that separating the distribution system into different zones with balance generation and consumption is not always possible and disconnecting the DG from the grid in case of fault is not an acceptable practice based on new standards. A communication-assisted microgrid protection relay is used in [29] to divide the microgrid into several subnetworks when a fault happens. This is done by providing a communication channel between relays. It is assumed that the subnetworks are divided such that they can operate in islands. After detecting the faulted subnetwork, the fault is cleared using a microgrid protection relay introduced in the paper. The disadvantage of this method is dividing the microgrid into subsystems, which may not always be feasible, and it affects the practicality of the proposed method.

In [85], a fault detection method is introduced that detects the fault using positive sequence voltage and current; but the method only detects a fault in the grid-connected mode. The method proposed in [18] uses a fifth harmonic injection after fault occurrence to detect the fault in the islanded microgrid; harmonic injection-based fault detection methods are also presented in [86]–[91]; to implement harmonic injection-based methods, an auxiliary control loop should be embedded in the inverter's control system which is not always feasible.

In [92], a fault detection method by using a distance relay with residual voltage compensation is proposed, but the method only detects the fault on the interconnection line between the Point of Common Coupling (PCC) and the microgrid.

In [93], authors proposed a fault detection method based on the traveling waves; however, 1-MHz sampling frequency and specific voltage transformers are required for implementation.

In [94], based on the relationship between the first peak value of fault current wavelet energy spectrum, authors proposed a fault detection method for microgrids, but the method only detects faults in the grid-connected mode.

A protection scheme based on voltage measurement is presented in [95]. In this method, three-phase voltages are measured and transformed to a "dq" synchronous frame. Then, V_q is compared with the V_q reference, and the fault can be detected. The proposed scheme needs communication between relays to compare the value of deviation from the V_q reference and to decide which relay should trip.

An impedance differential protection is presented in [96]. The measured impedance at both ends of the line is compared, and the fault is detected. In addition, for low-impedance faults, an impedance-based inverse time characteristic is introduced. It should be mentioned that this scheme cannot be implemented with available protection devices; moreover, it uses a differential method that requires communication between relays.

1.2 Problem Definition

As renewable energy-based resources with high randomness, intermittence, and fluctuation are connected to the microgrid, with the fast increase in the use of power electronic devices, they have brought significant challenges to the field of protection. Although different methods are presented in the literature to improve the performance of the traditional protection schemes in microgrids, the lack of systematic research on the protection of microgrids integrating inverter-based DERs still exists.

The main challenges in the protection of microgrids with high penetration of inverter-based resources are:

a) Limited fault current: to protect the power electronic switches used in the inverter, the control system of the invert limits the current during fault to 1.2 to 2 times the inverter's nominal current; this is problematic as conventional protection schemes rely on the high current magnitude to detect the fault [2]–[4].
b) Adopting different control schemes: inverters adopt different control schemes which make their fault current analysis and estimation more complex as compared to the conventional SG [2]–[4].

c) Absence of negative sequence current: a generic voltage source converter control system usually suppresses negative sequence current as explained in section 1.1.3; this is problematic, especially in the determination of the fault current direction which is crucial for a selective protection scheme [2]–[4].
d) Absence of the fault ride-through ability: the majority of inverters used in the distribution system become disconnected from the microgrid in the first 4.5 to 10 AC cycles after a fault [2]–[4], [97].

As discussed earlier, fault detection and protection are crucial parts of any electrical system since they protect personal safety and power equipment. Therefore, this thesis is aimed to do systematic research on the fault current characteristics of inverters with different control designs, study the possible fault scenarios in microgrids, investigate the voltage and current environment in microgrids, and explore the distinct fault behavior experienced by the two microgrid operating modes (grid-connected and island), which results in state-of-the-art protection for microgrids integrating inverter-based DERs.

1.2.1. Thesis Statement

The thesis recognizes the protection challenges in microgrids integrating inverter-based recourses and the limitations of the conventional protection elements; it then:

a) investigates several system parameters and shows that among the system parameters, voltage phase angle shift can be used for fault detection in microgrids. The thesis also proposes a new parameter obtained from the current signal. It then introduces a fault detection element for microgrids by employing the proposed parameters.
b) demonstrates the problems with conventional directional elements in microgrids and proposes a new directional element that determines the fault current direction in microgrids integrating inverter-based distributed energy resources based on a new parameter named current phase angle shift (*CPS*).
c) introduces a protection relay based on the proposed fault detection element and directional element and designs a protection scheme implemented by the proposed relay for microgrids

that can detect the fault, determine the fault zone, and remove the fault from the system so that the system can continue its normal operation.

d) implements the proposed protection relay and its elements in a Controller Hardware In the Loop (C-HIL) setup and demonstrates the performance of the proposed protection scheme by using real-time simulation.

1.2.2. Research Objectives

The research objectives of this thesis are explained in the following:

- **Fault detection element:** This includes conducting research on the current and voltage environment in microgrids, investigating the fault current and voltage characteristics of the microgrid, proposing parameters, and designing techniques to detect different types of faults in a microgrid integrating inverter-based DERs.

- **Directional element:** This includes studying the challenges that the conventional directional elements face in the presence of the inverter-based DERs in a microgrid and proposing a solution to determine the direction of the current under the fault conditions in a microgrid.

- **Protection scheme for microgrid**: This includes research on the possible scenarios in microgrids, which results in defining the features that must be considered in a microgrid protection scheme.

1.2.3. Methodology

This thesis proposes a protection scheme for microgrids integrating inverter-based DERs to address the protection challenges discussed in the previous sections. The protection scheme is defined as a scheme that protects personal safety and power equipment in case of a short circuit fault in the system. Such a scheme can detect faults, determine the fault zone, and remove the fault from the system so that the system can continue its normal operation. To achieve this, the challenges with the conventional protection schemes are recognized, and the fault current and voltage characteristics of the microgrid integrating inverter-based DERs are investigated under different operating modes and inverter control strategies. This investigation is carried out using model-based simulation and experimental tests for different microgrid configurations. New parameters and methods are proposed to detect the fault and determine the fault current direction. These methods have been tested in different microgrid configurations by using MATLAB Simulink software. Next, a protection relay for microgrids is proposed based on the introduced fault detection and directional elements. Then, a protection scheme is proposed and implemented by using the proposed protection relay. The proposed protection scheme is also tested in different microgrid configurations by using MATLAB Simulink software. The proposed relay is implemented in the Controller Hardware In the Loop setup by employing an actual physical relay, and it is validated in real-time in different microgrid configurations. Finally, the proposed method is applied to the measurements obtained from an actual distribution test bench and its performance is validated. Figure 1-3 demonstrates the procedure of performing the protection studies in the thesis. Also, the employed research, software, and hardware tools can be found in section A.6 of the appendix.

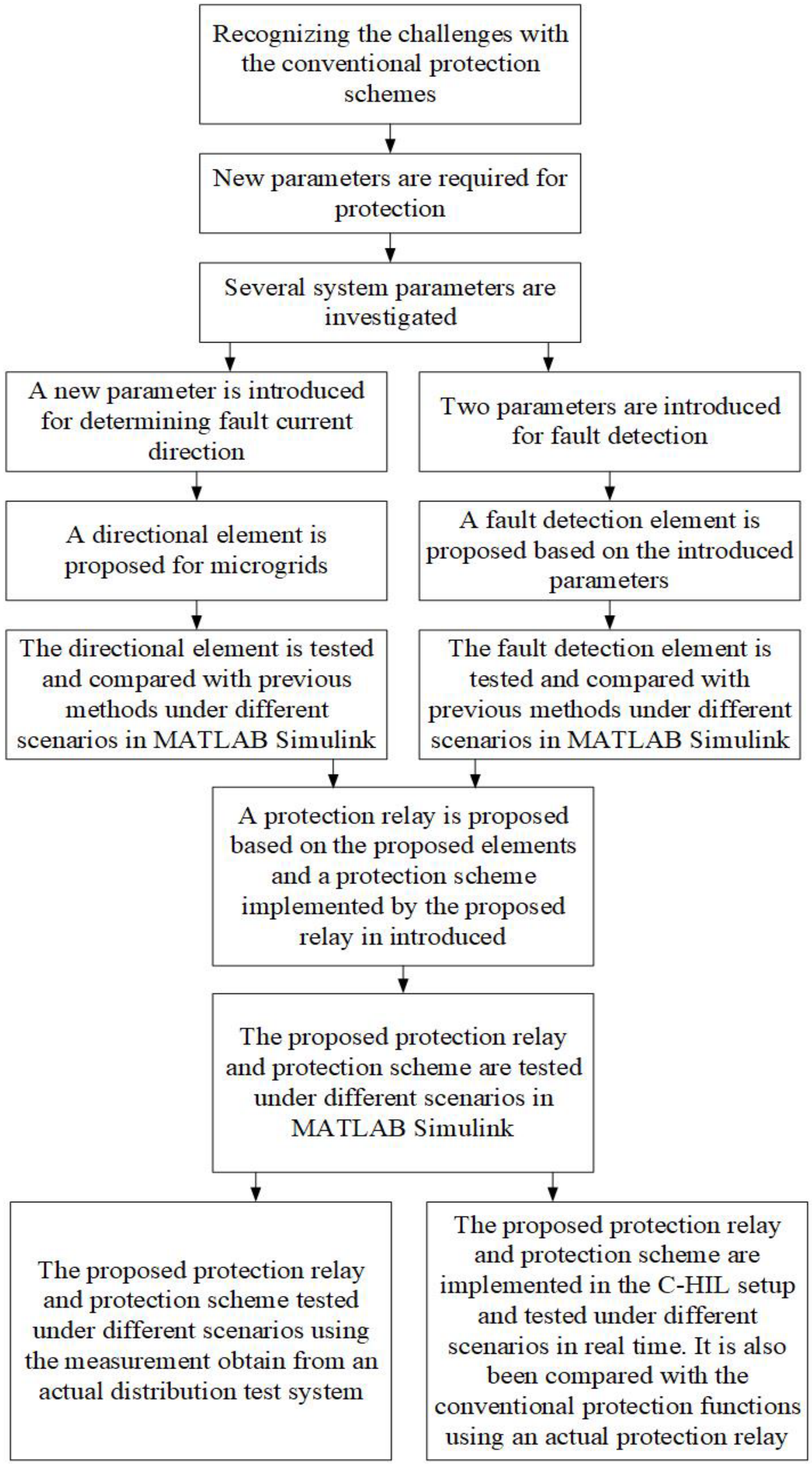

Figure 1-3: Methodology

1.2.4. Modeling of the inverter-based resources and the choice of the benchmark microgrids

As there are currently no standard model available for fault analysis of inverters, several models have been used in the process of testing the performance of the proposed methods including models based of fixed frequency approach [98], droop control [99], constant active/reactive power [12], average switching/ PWM switching, and single and multiloop control strategies [19]. In addition, the performance of the proposed methods has been tested using real time models and the measurements taken from experimental tests.

In addition, the proposed methods have been tested in most common microgrid benchmark systems including CIGRE benchmark system [80], [100]–[104], the double feeder microgrid benchmark system [75], [105]–[110], and low-voltage distribution feeder [111]–[113].

More information on the inverter models and the microgrid benchmark systems can be found in the appendix section.

1.2.5. Experimental Validation

The performance of the proposed protection scheme and the proposed relay functions are validated in C-HIL simulations. A real-time simulator is employed to model the microgrids in real-time. The microprocessor-based protection relay, serial radio transceiver, and a real-time embedded industrial controller are programmed to implement the proposed method. An Analog I/O card is used to connect the relay, industrial controller, and real-time simulator. The C-HIL validation is performed for three different microgrid configurations for different fault scenarios. The results obtained from the C-HIL setup validate the MATLAB Simulink results.

In addition to C-HIL validation, the method is applied to the measurements obtained from performing a fault on an actual distribution system. The results are discussed in detail in chapter 5.

1.3 Claims of Originality

The contribution of this dissertation provides the original solutions for protecting microgrids that include inverter-based distributed generations. As shown in the referenced peer-reviewed papers, the main contributions of the thesis are highlighted below:

- Two parameters named voltage Phase Angle Shift (*PAS*) and *D* parameters are introduced, and a fault detection method is presented. The method detects the fault by measuring the *PAS* and *D* parameters and employing a new relay characteristic. The *PAS* parameter is a shift in the voltage phase angle following a fault which is mainly caused by three factors: (a) the active power and reactive power variation following a fault and their effects on frequency and voltage levels (b) the variation in the *X/R* ratio between the source and the faulted feeder, and (c) the transformation of the sag to lower voltage levels as a result of a fault. The *D* parameter is defined as the difference between the predicted and the actual current samples.

- A method to determine the fault current direction in microgrids integrating inverter-based distributed energy resources is introduced, after demonstrating the problems with conventional directional elements in microgrids. The method determines the fault current direction based on a new parameter named current phase angle shift (*CPS*) and the direction of the current before the fault.

1.4 Dissertation Outline

After introducing the research topic and reviewing the protection challenges in microgrids in chapter 1, the rest of the thesis is organized into the following chapters.

- Chapter 2: Fault Detection Element

Two parameters for fault detection in microgrids are introduced in chapter 2, and a fault detection element based on the proposed parameters is introduced. Then, the fault detection element is tested under different fault scenarios in a benchmark microgrid system that includes battery energy storage and wind turbines, in both island and grid-connected modes.

- Chapter 3: Directional Element

In chapter 3, first, the challenges faced by the conventional directional elements such as negative sequence, positive sequence, and phase directional elements in the presence of inverter-based DERs in microgrids have been discussed. Next, a new directional element is proposed that determines the current direction during fault based on the current phase angle shift. Then, the performance of the proposed directional element is evaluated under different scenarios in a benchmark microgrid system. Finally, its performance is compared with the conventional directional elements.

- Chapter 4: Architecture of the Proposed Protection Scheme

By employing the fault detection element presented in chapter 2 and the directional element presented in chapter 3, a protection relay for microgrids is presented in chapter 4; also, a protection scheme implemented by the proposed relay is introduced. Then, the performance of the proposed relay and the protection scheme is evaluated under different scenarios by providing simulation results.

- Chapter 5: Real-time Controller-Hardware-in-the-Loop Validation and Experimental Results

In chapter 5, the performance of the proposed protection relay and the protection scheme is validated by providing Controller-Hardware-in-the-Loop (C-HIL) and experimental results. The C-HIL results are obtained for three microgrid systems under different scenarios.

Chapter 2 : Fault Detection Element

2.1 Introduction

As discussed in chapter 1, inverters adopt different control schemes which make their fault current analysis and estimation more complex. The fault current magnitude varies significantly when the microgrid transfers from the grid-connected to the island mode of operation. The fault current coming from the main grid is comparatively large in the grid-connected mode (about 16 times the nominal current). In contrast, in the island mode of operation, the fault current is relatively small (about 2 times the nominal current). Besides, the fault current contribution of IBRs is different from the traditional synchronous generators; this is because of the current control loop embedded in the inverter control system, which limits the maximum output current to 1.2 to 2 pu [114], [115]. Moreover, the test results presented in [97] show that the majority of inverters used in the distribution system become disconnected from the microgrid in the first 4.5 to 10 AC cycles after a fault. In other words, the majority of inverters tested in [97] stay connected to the system and ride-through over a short pried of time (4.5 to 10 AC cycles). LVRT requirements have an ongoing status in the grid codes. For example, IEEE 1547-2018 [116] allows DERs to ride-through over a wide range of voltage disturbances for at least 0.16 seconds. Currently, some of the LVRT requirements are applied to the medium voltage connected DERs in the new German grid code requiring DERs to stay connected to the system during fault for 0.15 seconds [117]. Therefore, fault clearance within the 4.5 AC cycles after fault occurrence is considered the design criteria in this thesis. Fault clearing time includes the time needed for fault detection, determination of the current direction, communication and coordination. In other words, the total time needed to clear the fault is defined as fault clearing time. To achieve this, voltage Phase Angle Shift (*PAS*) and *D* parameters are introduced, and a fault detection element is presented in this chapter that can detect the fault within the first AC cycle after the fault. The method detects the fault by measuring the *PAS* and *D* parameters and employing a new relay characteristic based on Mahalanobis Distance (MD) [118]. In this chapter, first, the procedure that leads to the selection of the parameters for fault detection is explained. Next, the proposed parameters, the calculation procedure, and the relay

Table 2-1: Some of the investigated parameters for fault detection in microgrids

dI/dt	dV/dt	dI_x/dt
Power Factor (PF)	Current Phase Shift	Rate of change of X
voltage phase shift	Z	dZ/dt
Y	dY/dt	Susceptance (B)

characteristic are discussed. Finally, the simulation results are provided.

2.2 Parameter Selection

In order to design the fault detection element, several system parameters have been investigated. Some of the investigated parameters are shown in Table 2-1. The investigation has been done by performing different load, transformer, and DG switching along with different fault scenarios. Then, the parameter is measured for each scenario to determine if the fault can be distinguished from the switching scenarios based on the obtained value for the parameter. After performing this procedure on different grid configurations, the voltage phase angle shift is selected for fault detection. As an example, Figure 2-2 demonstrates and compares the voltage phase angle shift obtained for load and transformer switching, DG switching, bolted and impedance ($R_f = 40$ ohms) Phase to Ground (PG), Phase to Phase (PP), Phase to Phase to Ground (PPG), and three Phase (3P) faults for the low-voltage distribution feeder and double feeder microgrid, in the island and grids connected modes of operation. It should be mentioned that 40 ohms fault impedance is chosen as the design criteria as discussed in Section 1.1.3. The description and parameters of the low-voltage distribution feeder and the double feeder microgrid shown in Figure 2-2 (a) and (d) can be found in sections A.1 and A.2 and Table A-1 and Table A-2 of the Appendix section, respectively. As shown in Figure 2-2, the voltage phase angle shift following a fault is larger as compared to the switching events. It should be mentioned that the specific procedure that is developed to measure this parameter and the main causes of voltage phase angle shift will be discussed in the next sections.

To understand the origin of phase angle shift associated with voltage sags, consider the single-phase voltage divider shown in Figure 2-1 for a three-phase fault, as that enables us to use the single-phase model. In Figure 2-1, Z_s is the source impedance and Z_l is the impedance of the line from the busbar to the fault location. All load currents are neglected, and it assumed that $E = 1$. Therefore, the complex voltage at PCC will be:

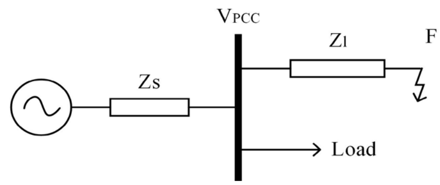

Figure 2-1: voltage divider

$$V_{PCC} = \frac{Z_l}{Z_S + Z_l} \tag{2-1}$$

where:

$$Z_l = R_l + jX_l \tag{2-2}$$

$$Z_S = R_S + jX_S \tag{2-3}$$

Therefore,

$$\varphi = \arctan(\frac{X_l}{R_l}) - \arctan(\frac{X_S + X_l}{R_S + R_l}) \tag{2-4}$$

φ in the above example shows the phase shift in voltage as a result of the change in the grid equivalent impedance (X/R ratio) following a fault. As explained above, the variation of the voltage phase angle shift is not related to the behavior of the source as a result of the fault. That is why voltage angle shift is selected here for fault detection in microgrids integrating inverter-based resource.

The D parameter which is defined as the difference between the actual and predicted current samples (predicted by linear prediction) is also introduced in addition to the voltage phase angle shift. The procedure for calculating the D parameter is explained in section 2.3.2. Figure 2-3 demonstrates and compares the D parameter obtained for load and transformer switching, DG switching, bolted and impedance ($R_f = 40$ ohms) Phase to Ground (PG), Phase to Phase (PP), Phase to Phase to Ground (PPG), and three Phase (3P) faults for the mentioned microgrid configurations in the island and grid-connected modes. As Figure 2-3 shows, because of the presence of the inverter-based resources in the system and their limited fault current, the *D* parameter obtained for fault and switching conditions are very close for some relays. For example,

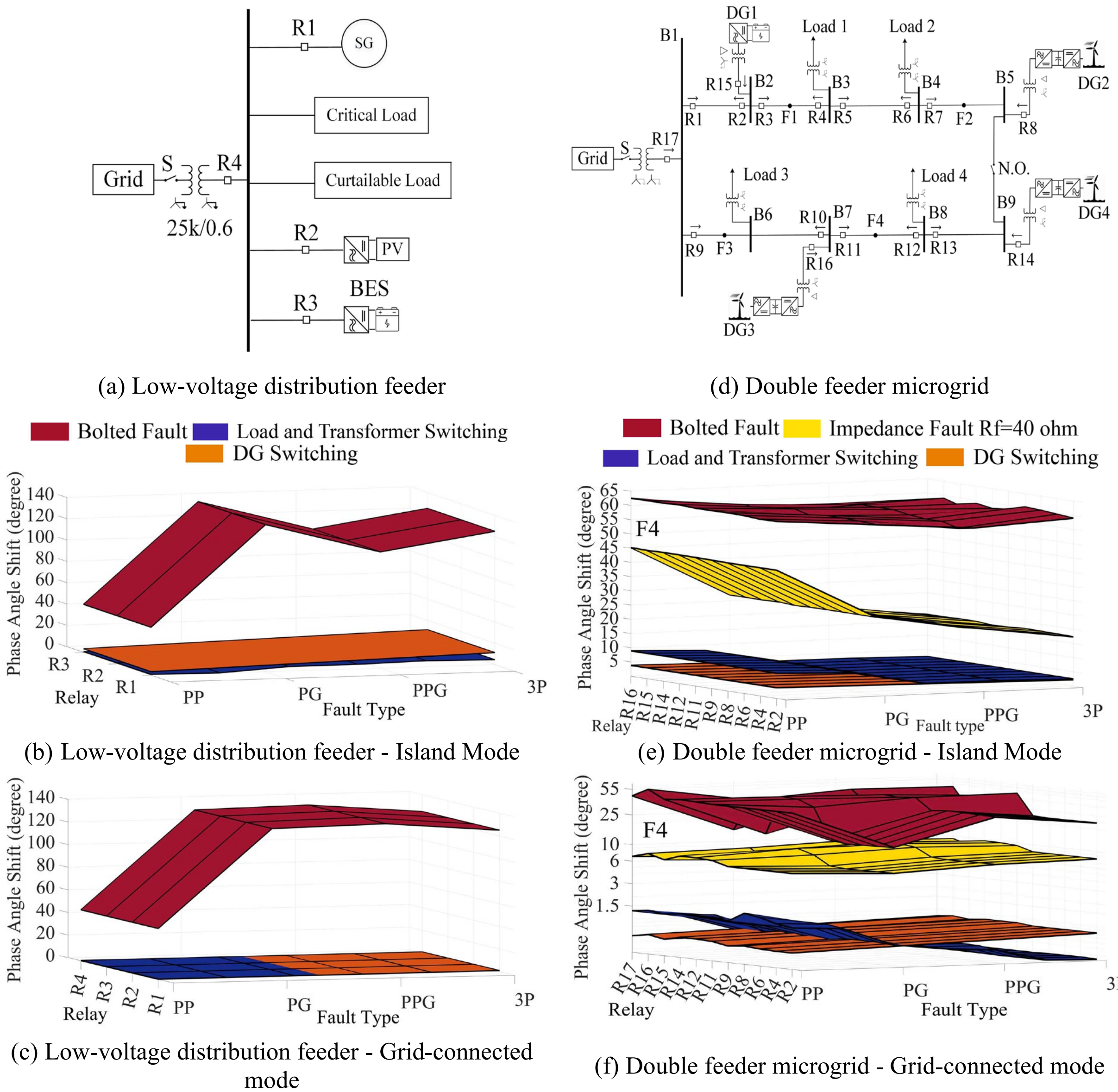

Figure 2-2: Voltage phase angle shift measured under different scenarios for two network configurations

the *D* parameter measured by R14 in the double feeder microgrid is 1882 for an impedance fault (Rf = 40 ohms) at point F4, and it is 1686 for the DG switching event. Therefore, the *D* parameter cannot be used separately to detect the fault in those cases. But there are there main advantages in using the *D* parameter along with the voltage phase angle shift parameter to detect the fault. First, the *D* parameter allows defining a dynamic boundary for the voltage phase angle shift parameter to detect the fault, which results in fast fault detection for different types of faults as compared to when only the voltage phase angle shift is employed. Second, the *D* parameter can improve the performance of the proposed method in the presence of regular resources in the system like synchronous generators. It is because synchronous generators are able to provide up to 5 pu (5 times the normal current) current under fault conditions [26]. Third, as it will be explained in section 2.3.2, to calculate the D parameter, in each sampling window, the last 25% of the samples in the window are predicted using the previous 75% of the samples in the sampling window based on linear prediction; this feature enables this parameter to readjust itself based on the different operating conditions of the microgrid without the need to change its base value under different loading condition. That is why the D parameter is a suitable candidate for fault detection in microgrids.

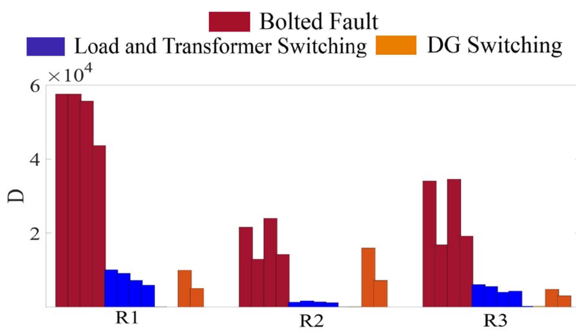

(a) Low-voltage distribution feeder
Island Mode

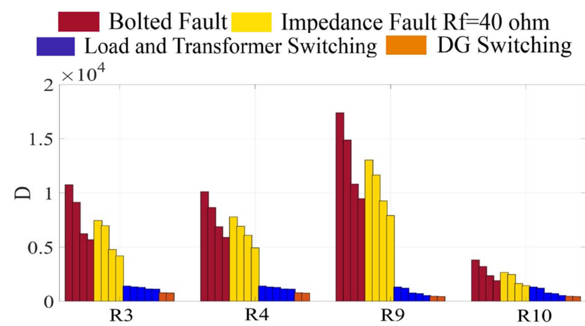

(c) Double feeder microgrid - Island Mode

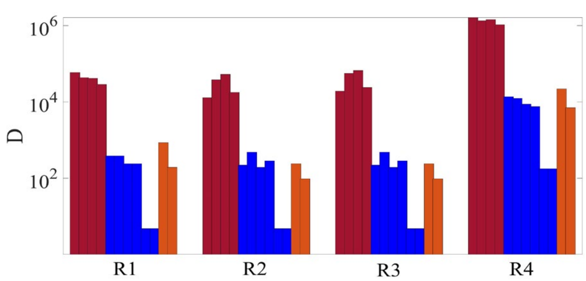

(b) Low-voltage distribution feeder
Grid-connected mode

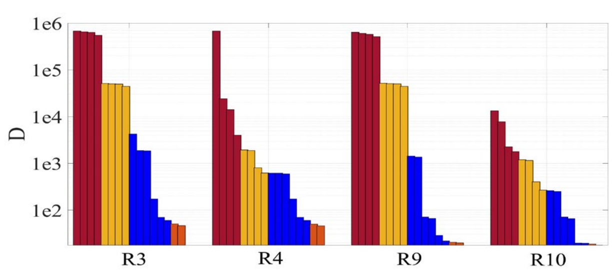

(d) Double feeder microgrid - Grid-connected mode

Figure 2-3: *D* parameter measured under different scenarios for two network configurations

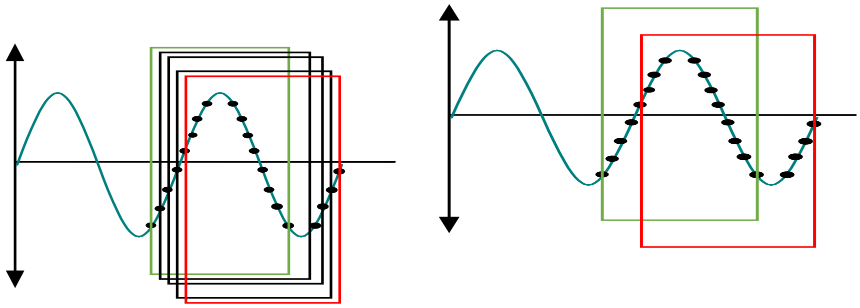

Figure 2-4: a) Moving sampling window b) Present and past sampling windows © 2021 IEEE [1]

2.3 Proposed Parameters

In this section, the voltage Phase Angle Shift (*PAS*) and *D* parameters are introduced and employed to detect the feeder faults in microgrids. These parameters are explained in the following subsections.

2.3.1 Voltage Phase Angle Shift

A short circuit in the system not only causes a voltage magnitude drop but a change in the voltage phase angle as well. The main causes of the voltage phase angle shift are the difference in the *X/R* ratio between the source and the faulted feeder, the active and reactive power variation and their effects on frequency and voltage level, and the transformation of the sag to lower voltage levels [119]–[121].

This phase angle shift is referred to as a phase angle shift associated with the voltage sag that demonstrates itself as a shift in the zero-crossing point of the instantaneous voltage [119]–[121]. Consider the voltage waveform and the sampling windows shown in Figure 2-4. In this figure, the sampling frequency is 16 samples per cycle. The red window shows the present sampling window, and the green window depicts the past sampling window, which is placed 4 sampling windows behind the present sampling window. Both present and past sampling windows are shown in Figure 2-4(b). In normal conditions, the phase difference between the sampling windows shown in Figure 2-4(b) is ((360)/16)*4= 90 degrees. In other words, if the past sampling window is shifted forward by 90 degrees, the two waveforms are exactly in phase. But when a fault occurs, the phase difference between the present and past sampling windows changes. If in the given example, the phase difference is either more or less than 90 degrees, this can be an indication of a fault [1].

2.3.1.1 Voltage phase angle shift calculation

In order to measure the phase angle shift, the fundamental component of the present and past sampling windows are obtained using the Least Square (LS) approach. Consider the sampled voltage based on the Fourier series as shown in

$$V(kT_s) = \sum_{n=1}^{N} A_n \sin(n\,\omega_0 kT_s) + B_n \cos(n\,\omega_0 kT_s) \tag{2-5}$$

where N is the maximum harmonic order of the voltage; ω_0 is the fundamental angular frequency; T_s is the sampling period, and $V(kT_s)$ is the k^{th} component of the voltage vector V:

$$V^T = [V(t_0 + T_s) \;\; V(t_0 + 2T_s) \;\; V(t_0 + 3T_s) \ldots V(t_0 + KT_s)] \tag{2-6}$$

Vector V contains all measured voltage samples within one cycle, and K is the total number of samples in one cycle. Therefore, the vector form of (2-5) can be written as

$$V = S\,Y \tag{2-7}$$

where Y is the unknown coefficient matrix, and S is known signals. Since only the fundamental frequency needs to be estimated here, $Y^T = [A_1, B_1]$ and S can be considered as the following:

$$S^T = \begin{bmatrix} \sin(\omega_0 T_s) & \sin(\omega_0 2T_s) & \ldots & \sin(\omega_0 KT_s) \\ \cos(\omega_0 T_s) & \cos(\omega_0 2T_s) & \ldots & \cos(\omega_0 K T_s) \end{bmatrix} \tag{2-8}$$

using the LS approach, the fundamental frequency component of the voltage is estimated as

$$Y = (S^T S)^{-1} S^T V \tag{2-9}$$

$$\hat{V} = S(S^T S)^{-1} S^T V \tag{2-10}$$

where $\hat{V}$ is the estimated fundamental component of the measured voltage. LS approach is employed here to estimate the fundamental frequency component of the signal fast; it should be mentioned that $S(S^T S)^{-1} S^T$ is a constant matrix and can be computed offline and stored. When the fundamental components of the present and past sampling windows are calculated, the phase difference between the present and past sampling windows can be obtained by computing the scalar product of $\hat{V}_{pr}$ and $\hat{V}_{pa}$ that are the estimated fundamental component vector of the present sampling window and the estimated fundamental component vector of the past sampling window, respectively

$$\hat{V}_{pr} . \hat{V}_{pa} = \left|\hat{V}_{pr}\right| \left|\hat{V}_{pa}\right| \cos(\varphi) \tag{2-11}$$

$$\varphi = a\cos\left(\frac{\hat{V}_{pr} . \hat{V}_{pa}}{\left|\hat{V}_{pr}\right| \left|\hat{V}_{pa}\right|}\right) \tag{2-12}$$

where φ is the phase difference between the two vectors in radian; $|\hat{V}_{pr}|$ and $|\hat{V}_{pa}|$ are Euclidian lengths of $\hat{V}_{pr}$ and $\hat{V}_{pa}$ respectively.

Therefore, the net Phase Angle Shift (*PAS*) between the fundamental component of the present and past sampling windows is:

$$PAS = \left|\frac{\varphi \times 180}{\pi} - \frac{\alpha \times 360}{K}\right| \tag{2-13}$$

where *K* is the number of samples in one cycle, and α is the number of samples between the present and past sampling windows. For example, in the given example in Figure 2-4(b) $\alpha = 4$ and $K = 16$; therefore, in normal conditions *PAS* is 0, and if the *PAS* is greater than zero it can be an indication of the fault. α should be tuned by considering the sampling frequency and can be chosen between $0.1K$ to $1K$[1].

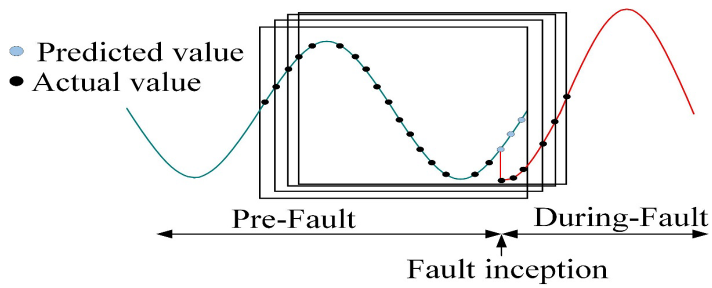

Figure 2-5: Moving sampling window; predicted and actual samples © 2021 IEEE [1]

2.3.2 D parameter: Difference between Predicted and Actual Current Samples

D is defined here as the difference between the predicted and the actual current samples. In each sampling window, the last 25% of the samples in the window are predicted using the previous 75% of the samples in the sampling window based on linear prediction. This ratio is tuned to provide suitable accuracy for this application. As an example, assume that the sampling frequency is 16 samples per cycle as shown in Figure 2-5. The linear prediction is employed here to predict future values of the current signal. It is because linear prediction is a simple and effective method that can be programed in the protection relays

$$I(m) \approx a_1 I(m-1) + a_2 I(m-2) + a_3 I(m-3) + \ldots \tag{2-14}$$

where, $I(m)$ is the predicted mth value of I, and $I(m-1),\ I(m-2)\ and$ ... are the past values of I. Since the past I values are known, a_i coefficients can be found by using the LS approach.

For example, if we seek a third-order linear predictor, coefficient matrix $a = [a_1, a_2, a_3]^T$ is one of the solving of an overdetermined system of equations. If $I(m)$ is known for $1 \leq m \leq M-1$, then the overdetermined system of equations is given by (2-15).

$$\begin{bmatrix} I(4) \\ I(5) \\ \vdots \\ I(M-1) \end{bmatrix} \approx \begin{bmatrix} I(3) & I(2) & I(1) \\ I(4) & I(3) & I(2) \\ \vdots & \vdots & \vdots \\ I(M-2) & I(M-3) & I(M-4) \end{bmatrix} \begin{bmatrix} a_1 \\ a_2 \\ a_3 \end{bmatrix} \tag{2-15}$$

Equation (2-15) can be written as $\bar{I} = Ha$ where H is a matrix of size $(M-4) \times 3$. Using the LS approach, the solution is given by $a = (H^T H)^{-1} H^T \bar{I}$; once the coefficients a_i are found, then $I(m)$ for $m \geq M$ can be estimated using (2-14).

As a result of a fault, the change in the current causes the predicted samples of the current waveform to deviate from their actual values as shown in Figure 2-5. Since the window includes both pre- and during-fault data, the difference between the actual samples and the predicted samples is significant. For the 16 samples per cycle, the last 4 samples are predicted. Therefore, parameter D, the difference between the predicted sample values and the actual sample values is [1]

$$D = \left| \begin{array}{l} (Sa_{13} + Sa_{14} + Sa_{15} + Sa_{16})_{Actual\ valuse} - \\ \qquad (Sa_{13} + Sa_{14} + Sa_{15} + Sa_{16})_{Predicted\ values} \end{array} \right| \tag{2-16}$$

where $Sa_{13}, Sa_{14}, Sa_{15}, and\ Sa_{16}$ are the last four samples of the signal in the sampling window.

2.4 Fault Detection Scheme

In this section, the proposed protection scheme is explained stepwise. First, in each sampling window, the voltage *PAS* and the *D* value of the current for three phases are obtained. Second, the maximum values of *PAS* and *D* among the three phases are calculated; the maximum values of *D* and *PAS* are named as D_{Max} and PAS_{Max}, respectively; the calculation of the maximum value among the three phases is to account for cases of unbalanced systems and asymmetrical faults. If the operating point (x(D_{Max}, PAS_{Max})) of the relay is outside of the relay's normal operating area, the trip signal will be issued.

Since (*D, PAS*) measured under fault conditions behaves differently from the (*D, PAS*) measured for switching events at least in one dimension (D dimension or PAS dimension), it is possible to differentiate between a fault and switching events by using both *D* and *PAS* parameters and employing Mahalanobis Distance (MD) metric [118]. MD is an effective tool to find outliers in multivariate data. The MD is unitless and scale-invariant. It also takes into account the correlations of the data. Another characteristic of MD is that it has an approximate chi-square distribution for normal multivariate observations. These features of MD allow us to define a general procedure for determining the relay characteristic; a procedure that is the same for different system configurations. Other applications of MD in the power system can be found in [122]–[124]. The Chi-Squared distribution is commonly used in applied statistics to provide the basis for making inferences about the variance of an arbitrary population based on a sample set of data [125]. Therefore, by determining the confidence ellipse of the relay characteristic based upon the 99.9% quantile of the Chi-Square distribution with 2 degrees of freedom, it is possible to differentiate between the normal events and fault conditions which will be shown through the several case studies in the thesis. In fact, the (*D, PAS*) measured for switching events and the (*D, PAS*) obtained for fault conditions belong to two different clusters as shown through the case studies in this chapter, and the confidence ellipse determines the boundaries of the switching events cluster. To explain the procedure of drawing the relay characteristic, consider matrix E that is formed based on the D and PAS measurement for normal events in the system such as load switching, transformer switching, and DG switching

$$E = \begin{bmatrix} D_1 & D_2 & \dots & D_q \\ PAS_1 & PAS_2 & \dots & PAS_q \end{bmatrix} \tag{2-17}$$

where q is the total number of normal events, and each column contains the PAS and D measured for each event. MD of point $X = [D\ PAS]^T$ is defined by (2-18):

$$MD^2(x \mid \mu, C) = (x-\mu)^T C^{-1} (x-\mu) \in R^1 \tag{2-18}$$

where μ is the sample mean vector defined by (2-19)

$$\mu = \left[\frac{1}{q}\sum_{i=1}^{q} D_i \quad \frac{1}{q}\sum_{i=1}^{q} PAS_i \right]^T \in R^{2\times 1} \tag{2-19}$$

and C is the sample covariance matrix that is calculated by

$$C = \frac{1}{q-1}\sum_{i=1}^{q}\left(\begin{bmatrix} D_i \\ PAS_i \end{bmatrix} - \mu\right)\left(\begin{bmatrix} D_i \\ PAS_i \end{bmatrix} - \mu\right)^T \in R^{2\times 2} \tag{2-20}$$

As mentioned, the confidence ellipse of the relay characteristic is defined based upon the 99.9% quantile of the Chi-Square distribution with 2 degrees of freedom. 99.9% quantile is chosen because it will result in an ellipse that will ensure the relay does not operate following a normal event in the system and can detect impedance faults up to 40 ohms in medium voltage (25kV) systems as shown through investigated scenarios in the thesis. The eigenvectors of the sample covariance matrix define the principal axes of the confidence ellipse, and the *D* and *PAS* mean values define the center of the ellipse. Also, the lengths of the semi major and minor axes of the ellipse, l_j, can be determined from the eigenvalues, λ_j, of the sample covariance matrix as (2-21) shows.

$$l_j = \sqrt{\lambda_j \ \chi^2_{2,99.9}} = \sqrt{13.816 \ \lambda_j} \tag{2-21}$$

Therefore, to determine the relay confidence ellipse, the following steps should be taken. First: switching scenarios are simulated, and corresponding *PAS* and *D* values for each relay are obtained. Second: matrix E is formed for each relay and the mean and covariance matrix is formed. Third: The confidence ellipse for each relay is determined by calculating the eigenvalues of the sample covariance matrix shown in (2-20). After the confidence ellipse is obtained, it can be stored in the relay. Figure 2-6 shows the relay's characteristic, inside the confidence ellipse is the normal operating area whereas the outside is the trip area [1].

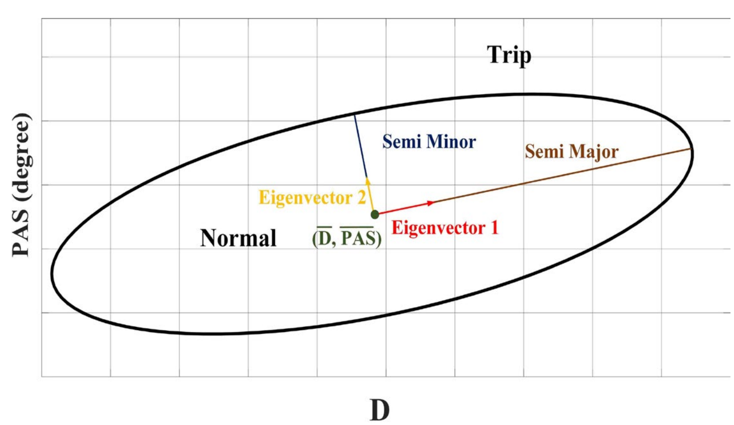

Figure 2-6:Relay's characteristic; normal and trip area

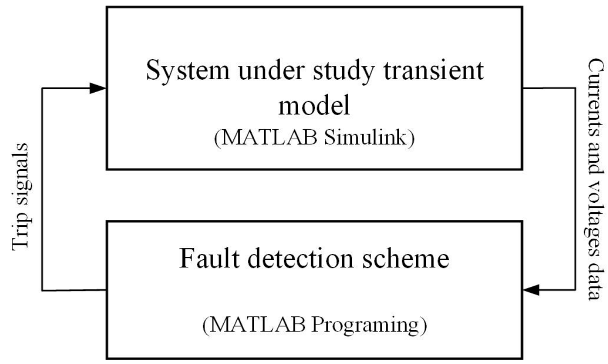

Figure 2-7: Model implementation – Fault detection scheme

2.5 Simulation Results and Discussion

In this section, the performance of the proposed fault detection scheme is evaluated through the simulation of different scenarios in the system under study by using MATLAB software. The system under study is modeled in MATLAB Simulink, and the fault detection method is programmed using MATLAB programing language as shown in Figure 2-7. The time step used for performing the simulation is 25 microseconds. The system under study is the modified CIGRE benchmark system [100], which includes a Battery Energy Storage (BES) and three type 4 wind turbines as shown in Figure 2-8. A type 4 wind turbine is a variable-speed wind turbine with a synchronous generator that is connected to the grid through a full-scale power converter. More information on type 4 wind turbine can be found in [126]. The system parameters are shown in Table A-3. The inverters control systems in the system under study are the conventional *dq* (direct-quadrature) control strategy for voltage source converters [98], [99]. The sampling frequency for the simulation results is 333 samples per cycle (19.98kHz). The system is solidly grounded; the grid and load transformers configuration are Yg/Yg, and the DG transformers configuration are Δ/Yg. Figure 2-8 also shows the relays installed at different points in the system. Each line is protected by two relays; line relays are directional. Also, a relay is allocated for the Point of Common Coupling (PCC) (R11) and each DG (R7 to R10). Each relay samples the local voltage and current. In the system under study, the Master-slave control strategy is employed. Information on the Master-slave control strategy can be found in [98]. In the system shown in Figure 2-8, DG 1 is the Master controller working in Voltage-Frequency (VF) mode, and DG2 to DG4 are the slaves working in PQ (active/reactive power) mode. In PQ control mode, inverters transfer a

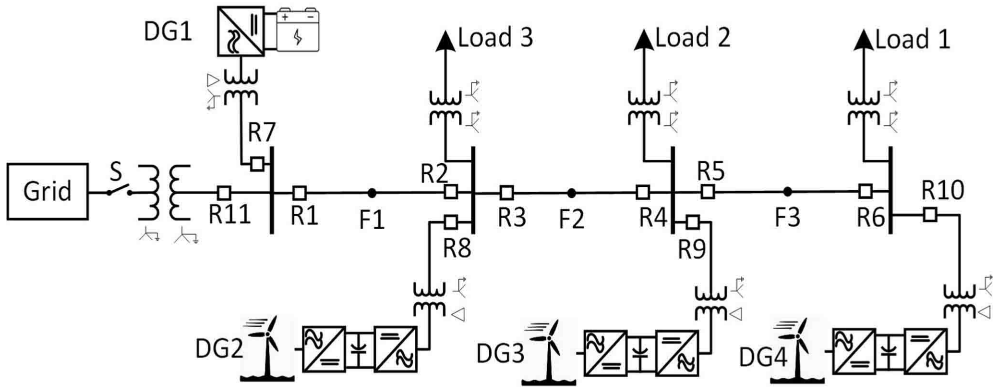

Figure 2-8: The modified CIGRE benchmark system © 2021 IEEE [1]

Table 2-2: Investigated scenarios for the island and grid-connected modes © 2021 IEEE [1]

	Island Mode				Grid-connected Mode		
	BF	IF ($R_f = 4$ ohms)	IF ($R_f =$ 40 ohms)	Switching	Switching	IF ($R_f =$ 30 ohms)	IF ($R_f =$ 20 ohms)
PG (F1, F2, F3)	×	×	×			×	×
PP (F1, F2, F3)	×	×	×			×	×
PPG (F1, F2, F3)	×	×	×			×	×
3P (F1, F2, F3)	×	×	×			×	×
Load 2				×	×		
Load 1=500kW				×			
Load 1=200kW+300kVar				×			
Load 1= 5MVA					×		
500kVA Transformer				×	×		
DG 3 Switching				×	×		

determined active (P^0) and reactive power (Q^0) to the microgrid, and they do not considerably contribute to controlling the voltage and frequency parameters of the microgrid. Therefore, inverters with PQ control mode can only operate in the island mode when an inverter with VF control mode or a synchronous generator is present in the microgrid [99], [127]. In VF control mode, inverters control the amplitude and frequency of the output voltage like synchronous generators [99], [127]. More information about the system under study and PQ and VF control modes implementation can be found in sections A.3, A4, and A.5 of the Appendix respectively. Table 2-2 demonstrates the investigated scenarios for the island and grid-connected modes. In case 1, the fault and switching scenarios for the island mode are inspected. The investigated scenarios for the island mode are shown in Table 2-2. In case 2, the fault and switching scenarios for the grid-connected mode are investigated. The scenarios for the grid-connected mode are shown in Table 2-2. The investigated fault scenarios include the Phase to Ground (PG), Phase to Phase (PP), Phase to Phase to Ground (PPG), Three Phase (3P) faults at points F1, F2, and F3 in the island and grid-connected modes; in the island mode, the fault scenarios are performed for Bolted Faults (BF), Impedance Faults with $R_f = 4$ ohms (IF), and impedance faults with $R_f = 40$ ohms; in the grid-connected mode, the fault scenarios are performed for IF with $R_f = 40$, 30 and 20 ohms. To show the ability of the proposed scheme in distinguishing the normal events from the fault conditions, several load, transformer, and DG switching scenarios are also investigated as shown in Table 2-2. The objective of examining the mentioned scenarios is to show that by using the two proposed parameters (*PAS* and *D*) and by employing the proposed fault detection scheme, all types of faults can be detected in the microgrid in both modes of operation; in case 3, the effect of the Short Circuit Capacity (SCC) of the grid feeder on the performance of the proposed protection scheme in the grid-connected mode is evaluated. The procedure of selecting switching scenarios to obtain relay characteristic is explained in case 4. In case 5, the effect of the inertia time constant on the performance of the proposed scheme is investigated. The impact of the presence of noise on the performance of the proposed scheme is evaluated in case 6. In case 7, the fault detection time of the proposed protection scheme is discussed; also, the proposed scheme is compared to the overcurrent and under-voltage fault detection methods in case 8. In case 9, the performance of the proposed method in a droop-controlled system is examined. The performance of the proposed scheme in the presence of a synchronous generator in the microgrid is evaluated in case 10, and finally, the sensitivity of the confidence ellipse to changes in the microgrid arrangement is investigated in case 11 [1].

2.5.1 Case 1: Island Mode – Fault and Switching Scenarios

In case 1, the fault and switching scenarios shown under the island mode column in Table 2-2 are investigated in the system under study shown in Figure 2-8 for the island mode. A detailed description of the system and the inverter control diagrams can be found in sections A.3, A.4, and A.5 of the Appendix section. Different faults are applied at points F1, F2, and F3; *PAS* and *D* parameters are measured by the relays shown in Figure 2-8. Table 2-3 shows *PAS* and *D* measured for the impedance faults with 40 ohms at point F1 along with *PAS* and *D* measured for the DG, transformer, and load switching events in the island mode. Table 2-3 demonstrates that the *PAS*

Table 2-3: Maximum voltage *PAS* and *D* parameter measured by relays for the scenarios shown in Table 2-2– Island mode

	Parameter	Load Switching events					mean	Impedance ($R_f = 40$) Fault at point F1 (PP, PG, PPG, 3P)				mean
R1	PAS	1.23	1.255	1.37	2.01	2.29	1.23	8.2	8.46	12.39	13.42	10.61
	D	604	566	1013	641	716	708	3066	2398	3073	2504	2760
R2	PAS	1.23	1.25	1.37	2.01	2.29	1.23	8.23	8.48	12.38	13.41	10.62
	D	609	567	1018	641	716	887	4307	2133	4785	2649	3468
R4	PAS	1.239	1.255	1.37	2.01	2.29	1.23	8.23	8.46	12.39	13.41	10.61
	D	924	825	1247	900	957	970	2953	1483	3271	1827	2383

parameter for load switching and fault scenarios belongs to two different clusters of the data. For example, *PAS* obtained for load switching events by R1 are 1.23, 2.25, 2.37, 2.01, and 2.29 degrees, and the *PAS* obtained for impedance faults with Rf=40 ohms by R1 are 8.2, 8.46, 12.39, and 13.42 degrees as Table 2-3 shows. The mean value for *PAS* following different switching scenarios is 2.03 degrees, and the mean value for *PAS* following different types of impedance faults is 10.61 degrees. Therefore, the mean value for PAS following fault scenarios is 5 times the mean value following switching events, which shows *PAS* for load switching and fault scenarios belongs to two different clusters. In Figure 2-9, *PAS* measured for the faults at points F1, F2, and F3 along with *PAS* measured for the DG, transformer, and load switching events in the island mode are shown and compared. The red surface in Figure 2-9 shows the *PAS* measured by different relays for bolted PG, PP, PPG, and 3P faults; the light blue surface in Figure 2-9 shows the *PAS* measured by different relays for PG, PP, PPG, and 3P faults with 4 ohms fault impedance ($R_f = 4$ ohms [128]); also, the yellow surface in Figure 2-9 shows the *PAS* measured by different relays for PG, PP, PPG, and 3P faults with 40 ohms fault impedance ($R_f = 40$ ohms); the orange surface in Figure 2-9 shows the *PAS* measured by different relays for the DG switching. Also, the PAS measured by different relays for transformer and load switching scenarios are shown by the dark blue surface. Figure 2-9 contains three 3D space coordinate planes; each coordinate plane belongs to one fault location. As demonstrated in Figure 2-9, the maximum *PAS* for the switching events is 2.3 degrees (transformer switching); *PAS* for the phase-to-phase fault with $R_f = 40$ ohms is 8.24 degrees. As shown in Figure 2-9, although the minimum *PAS* among the fault scenarios is for the phase-to-phase fault with $R_f = 40$ ohms, *PAS* for the phase-to-phase fault with $R_f = 40$ ohms is still about 3.5 times *PAS* for the switching events. In other words, the fault plates (red, yellow, and light blue) stand about 6 degrees higher than the plates for the switching event (dark blue and

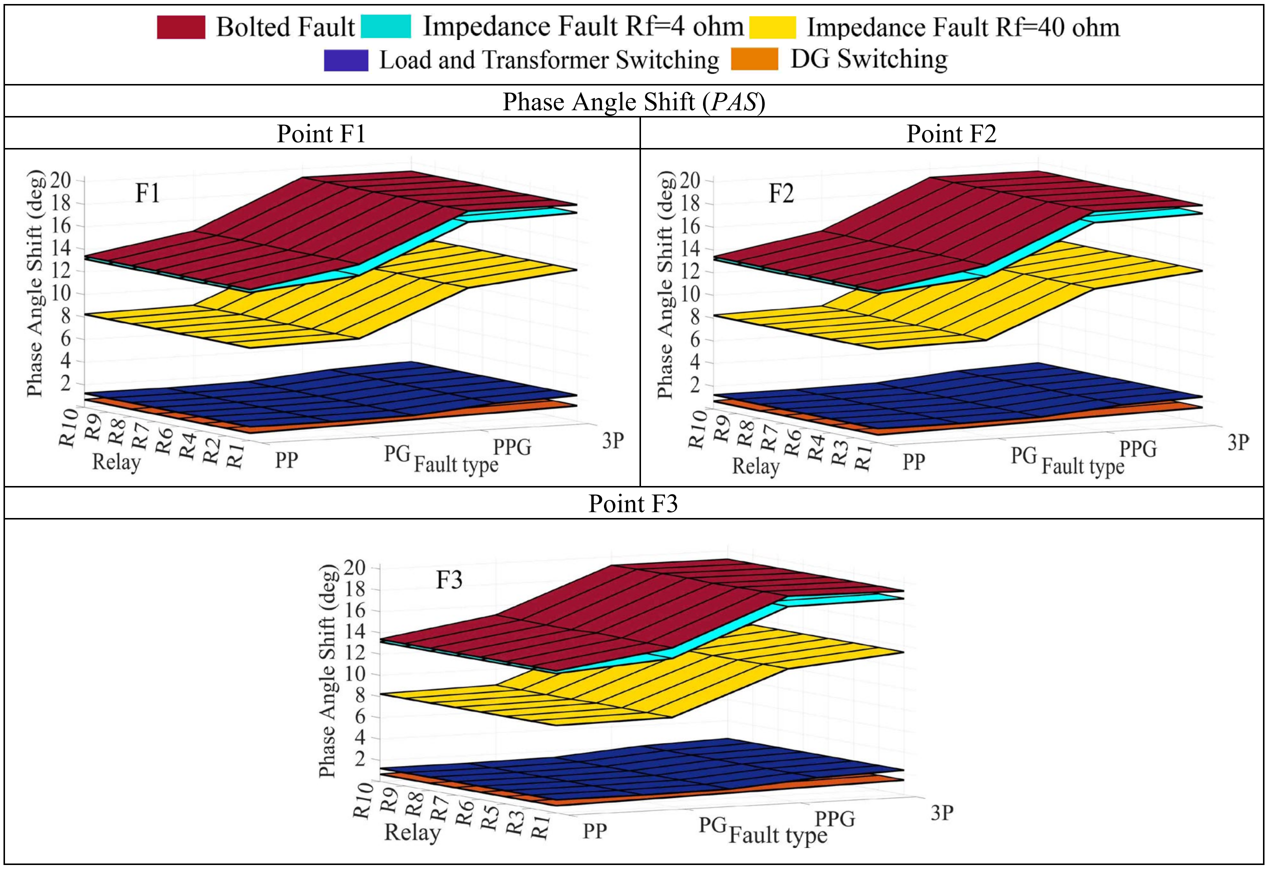

Figure 2-9: Maximum voltage *PAS* parameter measured by relays for the scenarios shown in Table 2-2 – Island mode © 2021 IEEE [1]

orange) which shows that the *PAS* as a result of switching events and fault conditions belong to two different clusters. This demonstrates that the voltage *PAS* can be employed for fault detection in the islanded microgrid by defining a threshold boundary based on the procedure explained in section 2.4.

The *D* parameter measured for the switching events is compared with the *D* parameter measured for different fault scenarios in Figure 2-10. As explained in section 2.3.2 the *D* parameter is obtained by analyzing the current waveform; for some relays in the system, the measured *D* value for the switching events and the fault scenarios are equal as shown in Figure 2-10. It is because inverters are not able to provide more than 1.2 to 2 pu current even in fault conditions. Therefore, current variation cannot be used separately in an inverter-based system to detect the fault, but it can be used as an indication of the fault conditions. In other words, the *D* parameter can be used

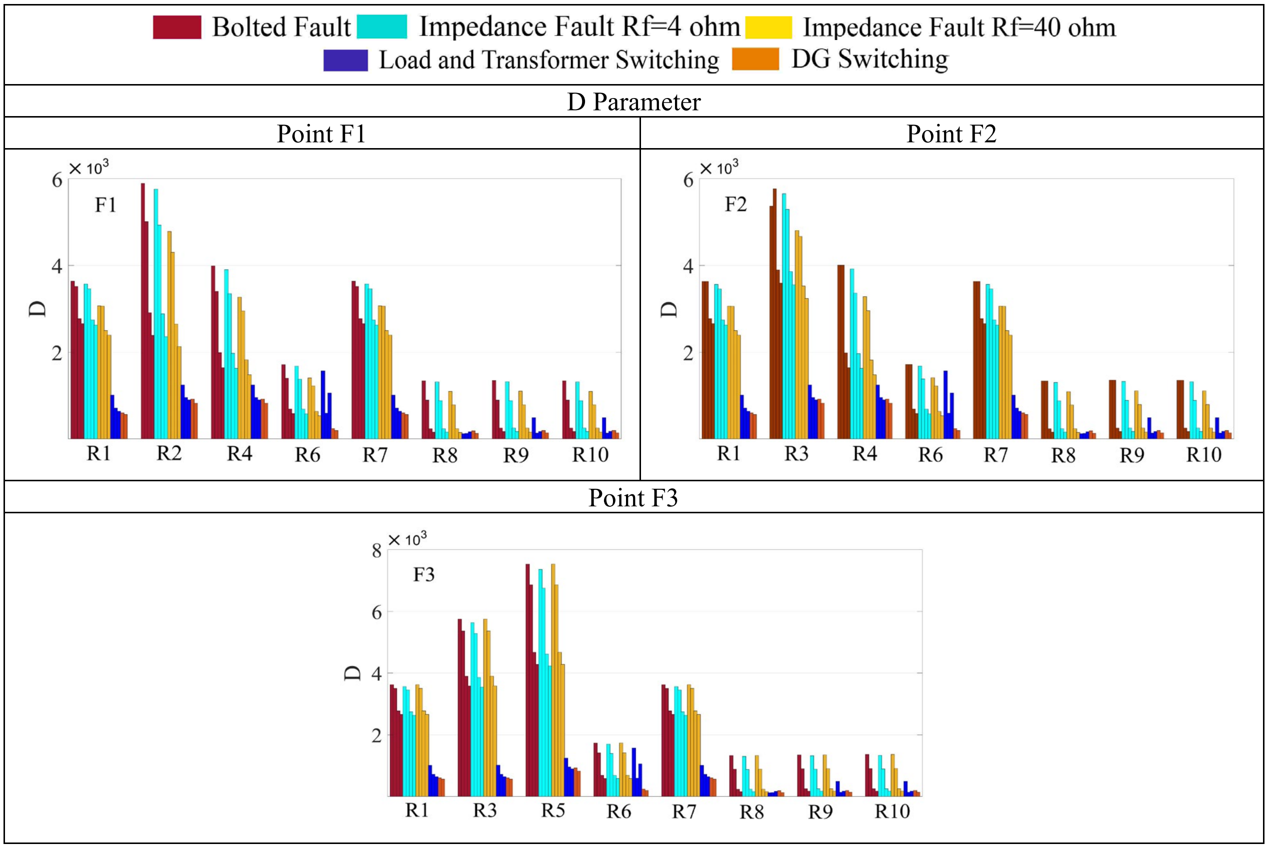

Figure 2-10: Maximum *D* parameter measured by relays for the scenarios shown in Table 2-2 – Island mode © 2021 IEEE [1]

Table 2-4: Relays' fault detection characteristics parameters – Island mode

Relay	Semi major axis	Semi minor axis	Eigenvector 1	Eigenvector 2	D mean	PAS mean
R1	947.70	1.77	(-0.99, 0.0007)	(-0.0007, -0.99)	447.83	1.14
R2	972.72	1.86	(-0.99, 0.0005)	(-0.0005, -0.99)	460.41	1.14
R3	1274.37	1.93	(-0.99, 4.85e-05)	(-4.85e-05, -0.99)	659.67	1.15
R4	1271.47	1.93	(-0.99, 4.47e-05)	(-4.47e-05, -0.99)	659.33	1.15
R5	2446.76	2.35	(-0.99, -0.0003)	(0.0003, -0.99)	515.88	1.10
R6	2045.20	1.82	(-0.99, -0.0003)	(0.0003, -0.99)	517.84	1.13
R7	971.66	1.86	(-0.99, 0.0005)	(-0.0005, -0.99)	460.54	1.14
R8	182.70	2.07	(-0.99, 0.004)	(-0.004, -0.99)	110.07	1.04
R9	454.06	2.22	(-0.99, 0.0008)	(-0.0008, -0.99)	156.17	1.16
R10	454.03	2.16	(-0.99, 0.0007)	(-0.0007, -0.99)	156.95	1.16

to define a dynamic boundary for the relay characteristic which results in a fast fault detection scheme based on the procedure explained in section 2.4. As Figure 2-9 and Figure 2-10 demonstrate, by using the two proposed parameters together and employing the fault detection scheme explained in section 2.4, it is possible to differentiate between switching events and fault conditions and detect the fault in the island mode of microgrid operation [1]. The relays' fault detection characteristics parameters obtained based on the fault detection scheme discussed in section 2.4 are shown in Table 2-4 for the island mode. It should be mentioned that the purpose of Figure 2-10 is to compare the D parameter measured for switching scenarios and fault for each relay separately as the relay uses locally measured currents and voltages to detect the fault.

2.5.2 Case 2: Grid-connected Mode- Fault and Switching Scenarios

In the grid-connected mode, the microgrid is connected to a 120kV main grid bus bar with 500 MVA short circuit capacity. The fault and switching scenarios shown under the grid-connected column in Table 2-2 are investigated for the grid-connected mode in case 2. As shown for the island mode of operation, the impedance faults have the lower voltage *PAS* among fault scenarios; therefore, only the impedance faults are simulated for the grid-connected mode. In case 2, the impedance faults with $R_f = 40, 30,$ and 20 ohms are applied at points F1, F2, and F3, and the *PAS* and *D* parameters are measured by the relays shown in Figure 2-8. Table 2-5 shows *PAS* and *D* measured for the impedance faults with 40 ohms at point F1 along with *PAS* and *D* measured for the DG, transformer, and load switching events in the grid-connected mode. Table 2-5 demonstrates that the *PAS* parameter for load switching and fault scenarios belongs to two different clusters of the data. For example, the mean value for *PAS* following load switching events measured by R1 is 0.13, and the mean value for *PAS* following impedance fault scenarios measured by R1 is 1.42 as Table 2-5 shows. Therefore, the mean value for *PAS* following fault scenarios is 10 times the mean value following a switching event, which shows *PAS* for load switching and fault scenarios belongs to two separate clusters of data. *PAS* measured by the relays for the fault at points F1, F2, and F3, and *PAS* measured for the switching events are compared through Figure 2-11 for the grid-connected mode. In Figure 2-11, the green surfaces show the *PAS* measured by different relays for the PG, PP, PPG, and 3P faults with 40, 30, and 20 ohms fault impedance ($R_f =$ $40, 30,$ and 20 ohms); The lighter the green color the lower the fault impedance. The orange surface in Figure 2-11 shows the *PAS* measured by different relays for the DG switching scenarios. Also,

Table 2-5: Maximum *PAS* and *D* parameter measured by relays for the scenarios shown in Table 2-2 – Grid-connected mode

	Parameter	Load Switching				mean	Impedance ($R_f = 40$) Fault at point F1 (PP, PG, PPG, 3P)				mean
R1	PAS	0.28	0.105	0.065	0.097	0.13	1.37	1.37	1.45	1.50	1.42
	D	11638	4073	924	840	4368	50081	44601	51219	51958	49464
R2	PAS	0.28	0.10	0.065	0.097	0.13	1.42	1.42	1.49	1.50	1.45
	D	11636	4075	1064	977	4438	2044	307	2235	413	1249
R4	PAS	0.29	0.10	0.065	0.098	0.13	1.42	1.42	1.48	1.52	1.46
	D	11322	4191	1125	1105	4435	1432	214	1533	301	870

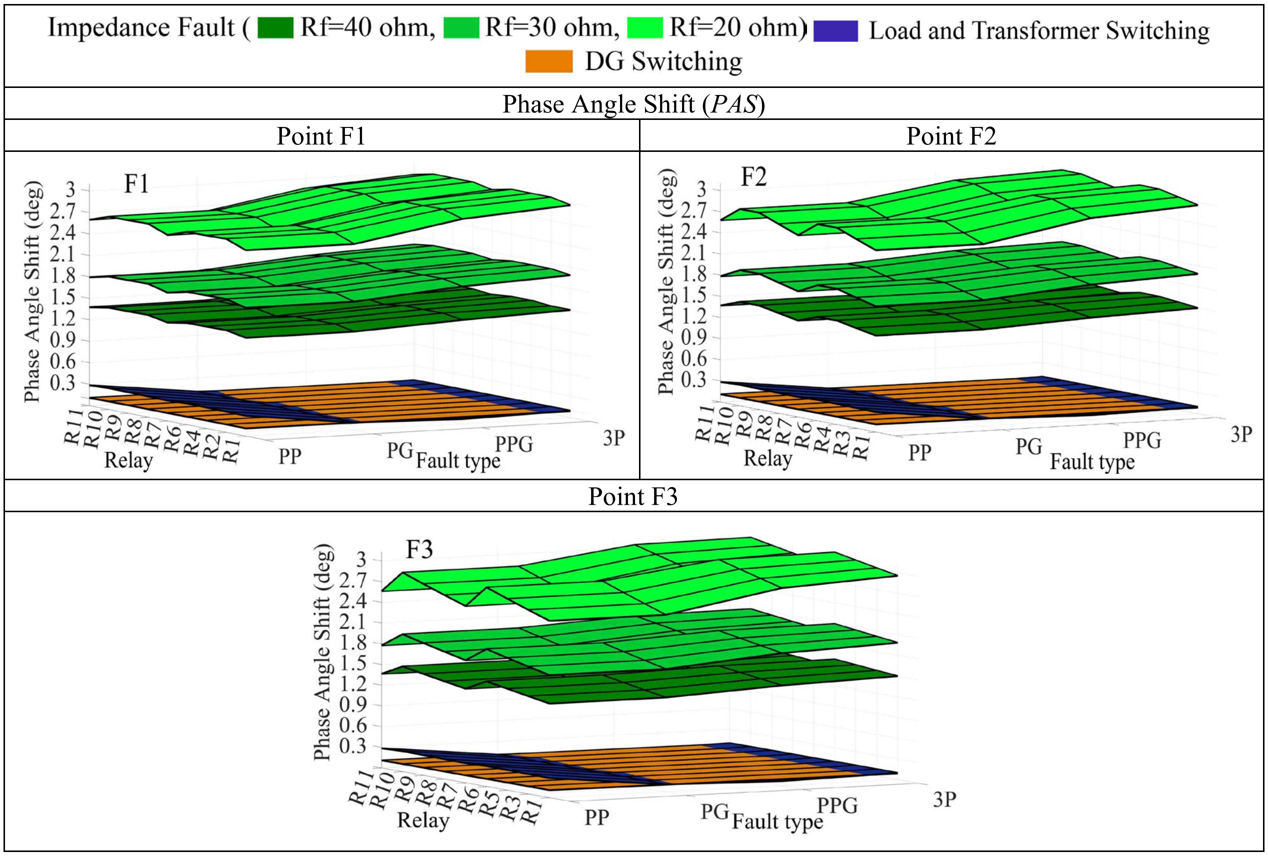

Figure 2-11: Maximum voltage *PAS* parameter measured by relays for the scenarios shown in Table 2-2 – Grid-connected mode of operation © 2021 IEEE [1]

the *PAS* measured by different relays for the transformer and load switching scenarios are shown by the dark blue surface. As it is shown in Figure 2-11, the *PAS* is 1.5 degrees for the three-phase impedance fault with $R_f = 40$ ohms and 1.37 degrees for the phase-to-phase fault with $R_f = 40$ ohms; Figure 2-11 also shows that the *PAS* increases as the fault impedance decreases; the maximum *PAS* for the switching events is 0.29 degrees (P=5MW switching) in the grid-connected mode. Also, the *PAS* for the DG switching is 0.11 degrees. Therefore, the *PAS* for the impedance fault ($R_f = 40$ ohms) is about 5 times the *PAS* for the switching events, which shows fault conditions and switching events belong to two different clusters and they can be differentiated in the grid-connected mode by using the *PAS* parameter based on the procedure explained in section 2.4. As expected, the *PAS* is smaller in the grid-connected mode compared to the island mode;

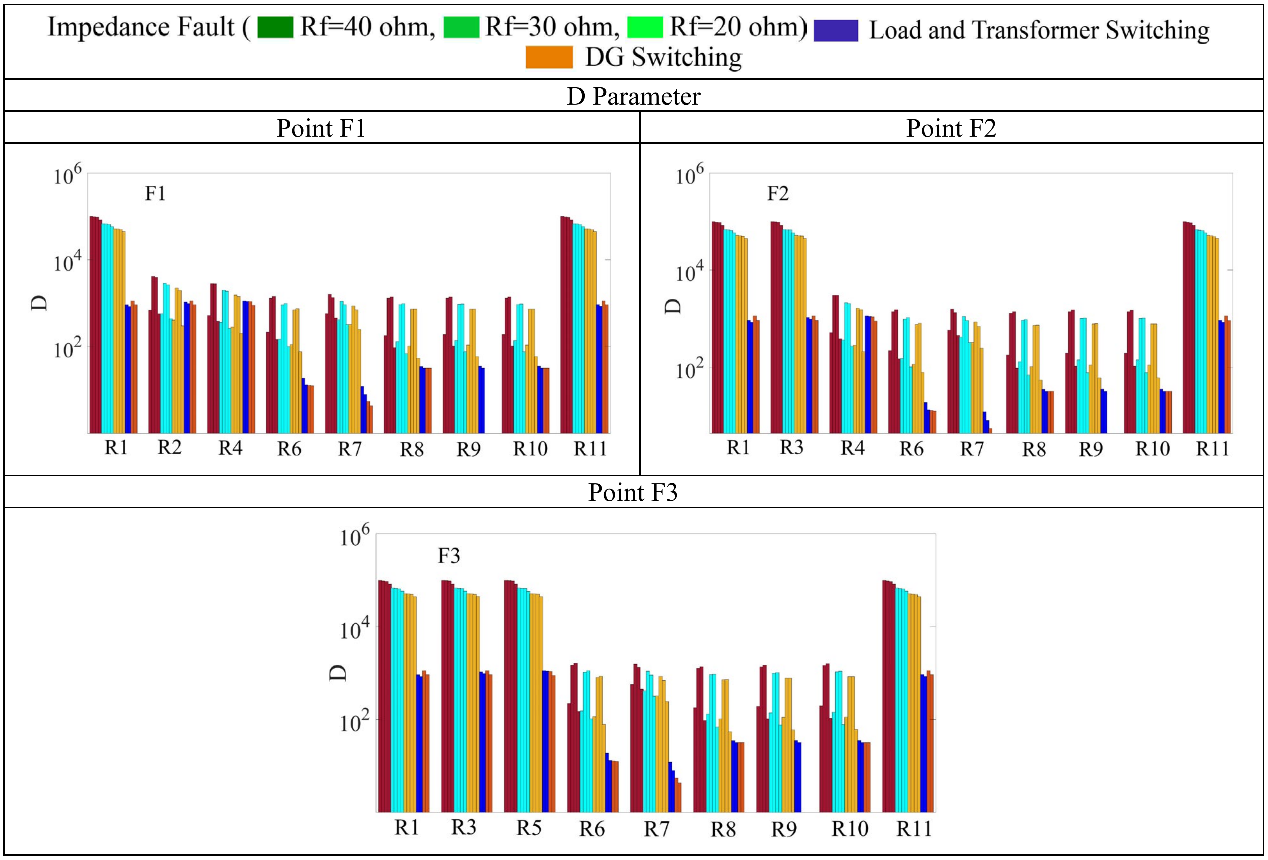

Figure 2-12: Maximum *D* parameter measured by relays for the scenarios shown in Table 2-2 – Grid-connected mode of operation © 2021 IEEE [1]

therefore, different relay characteristics should be determined for the fault detection for each mode of operation.

The *D* value measured by the relays for the switching events and different fault scenarios are compared in Figure 2-12. For the grid side relays (relays R1, R3, R5) there is a large margin between the measured *D* value for the switching events and the fault scenarios in the grid-connected mode. For example, the *D* value measured by R1 for impedance fault at point F1 is 44601 whereas the *D* value measured by R1 for switching event is 11638. It is because, in the grid-connected mode, the microgrid is connected to the power system that is able to provide a high-magnitude fault current. But, for the microgrid side relays (relays R2, R4, R6) the fault current and the switching current are close. For example, the *D* value measured by R2 for impedance fault at point F1 is 2044 whereas the *D* value measured by R2 for switching event is 977 (please note in

Table 2-5 the D parameter for switching events that have a higher value than the *D* parameter for the fault events are in the reverse direction and will be blocked by the directional element explained in chapter 3); as mentioned before, it is because these relays (relays R2, R4, R6) only see the current coming from the IBRs and IBRs cannot provide more than 1.2 to 2 pu current. Although the *D* parameter cannot be used separately to detect the fault in the grid-connected mode, the variation of the *D* parameter can be used as an indication of the fault in the system. In other words, the *D* parameter can be used to define a dynamic boundary for the relay characteristic which results in a fast fault detection scheme based on the procedure explained in section 2.4.

As shown in Figure 2-9 to Figure 2-12, by taking into account both parameters introduced above, and employing the fault detection scheme explained in section 2.4, fault can be detected in an inverter-based system in both island and grid-connected modes [1]. The relays' fault detection characteristics parameters obtained based on the fault detection scheme discussed in section 2.4 are shown in Table 2-6 for the grid-connected mode.

Table 2-6: Relays' fault detection characteristics parameters– Grid mode

Relay	Semi major axis	Semi minor axis	Eigenvector 1	Eigenvector 2	D mean	PAS mean
R1	46425.68	0.72	(-0.99, -1.14e-05)	(1.14e-05, -0.99)	8520.78	0.28
R2	47524.18	0.72	(-0.99, -1.18e-05)	(1.18e-05, -0.99)	8579.4	0.28
R3	47835.87	0.767	(-0.99, -1.17-05)	(1.17e-05, -0.99)	8892.7	0.30
R4	44464.70	0.799	(-0.99, -1.23e-05)	(1.23e-05, -0.99)	8072.9	0.28
R5	46576.74	0.758	(-0.99, -1.23e-05)	(1.23e-05, -0.99)	7966.61	0.29
R6	46528.80	0.812	(-0.99, -1.00e-05)	(1.00e-05, -0.99)	7986.49	0.27
R7	502.73	0.812	(-0.99, -0.00)	(0.00, -0.99)	79.77	0.25
R8	492.93	0.782	(-0.99, -0.00)	(0.00, -0.99)	130.62	0.24
R9	531.95	0.845	(-0.99, -0.00)	(0.00, -0.99)	137.99	0.24
R10	551.25	0.899	(-0.99, -0.00)	(0.00, -0.99)	137.78	0.24
R11	45300.75	0.757	(-0.99, -1.17e-05)	(1.17e-05, -0.99)	8162.31	0.30

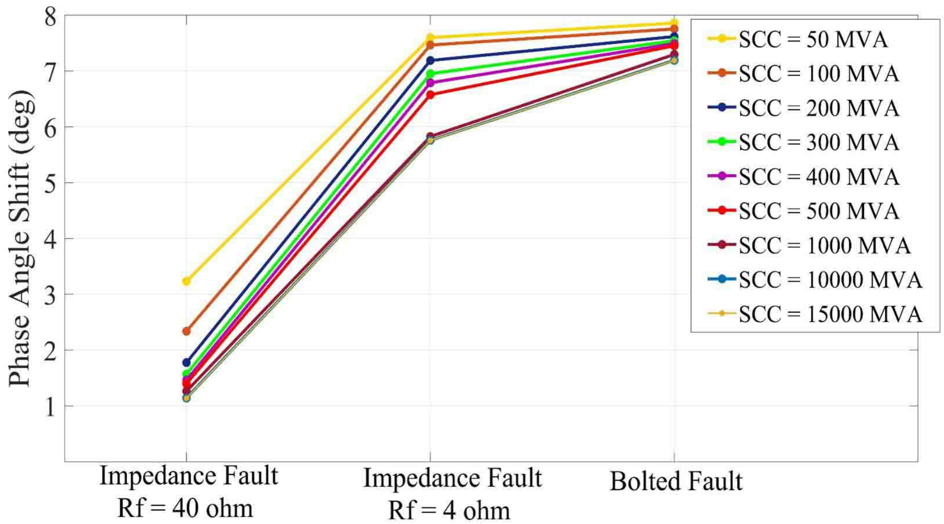

Figure 2-13: *PAS* variations with the variation of feeder SCC-Phase to ground fault (F2) © 2021 IEEE [1]

2.5.3 Case 3: The Effect of the Variation of the Short Circuit Capacity of the Grid Feeder on the Proposed Scheme

In this section, the effect of the SCC variations on the voltage *PAS* is examined. Figure 2-13 demonstrates the *PAS* variation for impedance ($R_f = 4$ ohms and $R_f = 40$ ohms) and bolted phase to ground faults when feeder SCC changes. As Figure 2-13 shows, although the phase angle shift decreases as the SCC of the grid feeder increases, there is a minimum voltage phase angle shift following a fault. In fact, there is a point that even if the short circuit capacity of the feeder increases, the voltage phase angle shift following a fault remains constant. For example, as Figure 2-13 shows, the voltage *PAS* following a fault remains constant as SCC increases from 10000 MVA to 15000 MVA. This confirms the capability of the proposed protection scheme to detect the faults in the grid-connected mode regardless of the SCC power of the grid feeder [1]. In other words, it demonstrates that *PAS* occurs following a fault as a result of the active/ reactive power variations and the changes in the grid equivalent impedance (X/R ratio) [119]–[121] regardless of the SCC power.

2.5.4 Case 4: The Procedure of Selecting Switching Scenarios to Obtain Relay Characteristic

In selecting the switching scenarios to form the E matrix and obtain relay characteristic, importance should be given to the different types of switching scenarios (such as DG, Transformer, and load switching) rather than the number of the performed scenarios. In general, the larger the sample size (the number of switching scenarios) the smaller the confidence ellipse [129]. For example, Figure 2-14 compares the relay R3 characteristic for case 1 when the number of performed scenarios increases from 5 (shown in Table 2-2) to 11. The added scenarios are shown in Table 2-7. As Figure 2-14 shows, the area of the confidence ellipse decreases as the number of the performed scenarios increases. Although by increasing the total number of the switching scenarios it is possible to determine the switching area with more precision, there is no need to perform a large number of switching scenarios to obtain the relay characteristics because of two main reasons: (a) there is a large margin between the *PAS* measured for switching events and fault condition as shown in case 1 and case 2; (b) the purpose here is to differentiate between switching events and fault conditions. Therefore, by considering the following switching scenarios to obtain relay characteristics, the required precision in determining relay characteristics for fault detection can be achieved [1].

- DG switching scenarios: connection and disconnection
- Transformer switching
- Load switching (largest load in the system)
- Load switching (active load with the maximum possible active power)
- Load switching (reactive load with the maximum possible reactive power)

Table 2-7: Added switching scenarios © 2021 IEEE [1]

L= 200kW	L= 400kW
L= 300kW	L= 450kW
L= 100kW+150kVar	L= 150kW+200kVar

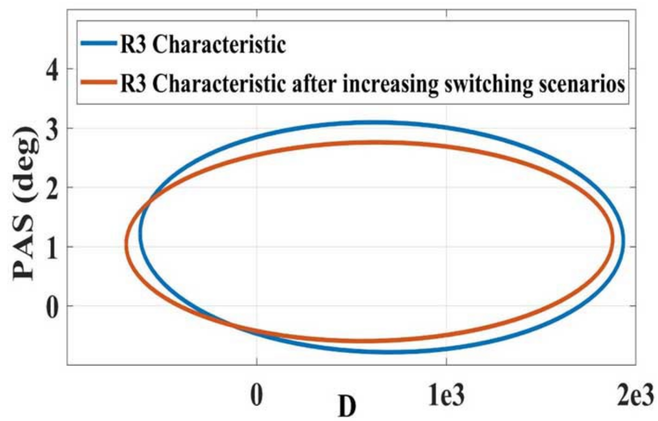

Figure 2-14: Relay's R3 characteristic © 2021 IEEE [1]

2.5.5 Case 5: The Effect of the Inertia Time Constant on the Performance of the Proposed Scheme

Because of the presence of the power electronic interfaces, microgrids have a low inertia time constant [130], [131]. Therefore, the system frequency is susceptible to change during load switching, which may result in *PAS* variations. However, the power variations during a fault are larger than power variations during a switching event. In fact, the frequency variations in the system should be very fast to result in *PAS* variations. In addition, *PAS* is associated with three main factors including (a) reactive power variation and its effect on the voltage level (b) active power interruption or variation and its effect on frequency, and (c) changes in the grid equivalent impedance (X/R ratio) [119]–[121]. During a fault, all these three factors severely change as compared to a switching event; therefore, a fault results in a larger *PAS* variation as compared to a switching event.

To demonstrate that *PAS* under fault is not comparable to *PAS* under load switching, an unlikely load-switching scenario is investigated. Load1=622kVA (P=500kW; Q=370kVar) is connected to the islanded microgrid at t= 1 sec in one step when the microgrid already has S=640kVA loading. The total generation power of the microgrid is 1050kVA. By connecting this load, the total loading of the microgrid is 1262kVA. Figure 2-15 shows the voltage and frequency of the microgrid along

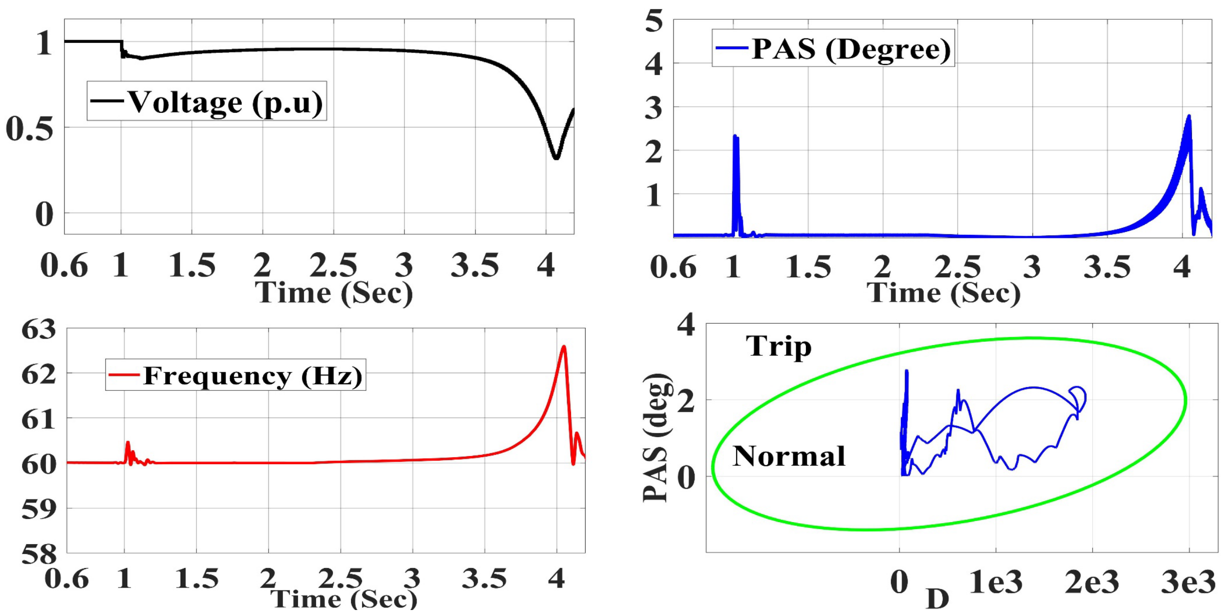

Figure 2-15: Voltage, frequency, *PAS*, and relay R5 characteristic © 2021 IEEE [1]

with *PAS* measured by relay R5. The relay R5 characteristic and the (D, *PAS*) trajectory after the switching event are also shown in Figure 2-15. As shown in Figure 2-15, because of the excessive overload, the system is not stable. However, even for this aggressive switching scenario, the (*D*, *PAS*) trajectory is inside the confidence ellipse [1].

2.5.6 Case 6: The Impact of the Presence of the Noise on the Performance of the Proposed Scheme

In this section, the impact of the noise level on the sensitivity of the proposed method is evaluated by contaminating the voltage and current signals with white Gaussian noise (SNR = 25 dB). Figure 2-16 shows the three-phase waveform with white Gaussian noise SNR= 25 dB in per unit [35], [41]. The relay R3 characteristic and the measured (*D*, *PAS*) trajectory for the switching scenarios with the presence of noise in the island and grid-connected modes are shown in Figure 2-17. As can be seen in Figure 2-17, all (*D*, *PAS*) trajectories are inside the normal operation area of the relay; therefore, the proposed scheme is able to properly operate in case of noisy measurements [1].

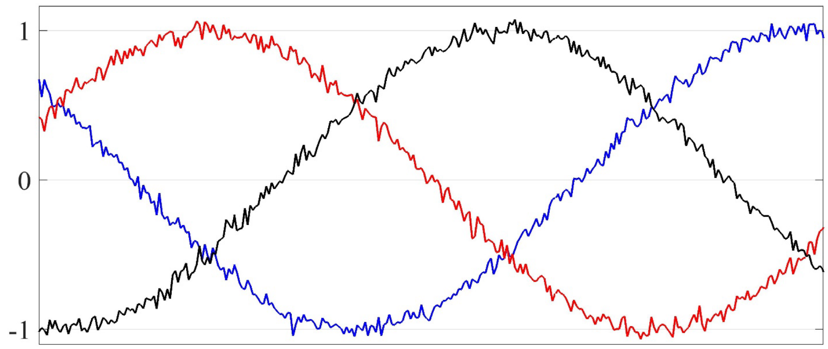

Figure 2-16: Three-phase waveform with SNR= 25 dB (in pu)

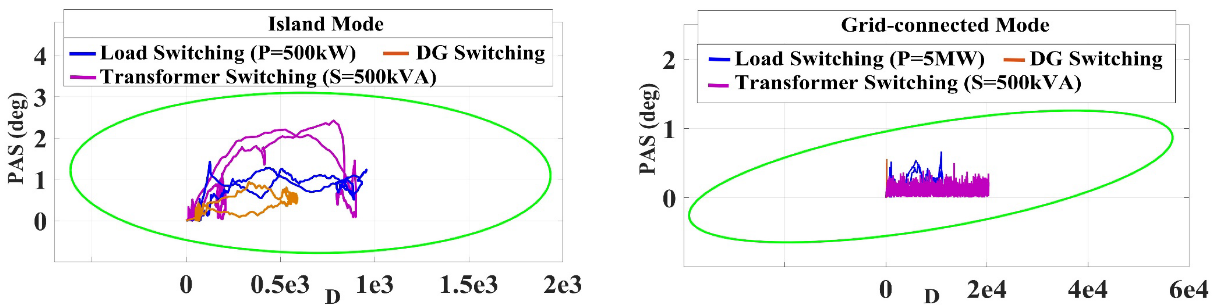

Figure 2-17: R3 characteristic and (D, *PAS*) trajectory for the switching scenarios with the presence of the noise in the island and grid-connected modes © 2021 IEEE [1]

2.5.7 Case 7: The Fault Detection Time of the Proposed Protection Scheme for the System Under Study

The fault detection time of the relays in the system under study for different fault scenarios at points F1, F2, and F3 in the island mode are shown in Figure 2-18. The fault detection time of the relays for the impedance fault with $R_f = 40$ ohms at points F1, F2, and F3 in the grid-connected mode are also shown in Figure 2-18 (green bars). As can be seen in Figure 2-18, all fault types on the feeder are detected by the primary relays in less than 5 milliseconds, which meets the design criteria (less than one AC cycle fault detection) for the fault detection element. Figure 2-18 shows that the proposed protection scheme is able to effectively detect all types of faults in both microgrid operation modes. In fact, the current prediction enables the proposed method to recognize current variations fast; also, the method can distinguish between the normal events and the fault condition by measuring the *PAS* parameter, which leads to fast detection of the fault conditions in the system.

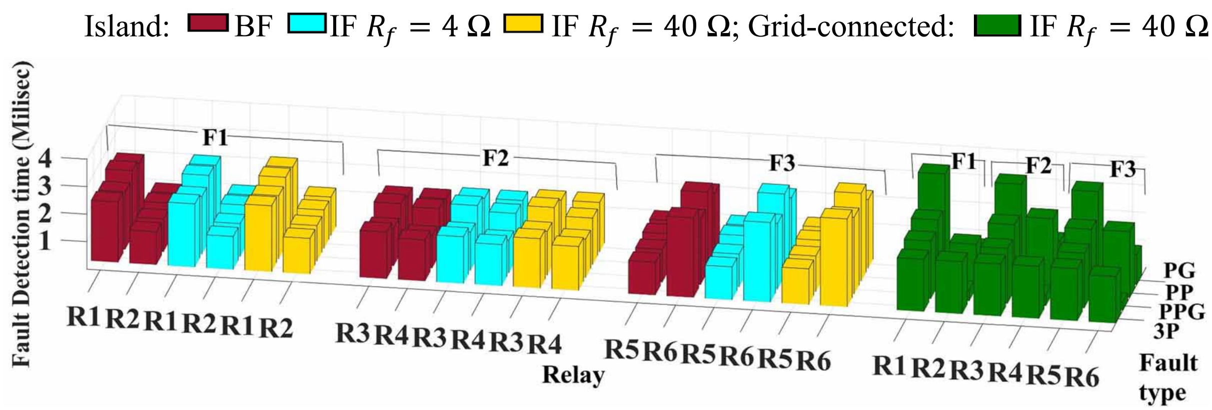

Figure 2-18: Fault detection time of the relays for the investigated fault scenarios in the island and grid-connected modes © 2021 IEEE [1]

It should be mentioned that the coordination between the relays can be achieved by employing a low-cost communication link that can transfer 2 bits of data between the relay at each end of the protection zone. When both relays at each end of the protected zone detect the fault, the faulty zone will be removed from the system [1]. The total fault clearing time which includes the time needed for communication and coordination has been discussed in chapter 5.

2.5.8 Case 8: Comparison of the Proposed Protection Scheme with Communication-assisted Overcurrent protection, and Under voltage protection

At first, the proposed method is compared with a communication-assisted dual setting overcurrent protection presented in [9]. The comparison is made for bolted three-phase faults. Table 2-8 compares the fault detection times of both methods for the fault at points F1, F2, and F3. As Table 2-8 shows, for the proposed method, the primary relays detect the bolted three-phase fault at point F1 in 0.0022 and 0.0012 seconds in the island mode; for communication-assisted overcurrent protection [9], the primary relays detect the fault at point F1 in 10.15 and 0.35 seconds in the island mode. This shows that overcurrent-based protection methods are ineffective in microgrids that integrate inverter-based DERs. As mentioned earlier, depending on the inverter control design, the inverter may become disconnected from the system in the first 4 to 10 AC cycles after fault [13]; therefore, protection methods that have a fault detection time greater than 4 cycles can be considered ineffective for microgrids in the presence of inverter-based DERs. Also, as the fault

Table 2-8: Comparison of the fault detection time for bolted three-phase fault © 2021 IEEE [1]

		Fault Detection time (Sec)			
		Island		Grid-connected	
Fault	**Primary Relays**	**Method in** [9]	**Proposed Method**	**Method in** [9]	**Proposed Method**
F1	R1	10.15	0.0022	0.44	0.0019
	R2	0.35	0.0012	0.35	0.0019
F2	R3	2.3	0.0015	0.24	0.0019
	R4	0.55	0.0015	0.55	0.0019
F3	R5	0.19	0.0029	0.04	0.0019
	R6	5.94	0.0029	5.94	0.0017

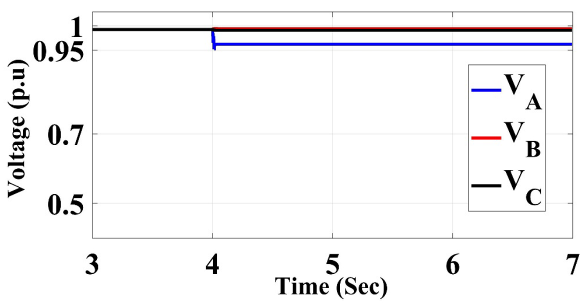

(a)

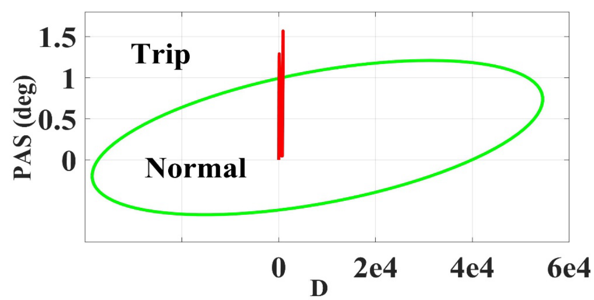

(b)

Figure 2-19: a) the voltage magnitudes measured by relay R6; (b) relay R6 characteristic and (D, *PAS*) trajectory for impedance PG fault ($R_f = 40$ ohms) at point F3 © 2021 IEEE [1]

impedance increases the fault detection time of the overcurrent-based protection methods increase, and in most cases, the overcurrent protection cannot detect the impedance fault. But, as shown in Figure 2-18 the proposed method detects all fault types in less than 1 AC cycle. Figure 2-19(a) shows the voltage magnitudes measured by relay R6 when an impedance PG fault ($R_f = 40$ ohms) is applied to the system under study at t= 4 sec at point F3. As shown in Figure 2-19(a), all voltages are above 0.95 per unit and under-voltage protection cannot detect the fault. Relay R6 characteristic and (D, PAS) trajectory of the fault is demonstrated in Figure 2-19(b). Both R5 and R6 detect this fault in less than 5 milliseconds as Figure 2-18 shows [1].

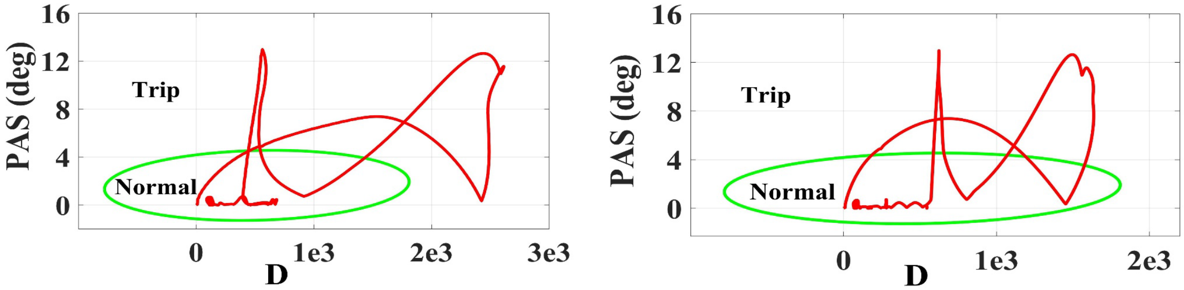

(a) (b)

Figure 2-20: (a) Relay R5 characteristic, (b) relay R6 characteristic, and (D, *PAS*) trajectories for the impedance PP fault (R_f = 40 ohms) at point F3 (Case 9) © 2021 IEEE [1]

Table 2-9: Relays' fault detection time (Sec) for Case 9 and Case 10 (Islanded mode) © 2021 IEEE [1]

		Case 9 (Droop-control)				Case 10 (in the presence of SG)			
		IF (R_f = 40 ohms)				IF (R_f = 40 ohms)			
		3P	PG	PP	PPG	3P	PG	PP	PPG
F1	R1	.0052	.0077	.0051	.0052	.0064	.0090	.0055	.0062
	R2	.0053	.0055	.0052	.0053	.0078	.0084	.0055	.0045
F2	R3	.0051	.0066	.0050	.0050	.0060	.0081	.0055	.0050
	R4	.0051	.0063	.0050	.0051	.0104	.0097	.0054	.0057
F3	R5	.0050	.0051	.0049	.0050	.0053	.0068	.0053	.0042
	R6	.0049	.0050	.0049	.0049	.0104	.0107	.0053	.0065

2.5.9 Case 9: Performance of the Proposed Method in a Droop-controlled System

In this section, the performance of the proposed protection scheme is examined when the droop-control strategy is employed in the system under study. In the droop control strategy, the output active and reactive power of the inverter depend on the frequency and magnitude of the output voltage, and they are regulated based on a droop characteristic [99]. In this case, DG1 and DG4 are working in droop-control mode, and DG2 and DG3 are working in PQ mode. The load switching scenarios shown in Table 2-2 are performed to obtain the relay characteristics based on the procedure explained in section 2.4. Relays R5 and R6 characteristics and (D, PAS) trajectory for the impedance PP fault with R_f = 40 ohms in island mode are demonstrated in Figure 2-20. Table 2-9 shows the relay fault detection time for the impedance 3P, PG, PP, and PPG faults with R_f = 40 ohms at points F1, F2, and F3 in the island mode for case 9. As Table 2-9 shows, the fault detection time of all relays are less than 16 milliseconds for impedance faults with R_f = 40 ohms

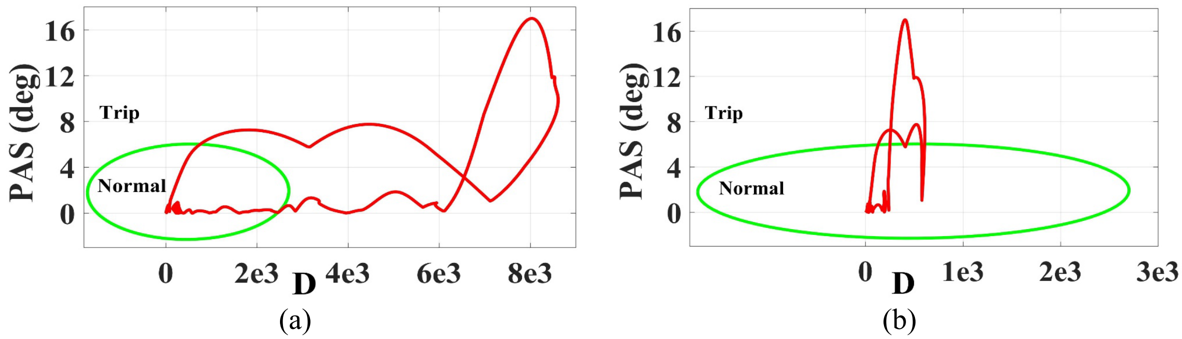

Figure 2-21: (a) Relay R5 characteristic, (b) relay R6 characteristic, and (D, *PAS*) trajectories for the impedance PP fault (R_f = 40 ohms) at point F3 (case 10) © 2021 IEEE [1]

at point F1, F2, and F3 in the island mode of operation. Therefore, this case study confirms the high performance of the proposed protection scheme when the droop control strategy is employed in the system [1].

2.5.10 Case 10: Performance of the Proposed Method in the Presence of a Synchronous Generator in the Microgrid

To examine the performance of the proposed method in the presence of a synchronous generator in the microgrid, BES (DG1) is replaced with a 0.5 MVA synchronous generator. In this case, the synchronous generator forms the voltage and frequency of the microgrid in the island mode, and DG2 to DG 4 are working in PQ mode. The load switching scenarios depicted in Table 2-2 are performed to obtain the relay characteristics based on the procedure explained in section 2.4. Relays R5 and R6 characteristics and (D, PAS) trajectory for the impedance PP fault with R_f = 40 ohms in island mode are shown in Figure 2-21. Table 2-9 demonstrates the relay fault detection time for impedance 3P, PG, PP, and PPG faults with R_f = 40 ohms at points F1, F2, and F3 in the island mode for case 10. As Table 2-9 depicts, the fault detection time of all relays are less than 16 milliseconds for impedance faults with R_f = 40 ohms at point F1, F2, and F3 in the island mode of operation, which verifies the performance of the method in the presence of the synchronous generator in the microgrid [1].

2.5.11 Case 11: Sensitivity of the Confidence Ellipse to Changes in the Microgrid Arrangement

Regular microgrid arrangement changes such as DG switching, overload condition, the connection of a new load or transformer, and disconnection of a load are considered in the procedure of determining the relay characteristic. In fact, the confidence ellipse determines the area of the switching events, and as shown in section 2.5.5, even an aggressive switching event does not affect the performance of the method. Therefore, there is no need to recalculate the relay setting in case of these arrangement changes. However, it may be needed to recalculate the relay setting if the voltage-frequency control strategy of the microgrid changes (for example, when the battery is replaced with a synchronous generator). Figure 2-22 compares relay R3 confidence ellipse for the first case study and case 10. As Figure 2-22 shows, the confidence ellipse is larger in the presence of a synchronous generator in the system. Instead of recalculating the relay settings, it is also possible to set the relay characteristic based on the case scenario with the largest ellipse (worst-case scenario). In case of determining the relay characteristics based on the case scenario with the largest ellipse, there is no need to change the relays' setting if the control strategy changes; but, a protection study is needed to make sure that selecting the relay characteristics based on the worst-case scenario does not affect the fault detection procedure. Between the three control strategies investigated in case 1 (Master-Slave), case 9 (droop-control), and case 10 (synchronous generator), the relays characteristic obtained for case 10 have the largest obtained ellipses. To examine the performance of the proposed method when unique group settings is chosen for different control strategies, all relays' settings are chosen based on the settings obtained in case 10; then, the proposed method is reexamined with the new settings for case 1 and case 9. Table 2-10 shows the relays fault detection time for the impedance 3P, PG, PP, and PPG faults with $R_f = 40$ ohms at points F1, F2, and F3 in the island mode for case 1 and case 9 when all the relay characteristics are set based on the settings obtained in case 10. As shown in Table 2-10, although the fault detection time of the relays slightly increases compared to Table 2-9, all fault detection times are still less than 16 milliseconds when the relays' settings are chosen based on the settings obtained in case 10. Therefore, the system under study can be protected using a unique group of relays' setting in case 1, case 9, and case 10 [1].

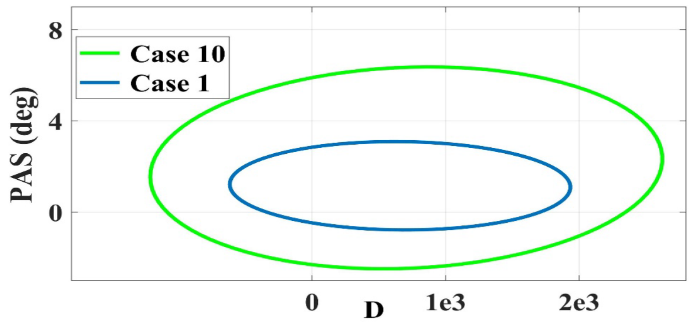

Figure 2-22: Relay's R3 characteristic © 2021 IEEE [1]

Table 2-10: Relays' fault detection time (Sec) for Case 1 and Case 9 (Islanded mode) using the relay setting obtained in case 10 © 2021 IEEE [1]

		Case 1 (Master-slave)				Case 9 (Droop-control)			
		IF (R_f = 40 ohms)				IF (R_f = 40 ohms)			
		3P	PG	PP	PPG	3P	PG	PP	PPG
F1	R1	.0069	.0067	.0046	.0069	.0085	.0087	.0056	.0098
	R2	.0069	.0055	.0046	.0066	.0074	.0065	.0057	.0070
F2	R3	.0048	.0054	.0045	.0047	.0080	.0076	.0056	.0079
	R4	.0072	.0067	.0035	.0072	.0079	.0074	.0057	.0077
F3	R5	.0043	.0047	.0034	.0042	.0077	.0071	.0055	.0075
	R6	.0073	.0074	.0034	.0077	.0081	.0081	.0055	.0082

2.6 Conclusion

This chapter proposed a fault detection element for the microgrid. *PAS* and *D* parameters were proposed, and the Mahalanobis Distance was employed to detect the fault in microgrids. Then the method was tested under different conditions in a microgrid system in the island and grid-connected modes. The benefits of the proposed fault detection element are summarized below based on the obtained simulation results.

- The proposed fault detection element can detect the fault in the island and grid-connected modes.
- The proposed element can detect the fault in a microgrid that is working under different control strategies such as master-slave, droop, and in the presence of synchronous generator.

- The fault detection time of the proposed element is about one AC cycle (16 milliseconds) which is much faster than the over-current protection.
- The proposed element can detect different types of faults including impedance faults.

Chapter 3 : Directional Element

3.1 Introduction

As discussed in chapter 1, in addition to fault detection, any effective microgrid protection method requires correct identification of fault current direction. However, the existing directional elements are designed based on the behavior of the Synchronous Generator (SG), and their performance is not reliable in the presence of IBRs in microgrids [82]. Therefore, in this chapter:

(a) Some of the problems associated with the conventional directional elements in the presence of inverter-based DERs in microgrids are demonstrated.
(b) A new directional element for microgrids is presented.
(c) The performance of the proposed directional element is compared with the conventional directional elements.

3.2 Conventional Directional Elements' Challenges in the Presence of Inverter-based DERs in Microgrid

In this section, the problems with the conventional positive sequence, negative sequence and phase directional elements in the presence of inverter-based DERs in the microgrids are discussed by providing simulation results on a test microgrid system. The system under study is shown in Figure 3-1. MATLAB Simulink is employed to model The system under study. The time step used for performing the simulation is 25 microseconds. This system is a double feeder microgrid inspired by the Canadian urban benchmark distribution system [105]. As shown in Figure 3-1, The system includes three type 4 wind turbines and a Battery Energy Storage (BES). Table A-2 shows the system parameters. A detailed description of the system and the inverter control designs can be found in sections A.2, A.4, and A.5 of the Appendix. The microgrid control strategy is based on the Master-slave control strategy; DG 1 (BES) is the Master controller working in Voltage-Frequency (VF) mode, whereas DG2 to DG4 are the slaves working in PQ mode. More information on the Master-slave control strategy can be found in [98]. The inverters' control systems are based on the conventional dq (direct- quadrature) control strategy for voltage source

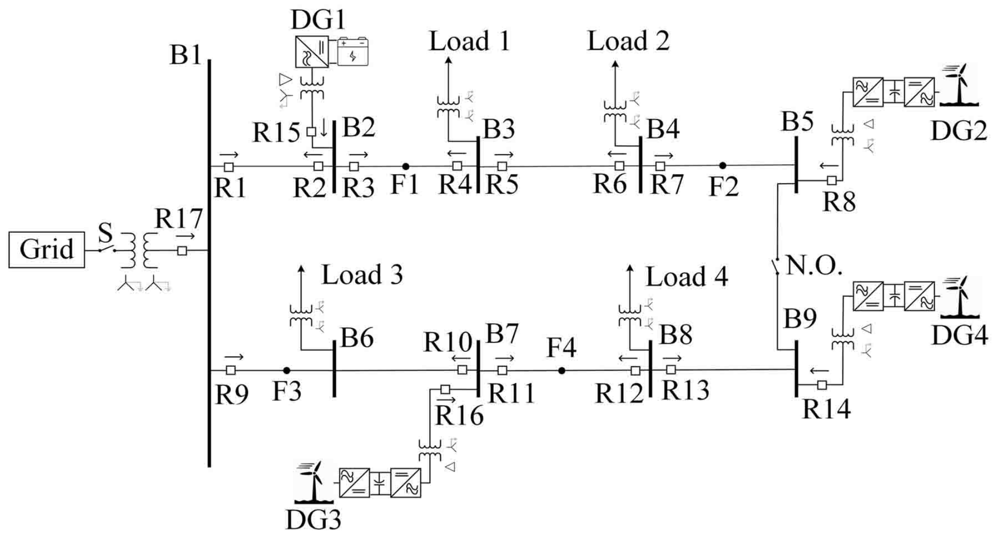

Figure 3-1: the double feeder microgrid

converters [98], [99]. The system is solidly grounded; the DG transformers configuration are Δ/Yg, and the grid and load transformers configuration are Yg/Yg. The protection relays installed in the system are shown in Figure 3-1.

3.2.1 Negative Sequence Directional Element

The negative sequence directional element is commonly employed to determine the current direction during unbalanced faults. The negative sequence directional element operates based on (3-1)[82], [132].

$$T^{-} = |V^2||I^2|\cos(\angle - V^2 - (\angle I^2 + \angle Z^1)) \tag{3-1}$$

where Z^1 is the positive sequence impedance of the line to be protected; I^2 and V^2 demonstrate the negative sequence current and voltage, respectively. In (3-1), if the angle of the cosine term ($\angle T^-$) is between -90 and 90 degrees, the element indicates a forward fault; otherwise, the element indicates a backward fault.

The negative sequence directional element is expected to operate correctly only if the source has a similar pattern in the negative sequence domain as the conventional synchronous generator-based source. Since a synchronous generator is modeled by an impedance in the negative-sequence

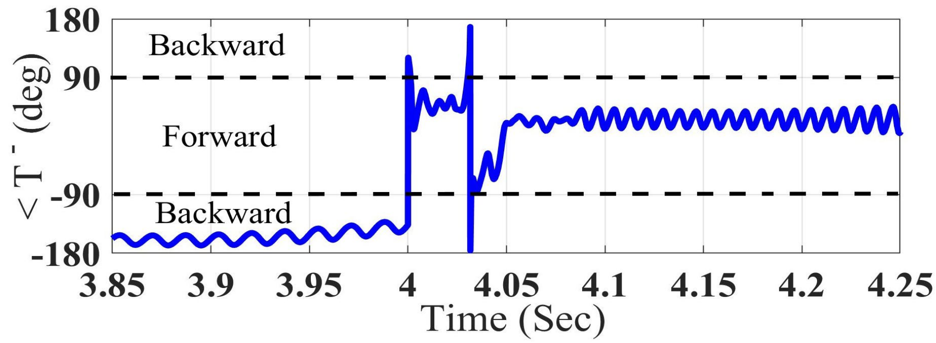

Figure 3-2: The output of negative sequence directional element ($\angle T^{-}$) for relay R13

circuit [15], [82], the negative-sequence voltage caused by the fault and the loop impedance determine the negative-sequence current. On the contrary, inverter-based DGs operate as current-controlled resources, and a generic voltage source converter control system usually suppresses negative sequence current as explained in section 1.1.3. The negative sequence directional element is prone to mal-operation in the presence of inverter-based DERs in a microgrid because of the absence of negative sequence current in microgrids incorporating inverter-based DERs [4], [82]. As an illustration, a bolted PP fault is applied to the islanded microgrid shown in Figure 3-1 at point F4 at t=4 sec. The fault is reverse for R13. Therefore, R13 should not issue a trip, and the feeder that connects bus B8 to bus B9 should not be disconnected. However, the angle of the cosine term in (3-1), named $\angle T^{-}$, is 30 degrees after the initial fault transients as Figure 3-2 demonstrates. Therefore, if a negative sequence directional element is employed here, R13 detects a forward fault incorrectly, and it can potentially issue a trip and disconnect the feeder that connects bus B8 to bus B9.

3.2.2 Positive Sequence Directional Element

When the negative sequence quantities are not present or cannot be used reliably, the positive sequence directional element is employed to determine the current direction. The positive sequence directional element operates based on (3-2) [82], [132].

$$T^{+} = |V^{1}||I^{1}|\cos(\angle V^{1} - (\angle I^{1} + \angle Z^{1})) \tag{3-2}$$

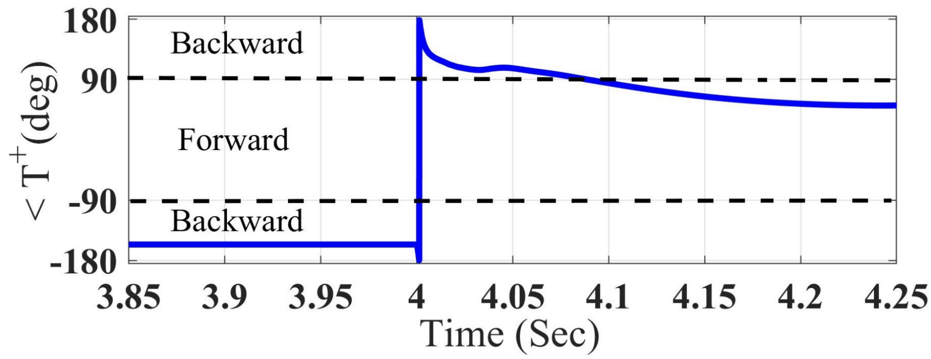

Figure 3-3: The output of positive sequence directional element ($\angle T^+$) for relay R1

where Z^1 is the positive sequence impedance of the line to be protected; I^1 and V^1 demonstrate the positive sequence current and voltage, respectively. In (3-2), if the angle of the cosine term ($\angle T^+$) is between -90 and 90 degrees, the element indicates a forward fault; otherwise, the element indicates a backward fault.

The positive sequence directional element is also prone to malfunction in the presence of inverter-based DERs in microgrids mainly because of the inverters' limited fault current especially when the microgrid is working in the grid-connected mode. As an illustration, a bolted 3P fault is applied to the grid-connected microgrid shown in Figure 3-1 at point F4 at t=4 sec. The fault is reverse for R1. Therefore, R1 should not issue a trip, and the feeder that connects bus B1 to bus B2 should not be disconnected. However, the angle of the cosine term in (3-2), named $\angle T^+$, is 85 degrees after the initial fault transients as Figure 3-3 demonstrates, which means the positive sequence directional element incorrectly shows a forward fault. Therefore, if a positive sequence directional element is employed here, R1 incorrectly detects a forward fault and can potentially issue a trip and disconnect the upper feeder that connects bus B1 to bus B2.

3.2.3 Phase Directional Element

The phase directional element is inaccurate when there is zero sequence dominated fault current in the system. However, this directional element is still used. The phase directional element operates based on (3-3) [82], [133].

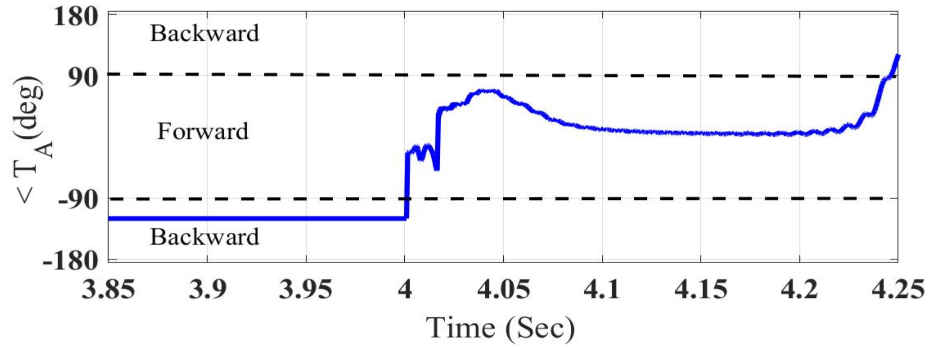

Figure 3-4: The output of phase directional element ($\angle T_A$) for relay R1

$$T_A = |V_{BC}||I_A| \cos(\angle V_{BC} - (\angle I_A + \angle Z^1)) \tag{3-3}$$

Similar to T^+ and T^-, if the angle of the cosine term ($\angle T_A$) is between -90 and 90 degrees, the element indicates a forward fault; otherwise, the element indicates a backward fault. As previously shown, the sequence-based directional elements are unreliable in the presence of inverter-based DERs in microgrids, and since the phase directional element is composed of the sequence elements, the phase directional element is also unreliable in the presence of inverter-based DERs in the system. As an illustration, a bolted PP fault is applied to the islanded microgrid shown in Figure 3-1 at point F4 at t=4 sec. The fault is reverse for R1; therefore, R1 should not issue a trip, and the feeder that connects bus B1 to bus B2 should not be disconnected. However, the angle of the cosine term in (3-3), named $\angle T_A$, is 85 degrees after the initial fault transients as Figure 3-4 demonstrates. Therefore, if a phase directional element is employed here, R1 incorrectly detects a forward fault and can potentially disconnect the upper feeder that connects bus B1 to bus B2.

3.3 Proposed Directional Element

As discussed, the directional elements play a crucial role in the protection of systems with bidirectional fault currents. Positive-sequence, negative-sequence, zero-sequence, and phase directional elements are the most common directional elements. However, as discussed above, positive-sequence, negative-sequence, and phase directional elements are all subject to malfunction in the presence of inverter-based DERs in microgrids under fault conditions because of the limited fault current of the inverter-based recourses and their small negative-sequence current [3], [4]. The zero-sequence directional element can be used in grounded microgrids, but it is not able to identify the fault direction during phase-to-phase and balanced faults [31], [82]. Therefore, in this section, a new directional element is proposed to determine the current direction under fault conditions in microgrids. The proposed element relies on the positive sequence directional element to determine the current direction during normal operation and employs the Current Phase Shift (*CPS*) to determine the current direction during fault. The proposed directional element is explained in the following.

Assume that the reactive current generated by the inverter during normal operation is Q_1 and the reactive power generated by the inverter during fault is Q_2. Therefore, Considering the capabilities of the inverter on whether it can provide dynamic voltage support during a fault by injecting reactive current or not [116], one of the following cases occurs in a microgrid integrating inverter-based DERs following a fault.

Case (1): IBRs start generating reactive current and the current flow direction remains unchanged.

In this case, since the current generated by IBRs is more active during normal operation, the phase angle of the current is close to zero. Following a fault, IBRs start generating reactive current. Therefore, the fault current in the line will be more inductive, and the phase angle of the current moves towards $-\pi/2$ radians. The $\emptyset$ angle is less than $\pi/2$ radians for this case as shown in Figure 3-5.

$$\angle I_{pre-fault} = \theta_1 \tag{3-4}$$
$$\angle I_{Fault} = \theta_2 \tag{3-5}$$
$$Q_2 > Q_1 \Rightarrow \theta_1 < \theta_2 < \pi/2 \tag{3-6}$$
$$\Rightarrow \left|\theta_2 - \theta_1\right| < \pi/2 \tag{3-7}$$
$$\Rightarrow \left|\angle I_{Fault} - \angle I_{pre-fault}\right| < \pi/2 \tag{3-8}$$

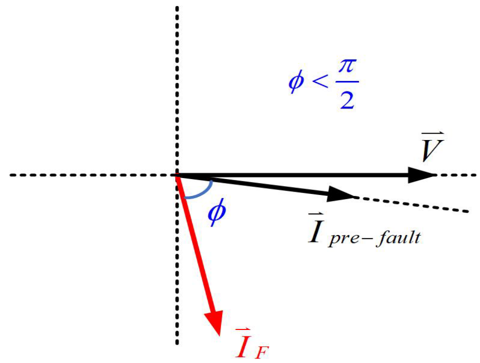

Figure 3-5: Phasor diagram: IBR generates reactive current; current flow direction remains unchanged

Case (2): IBRs generate reactive current and the current flow direction changes.

As shown in Figure 3-6, the difference between this case and case (1) is that the fault current is reversed, and the $\emptyset$ angle is greater than $\pi/2$ radians.

$$\theta_{2\,(case\,2)} = \theta_2 + \pi \tag{3-9}$$

$$\Rightarrow \theta_2 - \theta_1 < \pi/2 - \pi \tag{3-10}$$

$$\Rightarrow |\theta_2 - \theta_1| > \pi/2 \tag{3-11}$$

$$\Rightarrow \left| \angle I_{Fault} - \angle I_{pre-fault} \right| > \pi/2 \tag{3-12}$$

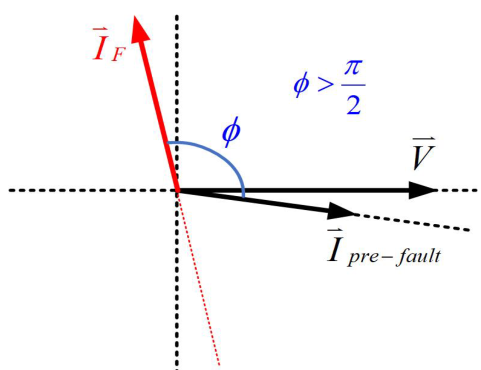

Figure 3-6: Phasor diagram: IBR generates reactive current; current flow direction changes

Case (3): IBR is working in constant PQ mode and keeps the power factor constant during fault and the current direction is unchanged.

In this case, since the IBR keeps the power factor constant, the ∅ angle is zero when the current flow direction remains unchanged after the fault occurs as shown in Figure 3-7.

$$Q_2 = Q_1 \Rightarrow \theta_1 = \theta_2 \tag{3-13}$$
$$\Rightarrow |\theta_2 - \theta_1| = 0 < \pi/2 \tag{3-14}$$
$$\Rightarrow |\angle I_{Fault} - \angle I_{pre-fault}| < \pi/2 \tag{3-15}$$

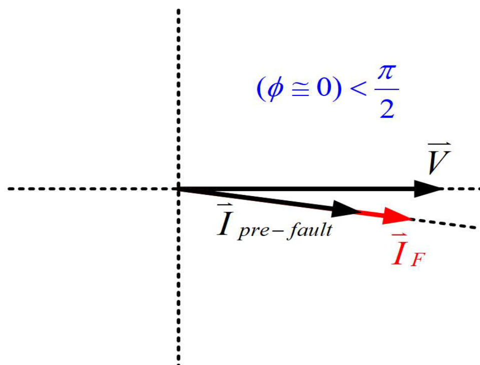

Figure 3-7: Phasor diagram: IBR works with constant power factor; current flow direction remains unchanged

Case (4): IBR is working in constant PQ mode and keeps the power factor constant during fault and the current direction changes.

As shown in Figure 3-8, the difference between this case and case (3) is that the fault current flow is reversed, and the ∅ angle is greater than $\pi/2$ radians.

$$\theta_{2\,(case\,4)} = \theta_2 + \pi \tag{3-16}$$
$$\Rightarrow |\theta_2 - \theta_1| = \pi > \pi/2 \tag{3-17}$$
$$\Rightarrow |\theta_2 - \theta_1| > \pi/2 \tag{3-18}$$
$$\Rightarrow |\angle I_{Fault} - \angle I_{pre-fault}| > \pi/2 \tag{3-19}$$

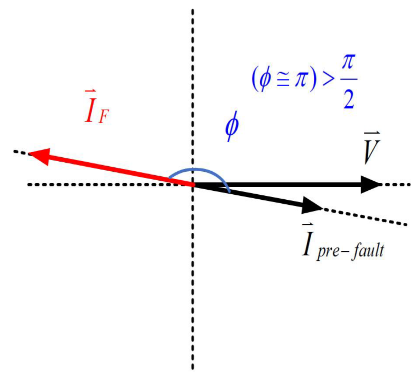

Figure 3-8: Phasor diagram: IBR works with constant power factor; current flow direction changes

From Figure 3-5 to Figure 3-8, it can be concluded that $\emptyset$ angle is less than $\pi/2$ radians when the flow direction of the positive sequence current is unchanged, and it is more than $\pi/2$ radians when the flow direction of the positive sequence current changes.

When a fault occurs in the system, the proposed directional element determines the current direction by knowing the direction of the current before the fault and measuring the positive sequence *CPS*. *CPS* is defined here as the phase angle shift of the fundamental component of two consecutive positive sequence current cycles. Positive sequence current is selected here as it is present in the system in all fault types.

The procedure of calculating *CPS* is the same as the procedure explained in section 2.3.1.1 for the *PAS* parameter, but for *CPS* calculation $\alpha = K$ as shown in (3-20) and (3-21).

$$\phi = a\cos\left(\frac{\tilde{I}^{+}_{present} \cdot \tilde{I}^{+}_{past}}{\left|\tilde{I}^{+}_{present}\right|\left|\tilde{I}^{+}_{past}\right|}\right) \tag{3-20}$$

$$CPS = \left|\frac{\phi \times 180}{\pi}\right| \tag{3-21}$$

The change in the current flow direction causes a significant step-change in *CPS* (more than 90 degrees as explained above); if *CPS* experiences a significant step-change, it means the current direction has changed as a result of a fault.

In the proposed directional element, the positive sequence torque angle ($\angle T^{+}$) is employed to determine the direction of the current under normal operating conditions. If $-90 < \angle T^{+} < 90$, it indicates a forward current direction, and if $\angle T^{+} < -90, or\ \angle T^{+} > 90$, it indicates a reverse current direction. $\angle T^{+}$ is defined as (3-22) shows.

$$\angle T^{+} = \angle V^{1} - (\angle I^{1} + \angle Z^{1}) \tag{3-22}$$

where I^1 and V^1 demonstrate positive sequence current and voltage, and Z^1 is the positive sequence impedance of the line to be protected [132].

It is worth mentioning that although the positive sequence torque angle is not reliable in the presence of inverter-based DERs in microgrids under fault conditions, it can be reliably used to determine the current direction during normal operation, especially in microgrids where load angles are small [132]. If the current becomes zero during the normal operation, the last current vector will be saved as the default value to determine the current direction; this value will be updated as soon as the current flows through the line. The logic of the proposed directional element is shown in Figure 3-9 and Figure 3-10. The current direction during normal operation is determined by $\angle T^{+}$. When a fault occurs, the fault detection element sends a signal to the directional element; then, the *CPS* for the positive sequence current is compared to a threshold value to determine if the current direction changed following the fault as compared to the current direction during the normal operation. The threshold value must be higher than 90 degrees as explained above and can be chosen between 90 degrees to 95 degrees based on the system condition. Here, 95 degrees is selected as the threshold value for the directional element as shown in Figure 3-9; in the next sections, the threshold value selection will be discussed in detail. If the *CPS* for positive sequence current is greater than 95 degrees, it means the current direction has changed because of the fault. If the *CPS* is less than 95 degrees, it shows that the current direction after the fault is the same as the direction determined by $\angle T^{+}$ during normal operation. The output of the proposed directional element logic shown in Figure 3-9 is 1 for the forward faults and is 0 for the reverse faults.

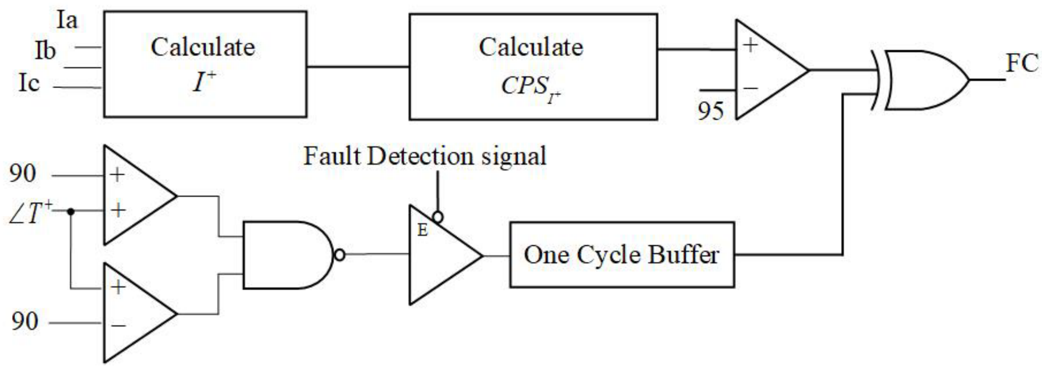

Figure 3-9: The logic of the proposed directional element (logic circuit diagram)

$$\boxed{-90 \le \angle T^{+}_{\text{Before Fault}} \le 90} \ \& \ \boxed{CPS_{\text{During Fault}} \ge 95} \rightarrow \boxed{\text{Backward Fault}}$$

$$\boxed{-90 \le \angle T^{+}_{\text{Before Fault}} \le 90} \ \& \ \boxed{CPS_{\text{During Fault}} < 95} \rightarrow \boxed{\text{Forward Fault}}$$

$$\boxed{\angle T^{+}_{\text{Before Fault}} \le -90 \ or \ \angle T^{+}_{\text{Before Fault}} \ge 90} \ \& \ \boxed{CPS_{\text{During Fault}} \ge 95} \rightarrow \boxed{\text{Forward Fault}}$$

$$\boxed{\angle T^{+}_{\text{Before Fault}} \le -90 \ or \ \angle T^{+}_{\text{Before Fault}} \ge 90} \ \& \ \boxed{CPS_{\text{During Fault}} < 95} \rightarrow \boxed{\text{Backward Fault}}$$

Figure 3-10: The logic of the proposed directional element

3.4 The Effect of Measurement Accuracy on the Performance of the *CPS* Filter and Threshold Value Selection

In this section, the effect of measurement accuracy on the performance of the *CPS* filter is investigated under two scenarios. First, the *CPS* is calculated when a 20% uniform random error is added to the current samples measured by the relay. The error is added to the current samples based on (3-23). In (3-23), $I^{e}_{(in\ pu)}$ is the measured current sample with error in per unit; $I_{(in\ pu)}$ is the measured current sample in per unit. Second, the current samples are contaminated with white Gaussian noise (SNR = 25 dB) and *CPS* is calculated [35], [41]. Then *CPS* threshold value selection is discussed.

$$I^{e}_{(in\,pu)} = I_{(in\,pu)} \pm (0.2 * Rand(0,1)) \tag{3-23}$$

Figure 3-11(a) demonstrates the measured current waveform by the relay for 0%, 20% measurement error, and when white Gaussian noise with SNR = 25 dB is added to the current signal. Figure 3-11(b) shows the *CPS* under normal operating mode corresponding to the current measurement with 0 and 20% measurement errors and with SNR = 25 dB. As shown by Figure 3-11(b), the maximum *CPS* error is about 4 degrees. Therefore, measurement error does not have a significant impact on the performance of the *CPS* filter. However, the measurement error should be considered when selecting the threshold value for the *CPS* in the proposed directional element.

As discussed in section 3.3 and shown through Figure 3-5 to Figure 3-8, when the *CPS* is greater than 90 degrees, it indicates that the direction of the current has changed during a fault.

As discussed above, in an environment with high measurement error (up to SNR =25dB) the *CPS* filter may have up to 4 degrees error when calculating the current phase shift. In addition, in a distribution system, the power factor is usually between 0.98 to 0.99 in the best-case scenario, and the current is expected to lag the voltage by at least 4 to 5 degrees. As a result, *CPS* is more than 95 degrees when the current direction changes in an actual distribution system. Therefore, to account for the measurement inaccuracy, 95 degrees threshold value is selected for *CPS*. It is worth mentioning that the recommended value is validated through 528 scenarios in both island and grid-connected modes by using MATLAB Simulink, and through 192 scenarios in the C-HIL setup for three different microgrid configurations.

It should be mentioned that if the system power factor is greater than 0.996 at the relay point, the *CPS* value should be lower than 95 degrees with a minimum of 90 degrees considering the measurement inaccuracy.

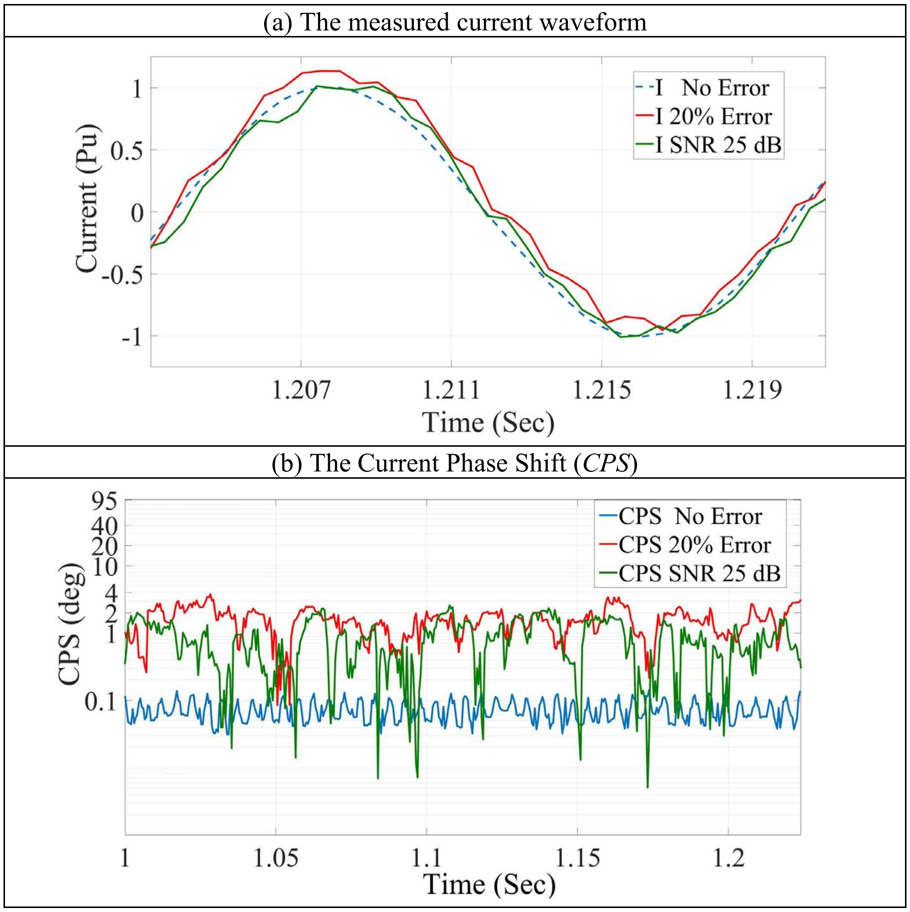

Figure 3-11: a) The measured current waveform for 0, 20%, and SNR = 25 dB measurement error; b) The *CPS* under normal operating mode corresponding to current measurement with 0, 20%, and SNR = 25 dB measurement error

3.5 Comparison of the Performance of the Proposed Directional Element and the Conventional Directional Elements

In this section, the performance of the proposed directional element is compared with the performance of the conventional directional elements discussed in section 3.2 in the system shown in Figure 3-1. As mentioned in section 3.2, MATLAB Simulink is employed to model the system under study. The time step used for performing the simulation is 25 microseconds. A detailed description of the system and the inverter control designs can be found in sections A.2, A.4, and A.5 of the Appendix. The proposed directional element is implemented using MATLAB programing language as shown in Figure 3-12.

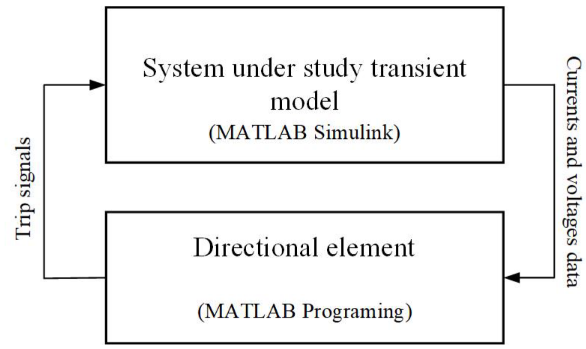

Figure 3-12: Model implementation - Directional element

In the first scenario, a bolted PP fault is applied to the islanded microgrid shown in Figure 3-1 at point F4 at t=4 sec. This is the same scenario discussed in section 3.2.1 for the negative sequence directional element, and as shown by Figure 3-2, the negative sequence directional element of R13 incorrectly detects a forward fault. Figure 3-13 and Figure 3-14 show the measured *CPS* and the proposed directional element output for relay R13 for the first scenario, respectively. As Figure 3-14 depicts, the proposed directional element correctly determines the backward current.

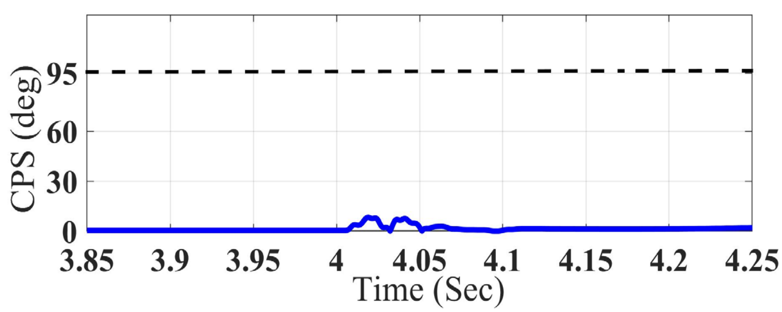

Figure 3-13: *CPS* measured by the proposed directional elements (first scenario R13)

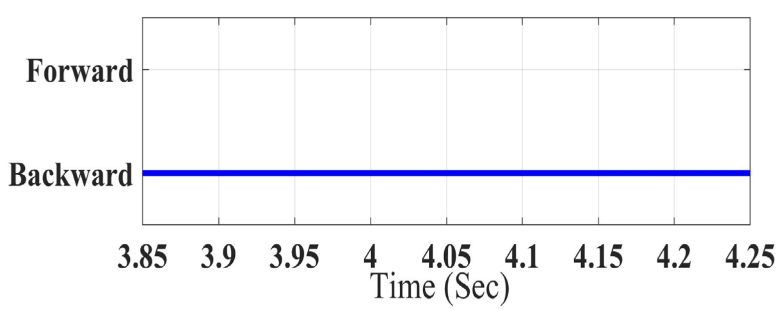

Figure 3-14: The output of the proposed directional element (first scenario R13)

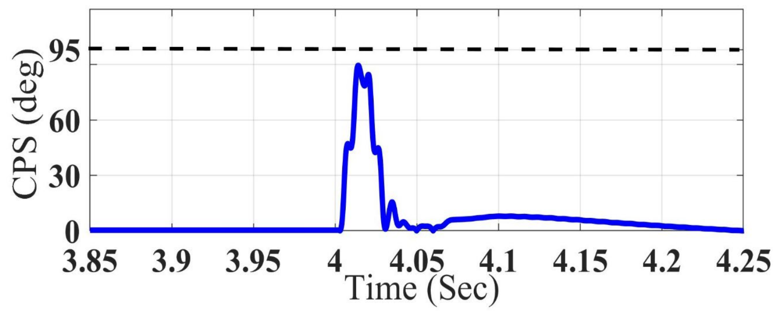

Figure 3-15: *CPS* measured by the proposed directional element (second scenario R1)

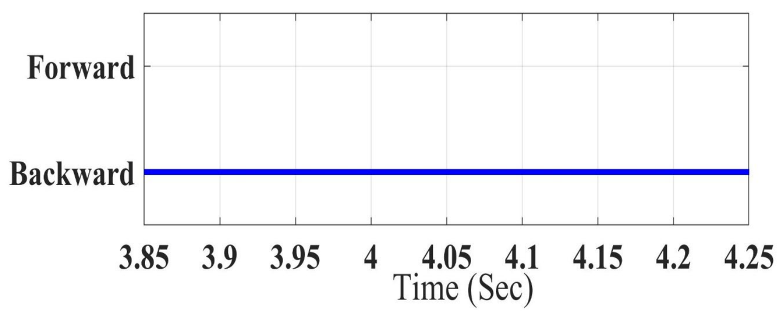

Figure 3-16: The output of the proposed directional element (second scenario R1)

In the second scenario, a bolted 3P fault is applied to the grid-connected microgrid shown in Figure 3-1 at point F4 at t=4 sec. This is the same scenario investigated in section 3.2.2, in which the positive sequence directional element of R1 incorrectly detects a forward fault as shown in Figure 3-3.

Figure 3-15 and Figure 3-16 show the measured *CPS* and the proposed directional element output for relay R1 for the second scenario, respectively. As Figure 3-16 depicts, the proposed directional element correctly determines the backward current.

In the third scenario, a bolted PP fault is applied to the islanded microgrid shown in Figure 3-1 at point F4 at t=4 sec. The fault is reverse for R1, and as shown in section 3.2.3 and Figure 3-4, the phase directional element incorrectly detects a forward fault. Figure 3-17 and Figure 3-18 show the measured *CPS* and the proposed directional element output for relay R1 for the third scenario, respectively. As Figure 3-18 depicts, the proposed directional element correctly determines the backward current.

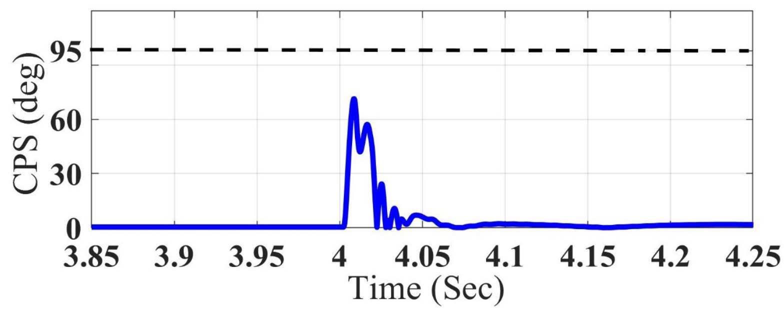

Figure 3-17: *CPS* measured by the proposed directional element (third scenario R1)

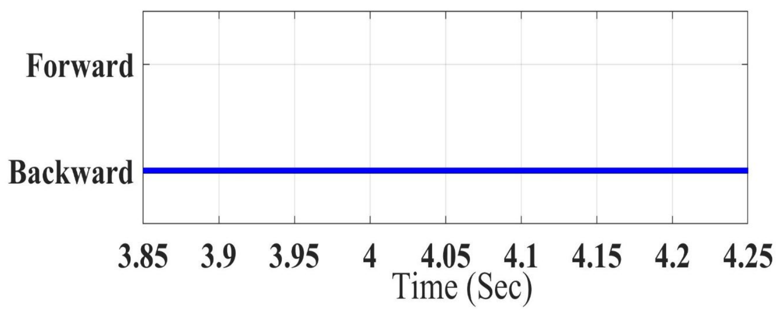

Figure 3-18: The output of the proposed directional element (third scenario R1)

It is worth mentioning that the performance of the proposed directional element will be examined more extensively in chapters 4 and 5.

3.6 Conclusion

This chapter proposed a directional element for microgrids. The proposed element relies on the positive sequence directional element to determine the current direction during normal operation and employs the *CPS* to determine the current direction's changes during fault. The benefits of the proposed directional element are summarized in the following.

- The proposed directional element can determine the current direction under different fault conditions and its performance is not dependent on the presence of the negative sequence current in the system or the phase angle of the voltage and current during fault.
- The proposed element can operate properly when the fault current in the system is limited due to the presence of inverter-based resources in the system where the sources in the system may behave differently compared with the conventional synchronous generators.

Chapter 4: Architecture of the Proposed Protection Scheme

4.1 Introduction

In addition to fault detection and determination of the fault current direction, another important aspect of a protection scheme is its capability to provide backup protection in case of a communication loss or the primary relay's breaker failure. This fact has not been fully considered in the proposed protection schemes for microgrids in the literature. In other words, to date, the research on microgrid protection has not led to a microgrid relay that covers all the aforementioned aspects. Therefore, in this chapter, a protection relay for microgrids is proposed. The relay includes: a) a fault detection element (introduced in Chapter 2), b) a directional element (introduced in Chapter 3), c) a coordination element, and d) a backup protection element.

Also, a protection scheme implemented by the proposed relay is introduced that protects the feeders and distributed generators in the microgrid. The proposed protection scheme can detect all types of faults including impedance faults; it detects the fault in both microgrid operation modes; it can also be implemented using a simple, flexible, and low bandwidth communication system. The proposed scheme does not require a protection relay at every node of the protection zone. In addition, it is able to provide backup protection in case of a communication loss or the primary relay's breaker failure. In this chapter, first, the proposed protection relay and its elements are introduced. Next, the architecture of the proposed protection scheme is explained. Finally, the simulation results are discussed.

4.2 Proposed Protection Relay for Microgrid

The protection relay logic is demonstrated in Figure 4-1. The relay consists of four elements including the fault detection element (introduced in Chapter 2), directional element (introduced in

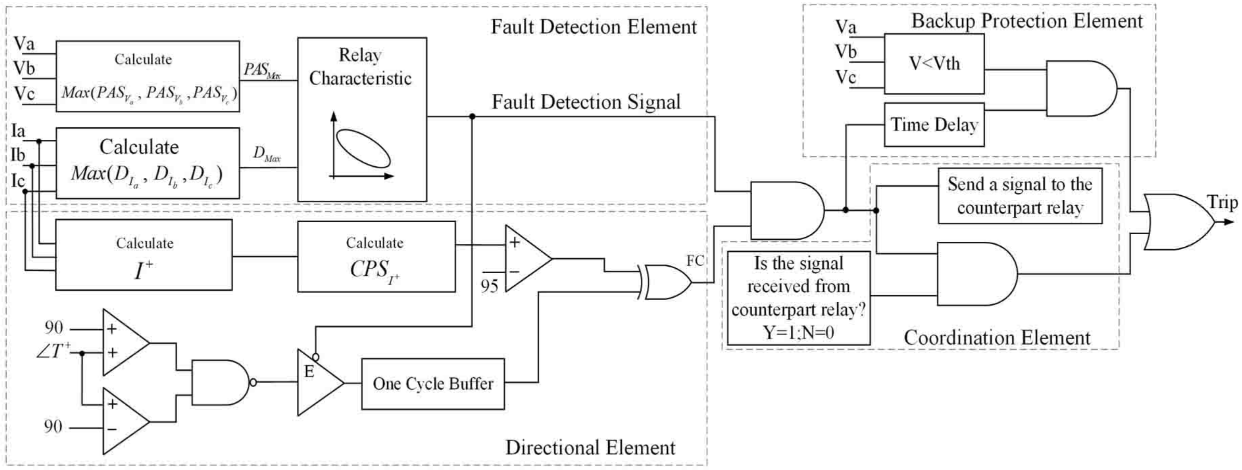

Figure 4-1: Proposed protection relay logic

Chapter 3), coordination element, and backup protection element. The proposed protection relay's coordination element and backup protection element are explained in the following sections.

4.2.1 Coordination Element and Communication Approach

In the proposed relay, the coordination between relays is achieved by using a low-cost communication link that can transfer 2 bits of data between each relay and its counterpart. In the following subsections, the communication approach is explained for systems with bidirectional and unidirectional currents.

4.2.1.1 System with Bidirectional Current

In the proposed protection scheme, each zone is protected with two relays for the system with the bidirectional current. To explain the communication approach in this case, consider the example system shown in Figure 4-2. The system is divided into three protection zones using six circuit breakers. Loads and sources are not shown in Figure 4-2. Assume that fault F occurs in zone 2, the fault detection element of the primary and backup relays in the system, R1, R3, R4, and R6 shown in Figure 4-2 detect the fault. After fault detection, relay R3 checks the current direction and because it sees a forward current, relay R3 sends a signal to relay R4. Relay R4 also detects the fault, and because it sees a forward current, relay R4 sends a signal to relay R3. Then, both relays R3 and R4 trip and clear the fault. In fact, a relay will trip if it detects a forward fault and receives

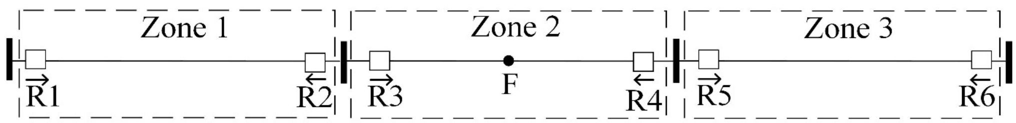

Figure 4-2: Example system with different protection zones (bidirectional current)

a fault signal from its counterpart, which shows the fault is inside the relay zone. If a relay detects a forward fault and does not receive a forward fault signal from its counterpart, this shows the fault is outside the relay zone, and the relay does not trip.

4.2.1.2 System with Unidirectional Current

For a system with unidirectional current, each zone is protected with one relay in the proposed protection scheme as shown in Figure 4-3. In the unidirectional system shown in Figure 4-3, the current flows from left to right. Figure 4-4 demonstrates the protection relay logic for unidirectional systems. In systems with unidirectional current, to determine if the fault is behind the relay, the currents are compared to a threshold value (I_{th}) as shown in Figure 4-4. In unidirectional systems, the relay current is small in case of a fault behind the relay; therefore, I_{th} is a small value (about 20 percent of the nominal current). To explain the communication approach in this case, assume fault F occurs in zone 2. The fault detection element of the relays R1, R2, and R3 in the system detect the fault. For the fault at point F, the currents measured by relay R3 are small ($I_{R3} < I_{th}$) because the system is unidirectional and the fault is behind relay R3; therefore, R3 does not trip and sends a signal to its upstream relay (which is relay R2). The fault detection element of R2 also detects the fault, and since it receives a signal from R3 and $I_{R2} > I_{th}$, the fault is located in relay R2's protection zone. Therefore, R2 trips and clears the fault.

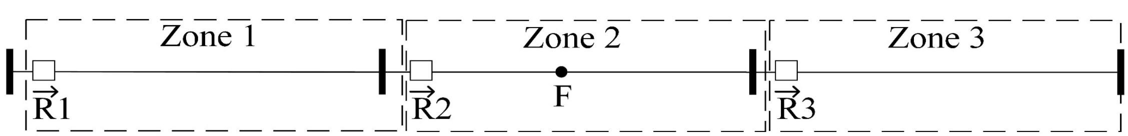

Figure 4-3: Example system with different protection zones (unidirectional current)

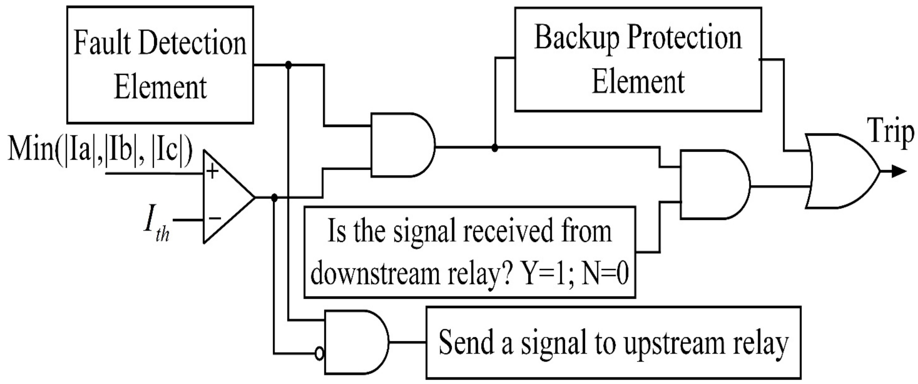

Figure 4-4: Protection relay logic for unidirectional systems

4.2.1.3 Backup Protection Element

As shown in Figure 4-1, the backup protection element will clear the fault after a predetermined time delay if the fault is still not cleared. With a predetermined time-delay after a forward fault is detected, the backup protection element compares the relay voltage with a threshold value (V_{th}) to determine if the fault is still not cleared. V_{th} can be chosen as 95 percent of the nominal voltage. The coordination between relays for backup protection is achieved by using constant time intervals. It is worth mentioning that coordination should be achieved for all the relays in the same direction. To coordinate the relays, the last relay in each direction that does not have a downstream relay is considered as the reference for coordination of each direction. As shown in (4-1), the backup protection operating time of each relay is obtained by adding the Coordination Time Interval (CTI) (in this chapter 0.2 second) to the downstream relay's backup protection operating time that has the same direction. t^b in (4-1) denotes the time delay of the backup protection element shown in Figure 4-1.

For example, in the system shown in Figure 4-2, R5 is the reference relay; therefore, $t_{R5}^b = 0$, and the backup operating time of R3 is $t_{R5}^b + CTI$, and the backup operating time of R1 is $t_{R3}^b + CTI$. For another direction in the system shown in Figure 4-2, R2 is the reference relay; therefore, $t_{R2}^b = 0$, and the backup operating time of R4 is $t_{R2}^b + CTI$, and the backup operating time of R6 is $t_{R4}^b + CTI$.

$$t^b_{R_{n+1}} = t^b_{R_n} + CIT \tag{4-1}$$

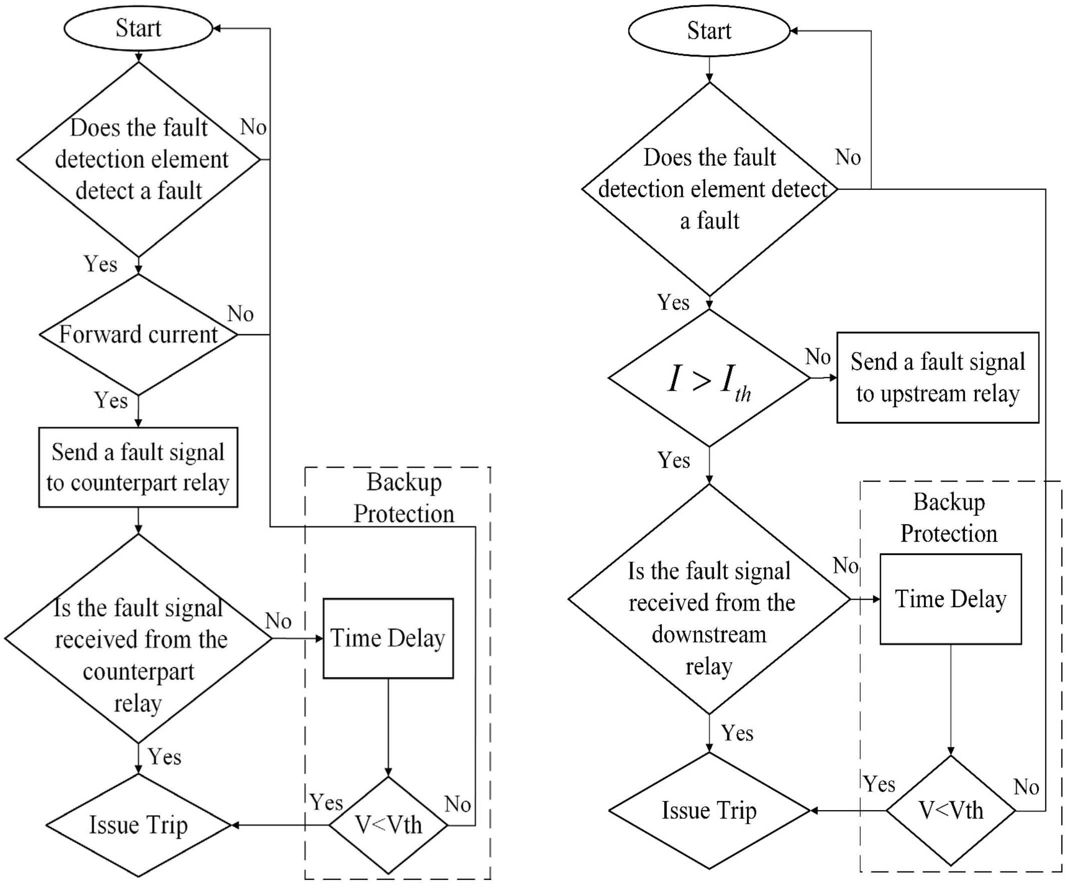

(a) Bidirectional systems (b) Unidirectional systems

Figure 4-5: Protection scheme algorithm

4.3 Proposed Protection Scheme Algorithm

In this section, the proposed protection scheme algorithm is explained for bidirectional and unidirectional systems. Figure 4-5(a) demonstrates the proposed protection algorithm for bidirectional systems. After the fault detection element detects the fault, the directional element checks the direction of the current. In case of a forward fault, the relay sends a fault signal to its counterpart (the relay at the other end of the protection zone). The relay also checks if it receives the fault signal from its counterpart; if the signal is received, it means the fault is in the relay's primary zone, and the relay issues a trip to clear the fault. Also, if the relay does not receive the signal from its counterpart, it either means the communication link is lost or the fault is not in the primary zone of the relay. In either case, the backup protection element will issue a trip to clear the fault if after a predetermined time delay the fault is still not cleared. The proposed protection algorithm for unidirectional systems is shown in Figure 4-5(b). After the fault detection element detects the fault in the system, the relay compares the measured currents with I_{th} to determine if the fault is in front of the relay. In case of a backward fault, the relay sends a signal to its upstream relay. In case of a front fault, the relay checks if it received a signal from its downstream relay to confirm that the fault is in the primary zone of the relay. If the signal is received, the relay will issue the trip and clear the fault. Similar to the algorithm for bidirectional systems, if the relay does not receive the signal from its downstream relay, it either means the communication link is lost or the fault is not in the primary zone of the relay. In either case, the backup protection element will issue a trip to clear the fault if after a predetermined time delay the fault is still not cleared.

As shown in Figure 4-5, in the proposed protection scheme, the fault detection element detects the fault based on the local information, and the scheme is still able to detect and clear the fault in case of a communication failure. Therefore, in addition to a fast fault detection for bolted and impedance faults in both microgrid's operating modes, several advantages are achieved considering the implementation costs: a) in the proposed protection scheme, a signal is sent by relay if the relay detects a forward fault using a low-bandwidth communication link between the two relays; as a result, the implementation cost of the proposed scheme is lower as compared to the protection schemes that requires a high-bandwidth communication such as differential protection; b) in the proposed scheme, the communication link is only for the coordination, and each relay detects the fault based on the local voltage and current measurements and independents of the communication; hence, the scheme is able to provide the backup protection in case of a communication failure; c) in the power system especially in the distribution system, we may have loads connected in the middle of the line (tap load) as shown in Figure 4-6; the proposed scheme can be implemented in the presence of a tap load in the middle of the line; in other words, the proposed protection scheme does not require a relay at every node of the system.

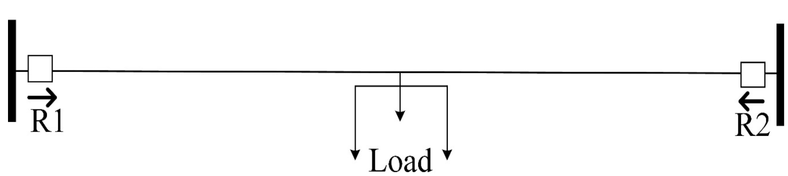

Figure 4-6: An example of a tap load

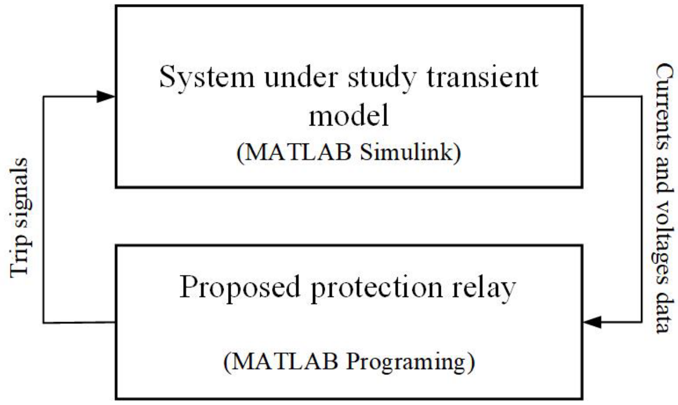

Figure 4-7: Model implementation – Proposed protection relay

4.4 Simulation Results

4.4.1 System Under Study

The system under study is shown in Figure 3-1. The system is described in section 3.2. Table A-2 shows the system parameters. As mentioned in section 3.2, MATLAB Simulink is employed to model the system under study. The time step used for performing the simulation is 25 microseconds. A detailed description of the system and the inverter control designs can be found in sections A.2, A.4, and A.5 of the Appendix. The proposed protection relay is implemented using MATLAB programing language as shown in Figure 4-7.

The sampling frequency for the simulation results is 333 samples per cycle (60×333) kHz= 19.98kHz). The protection relays installed in the system are shown in Figure 3-1. To show the performance of the proposed method in the presence of load in the middle of the line, the line that connects bus B1 to bus B7 is protected with two breakers at each end with load 3 connected in the middle of the line.

4.4.2 Determining Relays' Characteristics

To determine the relays' characteristics based on the procedure explained in section 2.4, the switching scenarios shown in Table 4-1 are simulated in the island and grid-connected modes. The measured *PAS* and *D* parameters for Load, DG, transformer Switching events (LS), Phase to Phase

Table 4-1: Switching scenarios in the island and grid-connected modes

Switching Scenario	Island Mode	Grid-Connected Mode
Load 1= 600kW	×	×
Load 3= 600kW+400kVar	×	×
Load 3= 1MW	×	×
Load 3= 5MW		×
1MVA Transformer	×	×
5MVA Transformer		×
DG 4 Switching	×	×

(PP), Phase to Ground (PG), Phase to Phased to Ground (PPG), and Three Phase (3P) Bolted Faults (BF) and Impedance Faults with $R_f = 40$ ohms (IF) at points F1 for relays R3 and R4 and at point F4 for relays R11 and R12 are compared through Figure 4-8 and Figure 4-9 for the island mode of operation.

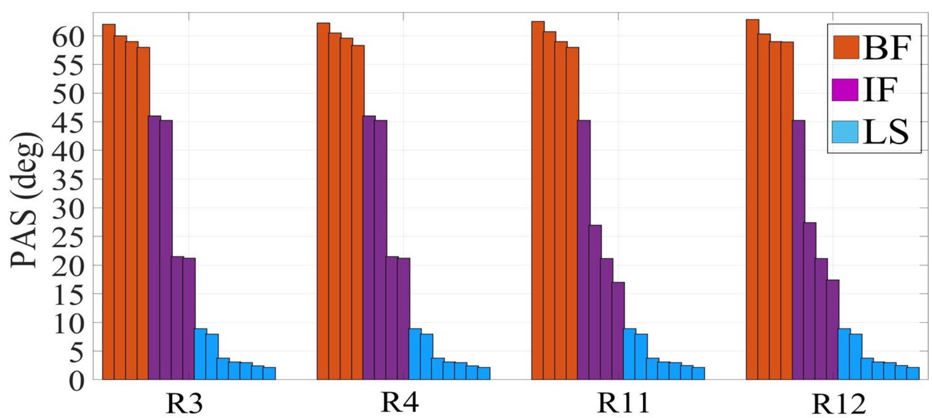

Figure 4-8: Maximum *PAS* parameter measured by relay for fault and switching scenarios in the island mode of operation

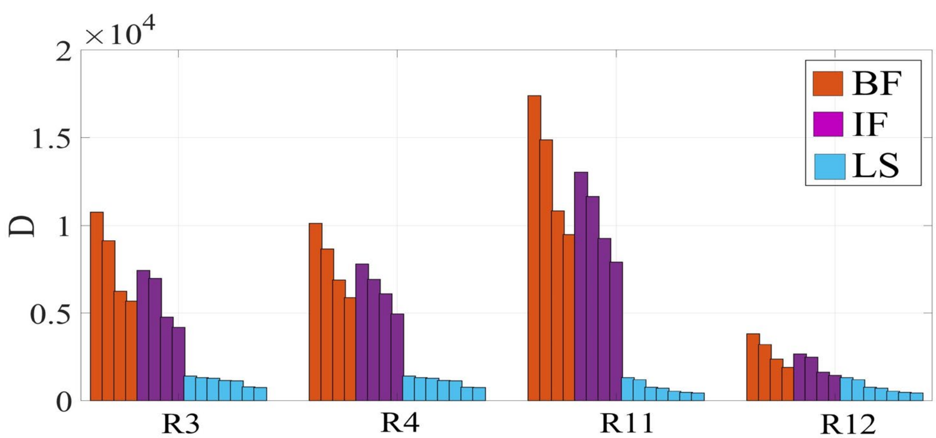

Figure 4-9: Maximum *D* parameter measured by relay for fault and switching scenarios in the island mode of operation

Also, Figure 4-10 and Figure 4-11 compare the measured *PAS* and *D* parameters for LS events and PP, PG, PPG, 3P bolted fault, and IF with $R_f = 40$ ohms at points F1 for relays R3 and R4 and at point F4 for relays R11 and R12 in the grid-connected mode. In Figure 4-8 and Figure 4-10, the blue bars show the *PAS* measured for different load, DG, and transformer switching; the purple bars demonstrate the *PAS* measured for PP, PG, PPG, 3P impedance faults, and the orange bars depict the *PAS* measured for PP, PG, PPG, 3P bolted faults. As Figure 4-8 shows, the maximum *PAS* measured among switching events is 8.85 degrees, and the minimum *PAS* measured among fault scenarios is 17 degrees in the island mode. In the grid-connected mode, as shown in Figure 4-10, the maximum *PAS* measured among switching events is 1.4 degrees, and the minimum *PAS* measured among fault scenarios is 7.5 degrees. As mentioned in section 2.3.1, *PAS* is affected by the variation in the X/R ratio between the source and the faulted feeder, the active and reactive

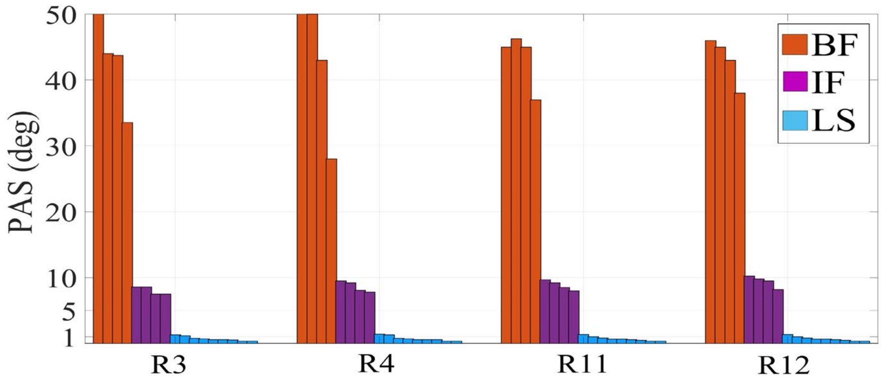

Figure 4-10: Maximum *PAS* parameter measured by relay for fault and switching scenarios in the grid-connected mode of operation

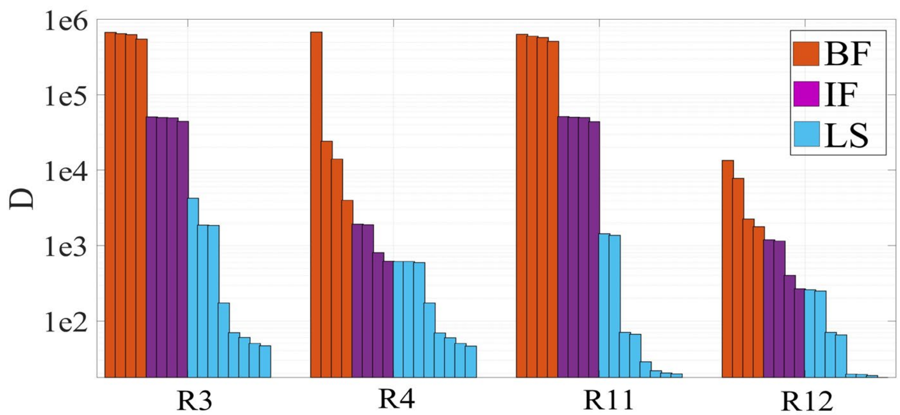

Figure 4-11: Maximum *D* parameter measured by relay for fault and switching scenarios in the grid-connected mode of operation

power variation following a fault and their effects on frequency and voltage levels, and also the transformation of the sag to lower voltage levels as a result of a fault. Therefore, as shown in Figure 4-8 and Figure 4-10, PAS variation is larger following a fault as compared to a switching event, and it is possible to differentiate between fault condition and switching event by measuring PAS parameter in both modes of microgrid operation. D parameter measured for switching events and fault scenarios is also compared by Figure 4-9 and Figure 4-11 in the island and grid-connected modes, respectively. In Figure 4-9 and Figure 4-11, the blue bars show D parameter measured for different load, DG, and transformer switching; the purple bars depict D measured for PP, PG, PPG, 3P impedance faults, and the orange bars demonstrate D measured for PP, PG, PPG, 3P bolted faults. Because of the presence of inverter-based resources and their limited fault current, D parameter measured for some fault scenarios is very close to the measured D value for switching scenarios. Therefore, D parameter cannot be separately used to differentiate between fault conditions and switching events. However, it can be used as an indication of the fault in the system especially when there is a combination of rotating and static resources in the microgrid.

4.4.3 Island Mode: Bolted and Impedance Faults

In this section, the performance of the protection scheme implemented by the proposed protection relay is evaluated by applying PG, PP, PPG, and 3P faults to the islanded microgrid at points F1, F2, F3, and F4 shown in Figure 3-1. The faults include bolted faults and impedance faults with $R_f = 40$ ohms. The relays' fault detection characteristics parameters obtained based on the fault detection scheme discussed in section 2.4 are shown in Table 4-2 for the island mode.

Table 4-3 demonstrates the primary and backup relays' operating time for different fault scenarios in the island mode. As Table 4-3 shows, the fault detection time of all the primary relays for the performed fault scenarios are less than one AC cycle (16 milliseconds), and all backup relays operate in a coordinated manner with respect to the primary relays. As an example, the primary relay R3 clears a 3P bolted fault at point F1 in the island mode in 0.0058 seconds. In case that the primary relay R3 does not clear the fault for example because of a breaker failure, the backup relays R1 and R15 clear the fault after 0.6113 and 0.8098 seconds respectively as depicted by Table 4-3. Figure 4-12 shows the relay characteristic, (D, PAS) trajectory, the measured CPS, and

Table 4-2: Relays' fault detection characteristics parameters – Island mode

Relay	Semi major axis	Semi minor axis	Eigenvector 1	Eigenvector 2	D mean	PAS mean
R1	3723.77	9.67	(-1, 0)	(0, -1)	1333.12	3.43
R2	3718.76	9.64	(-1, 0)	(0, -1)	1331.58	3.43
R3	3095.74	10.46	(-1, 0)	(0, -1)	1434.51	3.45
R4	3100.95	10.48	(-1, 0)	(0, -1)	1436.07	3.46
R5	1892.83	8.98	(-1, 0)	(0, -1)	1023.81	3.46
R6	1894.37	8.98	(-1, 0)	(0, -1)	1024.11	3.47
R7	2130.36	8.17	(-1, 0)	(0, -1)	913.52	3.06
R8	1674.51	9.19	(-1, 0)	(0, -1)	819.17	2.95
R9	3723.77	9.67	(-1, 0)	(0, -1)	1333.12	3.43
R10	1406.65	9.86	(-1, 0)	(0, -1)	769.17	3.65
R11	3702.8	9.49	(-1, 0)	(0, -1)	927.14	3.58
R12	3704.07	9.49	(-1, 0)	(0, -1)	927.3	3.59
R13	4372.06	10	(-1, 0)	(0, -1)	950.34	3.49
R14	4373.13	9.98	(-1, 0)	(0, -1)	949.61	3.49
R15	2062.08	8.62	(-1, 0)	(0, -1)	1315.33	3.48
R16	404.9	9.73	(-1, -0.01)	(0.01, -1)	214.36	3.66

Table 4-3: Primary and backup relays' operating time in the island mode

			Bolted Faults (Sec)				Impedance Faults (Sec)			
			3P	PG	PP	PPG	3P	PG	PP	PPG
F1	Primary	R3	.0058	.0046	.0048	.0053	.0072	.0057	.0055	.0063
		R4	.0051	.0048	.0049	.0050	.0054	.0052	.0056	.0052
	Backup	R6	1.006	1.005	1.004	1.005	1.006	1.005	1.505	1.505
		R15	.8098	.8054	.8047	.8063	.8114	.8082	.8053	.8091
		R1	.6113	.6069	.6048	.6082	.6120	.6112	.6055	.6102
F2	Primary	R7	.0066	.0052	.0048	.0058	.0123	.0069	.0053	.0073
		R8	.0051	.0046	.0047	.0050	.0057	.0051	.0053	.0053
	Ba	R5	.2056	.2046	.2049	.2053	.2068	.2055	.2056	.2062
F3	Primary	R9	.0043	.0042	.0042	.0044	.0049	.0048	.0048	.0049
		R10	.0091	.0048	.0048	.0059	.0114	.0057	.0055	.0066
	Backup	R2	.6043	.6042	.6042	.6044	.6049	.6048	.6048	.6049
		R12	1.011	1.007	1.004	1.010	1.012	1.011	1.005	1.010
		R16	1.011	1.005	1.004	1.006	1.012	1.005	1.005	1.006
F4	Primary	R11	.0039	.0038	.0038	.0039	.0043	.0042	.0042	.0044
		R12	.0114	.0071	.0048	.0108	.0121	.0115	.0055	.0107
	Backup	R9	.4044	.4043	.4042	.4044	.4048	.4049	.4048	.4049
		R16	1.011	1.004	1.004	1.006	1.012	1.005	1.005	1.006
		R14	1.211	1.207	1.204	1.211	1.212	1.212	1.205	1.211

the directional element output for relays R11 and R12 when an impedance PG fault with $R_f = 40$ ohms is applied to the system at t= 4 seconds at point F4. As Figure 4-12 shows, R12 sees a forward current before the fault (before t=4 sec); *CPS* for R12 is small when the fault occurs as demonstrated in Figure 4-12, which means the current direction is the same as the direction before the fault for R12, and R12 correctly detects the forward fault. For relay R11, *CPS* is about 140 degrees and is more than *CPS* threshold value (95 degrees), which means the current direction is

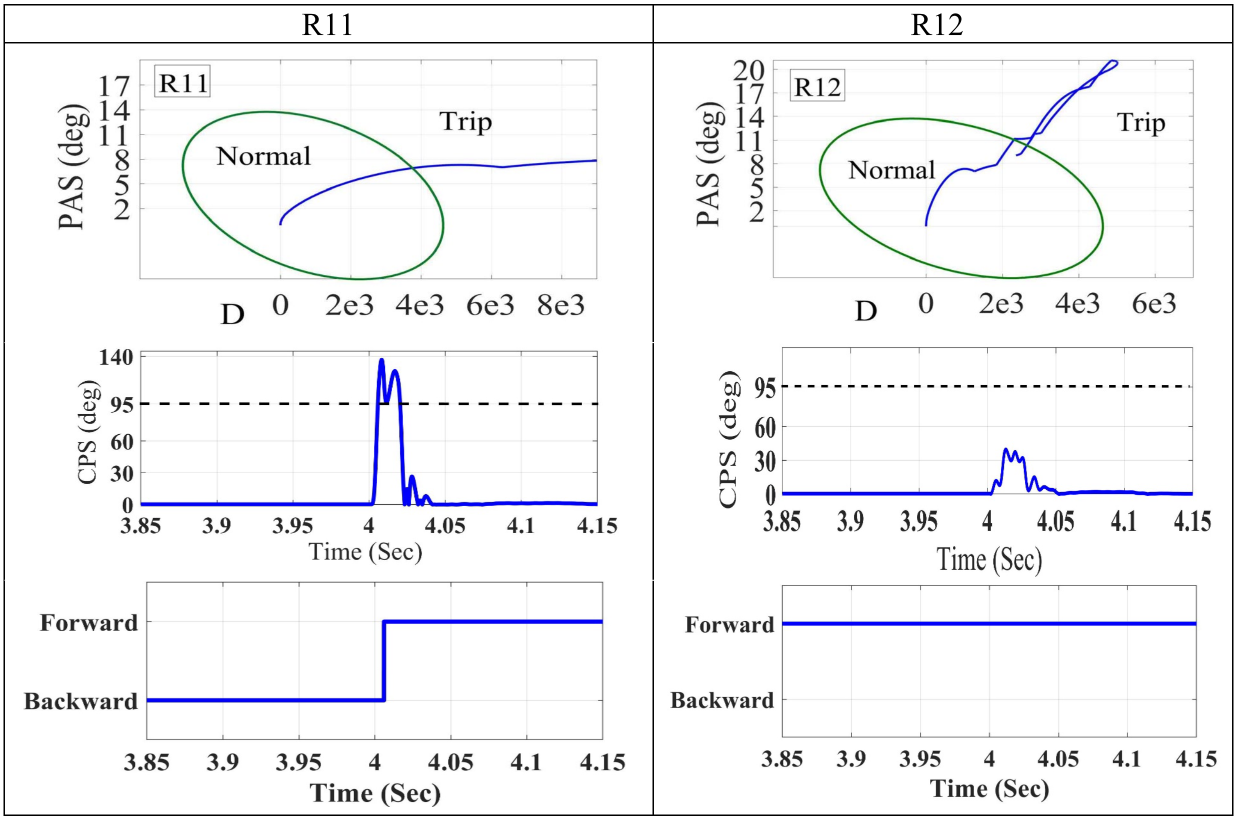

Figure 4-12: Relays R11 and R12 characteristics and (D, *PAS*) trajectories; *CPS* measurement and the output of the directional elements for Impedance PG fault ($R_f = 40$)

reversed because of the fault at t= 4 sec. As Figure 4-12 shows, relay R11 sees a backward current before the fault, and the current direction is reversed after the fault, which shows R11 correctly detects the forward fault.

4.4.4 Grid-connected Mode: Bolted and Impedance Faults

In the grid-connected mode, the microgrid is connected to a 700 MVA, 120 kV grid feeder. To examine the performance of the protection scheme and the proposed relay in the grid-connected mode, PG, PP, PPG, and 3P faults are applied to the grid-connected microgrid at points F1, F2, F3, and F4 shown in Figure 3-1. The faults include bolted faults and impedance faults with $R_f =$ 40 ohms. The relays' fault detection characteristics parameters obtained based on the fault detection scheme discussed in section 2.4 are shown in Table 4-4 for the grid-connected mode. Table 4-5 depicts the primary and backup relays' operating times for different fault scenarios in the grid-connected mode. As Table 4-5 shows, the fault detection time of all the primary relays for the performed fault scenarios are less than one AC cycle (16 milliseconds), and all the backup relays operate in a coordinated manner with respect to the primary relays. As an example, the primary relay R4 clears a 3P bolted fault at point F1 in the grid-connected mode in 0.0022 seconds as demonstrated by Table 4-5.

Table 4-4: Relays' fault detection characteristics parameters – Grid mode

Relay	Semi major axis	Semi minor axis	Eigenvector 1	Eigenvector 2	D mean	PAS mean
R1	30345.46	1.17	(-1, 0)	(0, -1)	3852.86	0.63
R2	30335.3	1.17	(-1, 0)	(0, -1)	3871.17	0.65
R3	30721	1.17	(-1, 0)	(0, -1)	3898.59	0.65
R4	30648.71	1.19	(-1, 0)	(0, -1)	3969.61	0.67
R5	30719.37	1.15	(-1, 0)	(0, -1)	3365.64	0.62
R6	30723.6	1.17	(-1, 0)	(0, -1)	3365.78	0.64
R7	30290.82	1.21	(-1, 0)	(0, -1)	3330.01	0.62
R8	30295.28	1.23	(-1, 0)	(0, -1)	3330.56	0.63
R9	21199.33	0.87	(-1, 0)	(0, -1)	3363.42	0.6
R10	1830.74	1.34	(-1, 0)	(0, -1)	329.8	0.6
R11	3734.06	1.26	(-1, 0)	(0, -1)	548.89	0.62
R12	3739.88	1.26	(-1, 0)	(0, -1)	547.86	0.62
R13	4582.28	1.38	(-1, 0)	(0, -1)	651.15	0.58
R14	4589.83	1.39	(-1, 0)	(0, -1)	652.16	0.58
R15	446.65	1.28	(-1, 0)	(0, -1)	64.36	0.6
R16	286.26	1.31	(-1, 0)	(0, -1)	55.54	0.57
R17	31171.54	0.8	(-1, 0)	(0, -1)	6722.22	0.6

Table 4-5: Primary and backup relays' operating time in the grid-connected mode

			Bolted Faults (Sec)				Impedance Faults (Sec)			
			3P	PG	PP	PPG	3P	PG	PP	PPG
F1	Primary	R3	.0022	.0028	.0021	.0023	.0040	.0040	.0027	.0041
		R4	.0022	.0027	.0020	.0021	.0036	.0035	.0025	.0037
	Backup	R6	1.002	1.002	1.002	1.002	1.003	1.003	1.002	1.003
		R15	.8023	.8028	.8021	.8023	.8041	.8041	.8028	.8040
		R1	.6023	.6028	.6021	.6024	.6042	.6046	.6029	.6041
F2	Primary	R7	.0022	.0027	.0021	.0022	.0037	.0035	.0025	.0040
		R8	.0022	.0027	.0021	.0022	.0035	.0033	.0024	.0038
	Ba	R5	.2023	.2028	.2021	.2023	.2038	.2037	.2026	.2039
F3	Primary	R9	.0021	.0026	.0020	.0021	.0036	.0037	.0023	.0034
		R10	.0023	.0028	.0021	.0023	.0043	.0043	.0030	.0042
	Backup	R2	.6022	.6028	.6021	.6022	.6039	.6041	.6028	.6038
		R12	1.002	1.002	1.002	1.002	1.004	1.004	1.002	1.004
		R16	1.002	1.002	1.002	1.002	1.004	1.004	1.002	1.004
		R17	.8023	.8029	.8024	.8023	.8037	.8045	.8032	.8043
F4	Primary	R11	.0021	.0027	.0021	.0021	.0024	.0032	.0024	.0024
		R12	.0022	.0027	.0021	.0022	.0038	.0036	.0027	.0040
	Backup	R9	.4022	.4027	.4020	.4023	.4036	.4039	.4024	.4035
		R16	1.002	1.002	1.002	1.002	1.003	1.003	1.002	1.004
		R14	1.202	1.202	1.202	1.202	1.203	1.203	1.202	1.204

Table 4-6: Primary and backup relays' operating time in the presence of SG

			Bolted Faults (SG)				Impedance Faults (SG)			
			3P	PG	PP	PPG	3P	PG	PP	PPG
F1	Primary	R3	.0059	.0048	.0084	.0023	.0073	.0073	.0090	.0051
		R4	.0071	.0077	.0089	.0052	.0074	.0086	.0101	.0063
	Backup	R6	1.009	1.008	1.010	1.002	1.009	1.009	1.014	1.006
		R15	.8074	.8087	.8051	.8023	.8081	.8097	.8095	.8076
		R1	.6115	.6109	.6094	.6064	.6135	.6153	.6141	.6121
F4	Primary	R11	.0042	.0038	.0071	.0036	.0050	.0043	.0075	.0041
		R12	.0121	.0117	.0097	.0085	.0137	.0162	.0143	.0136
	Backup	R9	.4045	.041	.4074	.4039	.4062	.4050	.4078	.4046
		R16	1.012	1.005	1.008	1.003	1.014	1.007	1.013	1.003
		R14	1.213	1.212	1.210	1.212	1.214	1.217	1.214	1.215

4.4.5 Performance of the Proposed Scheme in the Presence of a Synchronous Generator

In this section, BES (DG1) is replaced with a 1 MVA Synchronous Generator (SG) to examine the performance of the proposed scheme in the presence of SG in the microgrid. In this case, the voltage and frequency of the microgrid are formed by SG in the island mode and DG2 to DG 4 are working in PQ mode. PG, PP, PPG, and 3P faults are applied to the islanded microgrid at points F1 and F4. The faults include bolted faults and impedance faults with $R_f = 40$ ohms. The primary and backup relays' operating times for different fault scenarios for this case are shown in Table 4-6. All the primary relays detect the fault rapidly for the performed fault scenarios, and all the backup relays operate in a coordinated manner with respect to the primary relays as demonstrated by Table 4-6. As an example, the primary relay R11 clears a 3P bolted fault at point F4 in the island mode in 0.0042 seconds as shown by Table 4-6. The results confirm the high performance of the proposed scheme in the presence of the SG in the microgrid.

4.4.6 Performance of the Proposed Scheme Against Impedance Fault with Higher Impedance

To evaluate the performance of the proposed method against the impedance faults with fault impedance greater than 40 ohms, PG, PP, PPG, and 3P impedance faults with 120 ohms fault impedance are applied to the islanded microgrid and the fault detection time of the relays are

Table 4-7:Primary and backup relays' operating time for impedance fault with $R_f = 120$ ohms- Island mode

			IF 120 ohms (BES- Case 4.4.3)				IF 120 ohms (SG-Case 4.4.5)			
			3P	PG	PP	PPG	3P	PG	PP	PPG
F1	Primary	R3	.0110	.0079	.0102	.0086	.0082	.0095	.0101	.0075
		R4	.0062	.0061	.0099	.0060	.0118	.0103	.0149	.0117
	Backup	R6	1.007	1.006	1.010	1.006	1.015	1.012	1.016	1.013
		R15	.8135	.8126	.8101	.8113	.8093	.8113	.8109	.8097
		R1	.6140	.6167	.6104	.6115	.6150	.6170	.6153	.6148
F4	Primary	R11	.0053	.0051	.0054	.0052	.0068	.0075	.0083	.0064
		R12	.0125	.0120	.0105	.0117	.0157	.0184	.0155	.0153
	Backup	R9	.4064	.4062	.4062	.4061	.4073	.4085	.4087	.4074
		R16	1.009	1.010	1.010	1.012	1.018	1.008	1.014	1.044
		R14	1.202	1.202	1.202	1.202	1.218	1.221	1.216	1.215

obtained. The primary and backup relays' operating time for different types of impedance faults with $R_f = 120$ ohms at points F1 and F4 for case 4.4.3 and case 4.4.5 are shown in Table 4-7. As depicted by Table 4-7, all the primary relays detect the fault for the performed fault scenarios in this case, and all the backup relays operate in a coordinated manner with respect to the primary relays. As an example, the primary relay R3 clears a 3P impedance fault with $R_f = 120$ ohms at point F1 in the island mode in 0.011 seconds for case 4.4.3; also, R3 clears a 3P impedance fault with $R_f = 120$ ohms at point F1 in the island mode in 0.0082 seconds for case 4.4.5 as shown by Table 4-7; this confirms the high performance of the proposed scheme against the impedance fault with 120 ohms fault impedance.

4.4.7 The Effect of Changing the α Parameter on the Performance of the Proposed Protection Scheme

As explained in section 2.3.1.1, α is the number of samples between the present and past sampling windows when calculating PAS parameter. As mentioned, α parameter can be chosen between $0.1K$ to K, where K is the total number of samples in one cycle. In this section, the measured PAS for different switching and fault scenarios in the island and grid-connected modes are compared for $\alpha = 0.1K$ and $\alpha = K$ in the system under study shown in Figure 3-1.

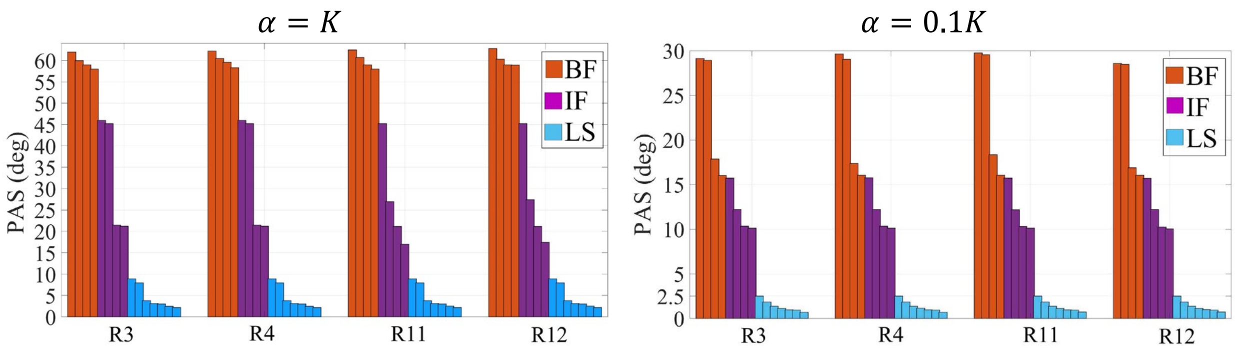

Figure 4-13: Comparison of PAS measured for different scenarios for $\alpha = 0.1K$ and $\alpha = K$ in the island mode

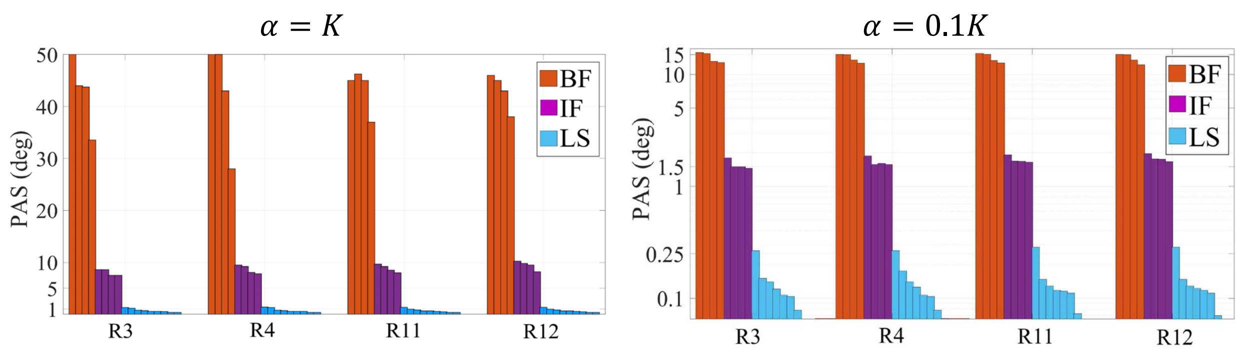

Figure 4-14: Comparison of PAS measured for different scenarios for $\alpha = 0.1K$ and $\alpha = K$ in the grid-connected mode

The switching scenarios are shown in Table 4-1, and the fault scenarios include PP, PG, PPG, 3P bolted fault and IF with $R_f = 40$ ohms at points F1 and F4. In Figure 4-13 and Figure 4-14, the blue bars show the PAS measured for different load, DG, and transformer switching; the purple bars demonstrate the PAS measured for PP, PG, PPG, 3P impedance faults, and the orange bars depict the PAS measured for PP, PG, PPG, 3P bolted faults. Figure 4-13 and Figure 4-14 compare the PAS measured for different scenarios for $\alpha = 0.1K$ and $\alpha = K$ in the island and grid-connected modes, respectively.

Table 4-8 and Table 4-9 compares the primary and backup relays' operating time for $\alpha = 0.1K$ and $\alpha = K$ in the island and grid-connected modes for bolted faults, respectively.

As Figure 4-13 and Figure 4-14 demonstrate, PAS measured for different scenarios increases by increasing α parameter. As an example, PAS measured for 3P bolted fault in the island mode is 29 degrees with $\alpha = 0.1K$, and it is 62 degrees with $\alpha = K$. α is the number of samples between the present and past sampling windows when calculating the PAS parameter as explained in section 2.3.1.1. By selecting $\alpha = K$ the difference between the present and past sampling windows is one

AC cycle. Therefore, the filter can capture a larger phase angle shift as compared to when the difference between the present and past sampling windows is 0.1 AC cycle ($\alpha = 0.1K$). As a result, increasing α parameter can eliminate the need for high-accuracy measurement and high sampling frequency by measuring a larger *PAS* following a fault and increasing the margin between the measured *PAS* value for fault condition and switching event. However, the relay fault detection time in the island and grid-connected mode will slightly increase by increasing α as Table 4-8 and Table 4-9 demonstrate. For example, the fault detection time of the primary relay R3 for a 3P fault at point F1 in the island mode of operation increases from 0.0025 seconds (for $\alpha = 0.1K$) to 0.0058 seconds (for $\alpha = K$) as shown in Table 4-8.

Table 4-8: Comparison of the primary and backup relays' operating time for $\alpha = 0.1K$ and $\alpha = K$ in the island mode

			$\alpha = K$				$\alpha = 0.1K$			
			3P	PG	PP	PPG	3P	PG	PP	PPG
F1	Primary	R3	.0058	.0046	.0048	.0053	.0025	.0025	.0022	.0024
		R4	.0051	.0048	.0049	.0050	.0025	.0025	.0022	.0024
	Backup	R6	1.0064	1.0055	1.0047	1.0057	1 .0026	1.0026	1.0023	1.0025
		R15	.8098	.8054	.8047	.8063	.8025	.8025	.8023	.8025
		R1	.6113	.6069	.6048	.6082	.6025	.026	.6023	.6025
F4	Primary	R11	.0039	.0038	.0038	.0039	.0026	.0026	.0023	.0026
		R12	.0114	.0071	.0048	.0108	.0026	.0026	.0023	.0026
	Backup	R9	.4044	.4043	.4042	.4044	.4026	.4026	.4023	.4026
		R16	1.0116	1.0049	1.0047	1.0060	1.0026	1.0026	1.0023	1.0026
		R14	1.0117	1.0071	1.0049	1.0114	1.0026	1.0026	1.0023	1.0026

Table 4-9: Comparison of the primary and backup relays' operating time for $\alpha = 0.1K$ and $\alpha = K$ in the grid-connected mode

			$\alpha = K$				$\alpha = 0.1K$			
			3P	PG	PP	PPG	3P	PG	PP	PPG
F1	Primary	R3	.0022	.0028	.0021	.0023	.0019	.0023	.0018	.0019
		R4	.0022	.0027	.0020	.0021	.0019	.0024	.0019	.0019
	Backup	R6	1.0022	1.0027	1.0021	1.0022	1.0021	1.0026	1.0020	1.0021
		R15	.8023	.8028	.8021	.8023	.8019	.8024	.8019	.8019
		R1	.6023	.6028	.6021	.6024	.6019	.6023	.6018	.6019
F4	Primary	R11	.0021	.0027	.0021	.0021	.0019	.0023	.0018	.0019
		R12	.0022	.0027	.0021	.0022	.0019	.0023	.0018	.0019
	Backup	R9	.4022	.4027	.4020	.4023	.4019	.4025	.4019	.4020
		R16	1.0022	1.0028	1.0021	1.0023	1.0019	1.0023	1.0018	1.0019
		R14	1.0023	1.0028	1.0021	1.0023	1.0019	1.0023	1.0018	1.0019

4.4.8 The Impact of the Presence of the Harmonics on the Performance of the Proposed Scheme

In this section, the effect of the harmonics on the performance of the proposed scheme is investigated in the double feeder microgrid (shown in Figure 3-1). This is achieved by adding 20% of the 3rd and 15% of the 5th harmonic components to the voltage and current signals [134], [135]. As an illustration, Figure 4-15(a) demonstrates the voltage waveform containing 20% of the 3rd and 15% of the 5th harmonic components. Figure 4-15(b) shows the measured *PAS* corresponding to the voltage waveform. Figure 4-16 demonstrates relay R3 characteristic for the island mode of operation and the (*D*, *PAS*) trajectory when the voltages and current signals are contaminated with the harmonic components. As shown by Figure 4-15(b) and Figure 4-16, the proposed method is able to remove 3rd and 5th harmonic components from the waveform and calculate *PAS* and *D* values with negligible error in the presence of 3rd and 5th harmonic components in the system.

(a) The voltage waveform

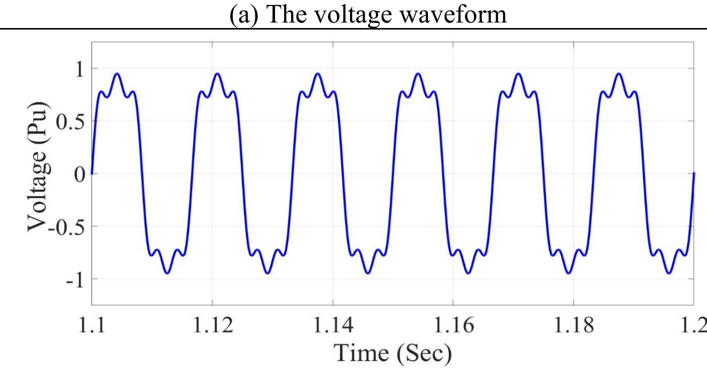

(b) The voltage Phase Angle Shift (*PAS*)

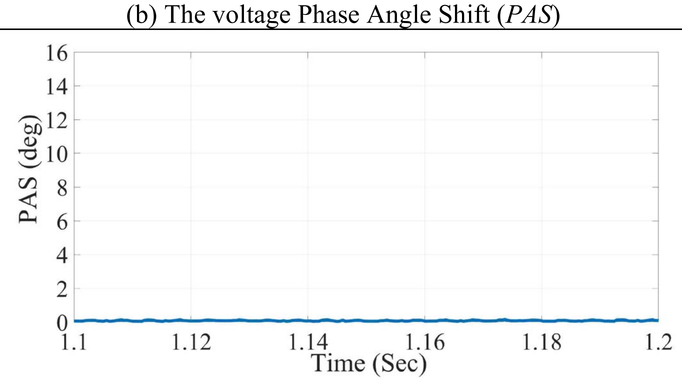

Figure 4-15: a) The voltage waveform containing 20% of 3rd and 15% of 5th harmonic components; b) The voltage Phase Angle Shift (*PAS*) corresponding to the voltage waveform

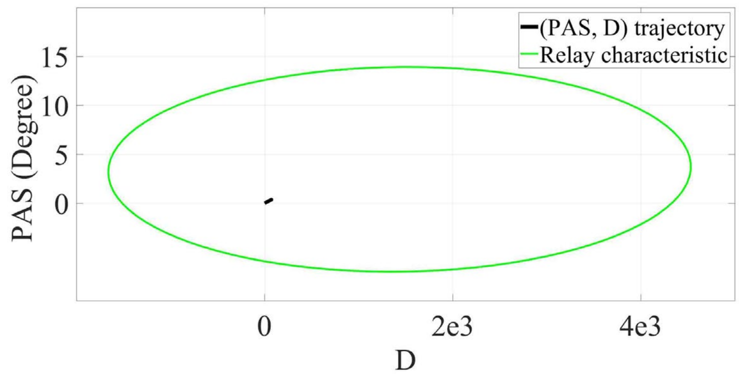

Figure 4-16: Relay R3 characteristic for the island mode of operation, and the (*D*, *PAS*) trajectory when the voltage and current signals are contaminated with the harmonic components

4.5 Conclusion

A protection relay for microgrids was proposed in this chapter by employing the fault detection element, the directional element, and by developing a coordination element and a backup protection element. In addition, a protection scheme implemented by the proposed relay was introduced. The main benefits of the proposed protection scheme are mentioned in the following.

- The proposed protection scheme can detect all types of faults including impedance faults.
- The proposed scheme is able to detect the fault in both microgrid operating modes including island and grid-connected modes.
- The scheme is able to provide backup protection in case of the primary relay's breaker failure or communication loss.
- The proposed scheme does not need a relay at every node of the system and can be implemented by a low-cost communication link that can transfer 2 bits of data between each relay and its counterpart.

Chapter 5 : Real-time Controller-Hardware-in-the-Loop Validation and Experimental Results

5.1 Introduction

In this chapter, the performance of the proposed protection scheme is evaluated in the Real-Time Controller-Hardware in the Loop (C-HIL) setup, and its performance is compared with the conventional protection schemes. In the next section, the C-HIL setup and its components are explained. Also, the implementation of the proposed scheme in the C-HIL setup is briefly discussed. Next, the performance of the proposed scheme is evaluated for three different systems by performing several scenarios in the C-HIL setup. The scheme is also compared with directional overcurrent protection (ANSI standard number: 67 [136]) and voltage-restrained overcurrent protection (ANSI standard number: 51V [136]). Finally, the proposed scheme is tested by the measurements obtained on a physical distribution test line and the results are discussed.

5.2 Controller-Hardware-in-the-Loop (C-HIL) Setup

The C-HIL setup is shown in Figure 5-1. The C-HIL setup includes an OPAL-RT real-time simulator, amplifiers, two SEL 651 R2 protection relays, an FPGA-based National Instrument Compact Rio controller, and two SEL 3031 radio transceivers as shown in Figure 5-1. Table 5-1 shows the part list for the C-HIL implementation. Figure 5-2 shows the actual setup. The proposed directional element and fault detection element shown in Figure 4-1 are implemented on the FPGA-based controller. To validate the program, the proposed relay is reprogrammed by LabView software to be implemented in the FPGA-based controller for the C-HIL results, and the MATLAB

Table 5-1: C-HIL setup part list

Part	Number	Model
Real-time simulator	1	OPAL-RT OP 5650
Current amplifier	6	AE Techron 7224
Voltage amplifier	6	AE Techron 7212
Protection relay	2	SEL 651 R2
Serial radio transceiver	2	SEL 3031
Controller	1	National Instrument cRIO 9040

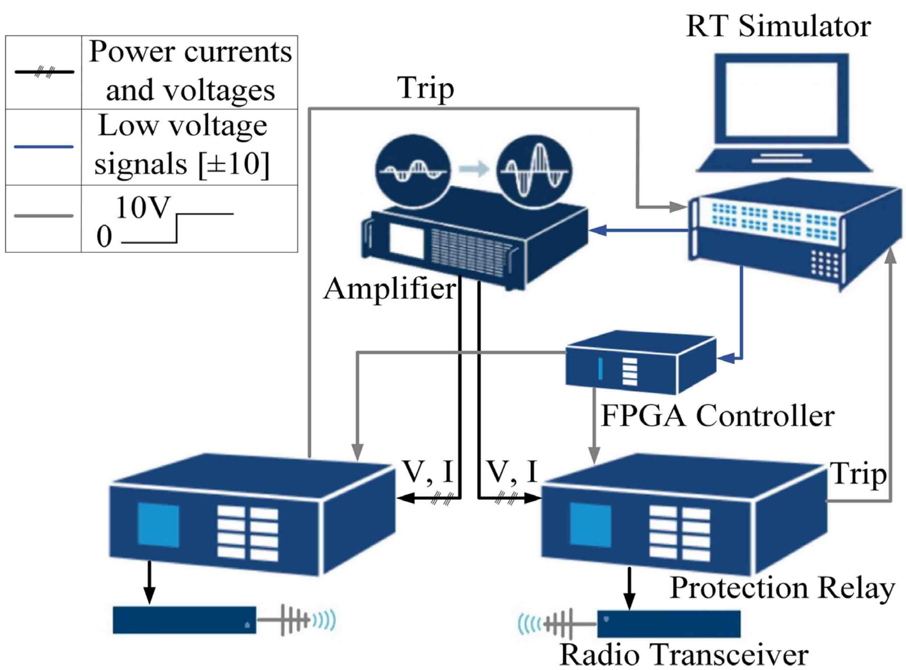

Figure 5-1: the Controller-Hardware-in-the-Loop(C-HIL) setup

code that is used for the simulation results has not been employed here. There is a link between the FPGA-based controller and the protection relays as shown in Figure 5-1. The protection relay used in the experiment is SEL-651R2 which is one of the relays that is commonly used in the distribution system. By employing the controller, the proposed directional element and fault detection element can be added to the protection functions on the protection relay. In this setup, two protection relays are employed that demonstrate the relay at each end of the protection zone. Since each protection zone has a maximum of two relays as demonstrated in Figure 4-2, any system configuration can be mapped using the C-HIL setup shown in Figure 5-1. In fact, the protection zone under investigation is mapped by the C-HIL setup, and the rest of the system is modeled in

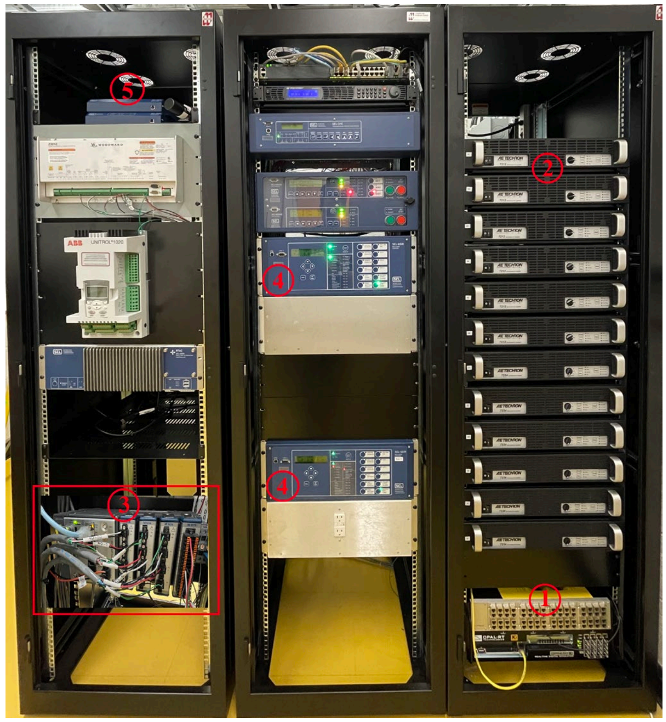

Figure 5-2: C-HIL setup, 1) RT simulator. 2) Amplifiers, 3) Controller (installed on the back of the rack), 4) Protection relays 5) Radio transceivers

real time in the Hypersim software. For example, to investigate the performance of the proposed relay in case of a fault at point F4 shown in Figure 3-1, one of the relays in the C-HIL setup is represented as R11 and the other one as R12 in the system under study shown in Figure 3-1. The C-HIL schematic is shown in Figure 5-3. The coordination element shown in Figure 4-1 is implemented using serial radio transceivers. The controller is sampling the voltage and current signals received from the real-time simulator at 33 samples per cycle (1.98 kHz). The function of each part is briefly explained in the following subsections.

5.2.1 Real-Time Simulator

The real-time simulator OPAL-RT OP 5650 is employed to simulate the system under study in real-time. The simulator is equipped with analog and digital I/O cards that are able to inject the selected signals into the amplifier and the FPGA-based controller connected to the simulator.

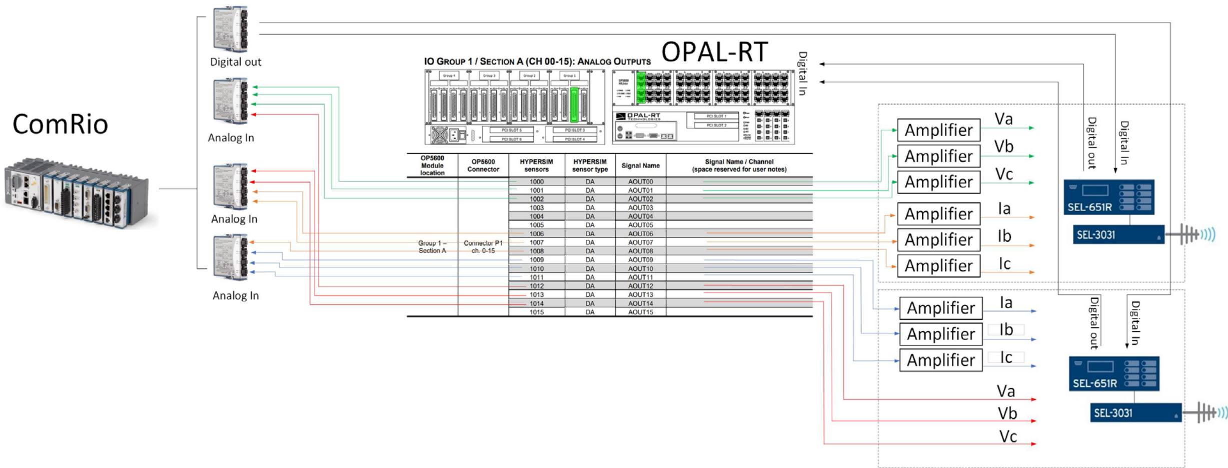

Figure 5-3: C-HIL schematic

5.2.2 Amplifiers

AE Techron 7224 and AE Techron 7212 amplifiers are used here to convert the analog signal coming from the real-time simulator to high-power voltage and current signals that are connected to the input of the protection relays. Since there are two protection relays in the setup, 6 voltage amplifiers and 6 current amplifiers are employed in the C-HIL setup.

5.2.3 Protection Relays

The protection relay employed for the protection studies in the C-HIL setup is SEL 651 R2 which is one of the most common protection relays used in the distribution system.

5.2.4 Serial Radio Transceiver

The serial radio transceiver is SEL 3031 which is a 915 MHz ISM serial data radio that supports point-to-point (P2P) and point-to-multipoint (P2MP) operational modes. The serial radio transceiver is employed in the C-HIL setup to communicate the fault detection signal between the two protection relays.

5.2.5 FPGA-based Controller

The FPGA-based controller is National Instrument cRIO 9040 which includes a processor running in real-time, a programmable FPGA, and modular I/O. It is used in the C-HIL setup to implement the protection algorisms by programming the FPGA and the real-time controller.

5.3 Evaluation of the Proposed Scheme in C-HIL Setup

In this section, the performance of the proposed scheme is evaluated for three systems. A low-voltage distribution feeder, the modified CIGRE benchmark system [100], and the double feeder microgrid [106]. It should be mentioned that all three systems are modeled in real-time software to run the models in real-time for the C-HIL validation.

5.3.1 Low-voltage Distribution Feeder

This system is a 600V distribution feeder that can work in the island and grid-connected modes. The feeder includes a 320kW diesel generator, 300kW battery energy storage, 250kW PV, 100kW curtailable load, and 300kW critical load. In the grid-connected mode, the system is connected to a 25kV, 100MVA main grid. The system is demonstrated in Figure 5-4.

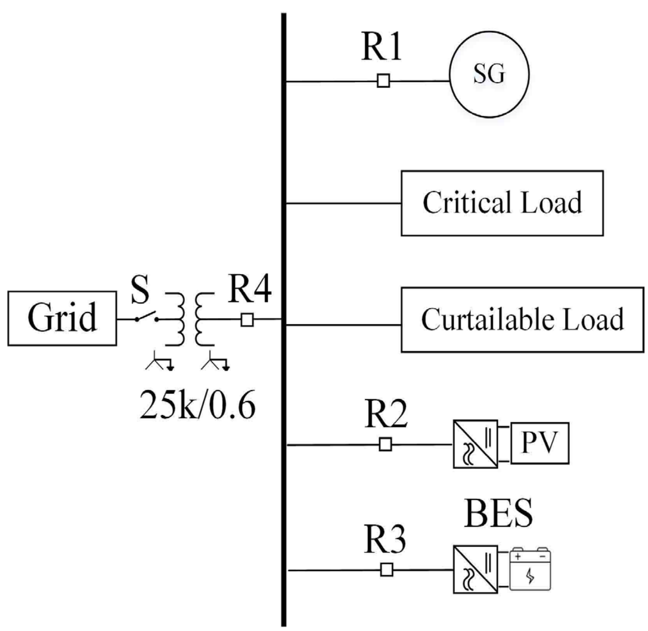

Figure 5-4: Low voltage distribution feeder

The system parameters are shown in Table A-1 in the Appendix section. A detailed description of the system and the inverter control designs can be found in sections A.1, A.4, and A.5 of the Appendix. The effectiveness of the proposed method in this system is investigated in the island and grid-connected modes in the following subsections.

5.3.1.1 Island Mode

In the island mode of operation, several switching scenarios are performed, and *PAS* and *D* parameters for each scenario are obtained. The switching scenarios performed in this system are shown in Table 5-2. Then, the relays' characteristics are obtained based on the procedure explained in section 2.4 and section 2.5.4. The relays' fault detection characteristics parameters obtained based on the fault detection scheme discussed in section 2.4 are shown in Table 5-3 for the island

Table 5-2: Switching scenarios

Load =100kW
Load=300kW
Load=500kW
PV switching

Table 5-3: Relays' fault detection characteristics parameters – Island mode

Relay	Semi major axis	Semi minor axis	Eigenvector 1	Eigenvector 2	D mean	PAS mean
R1	15060.72	9.12	(-1, 0)	(0, -1)	5938.2	5.27
R2	20322.41	8.81	(-1, 0)	(0, -1)	3626.4	5.27
R3	8319.53	11.16	(-1, 0)	(0, -1)	3544.8	5.27

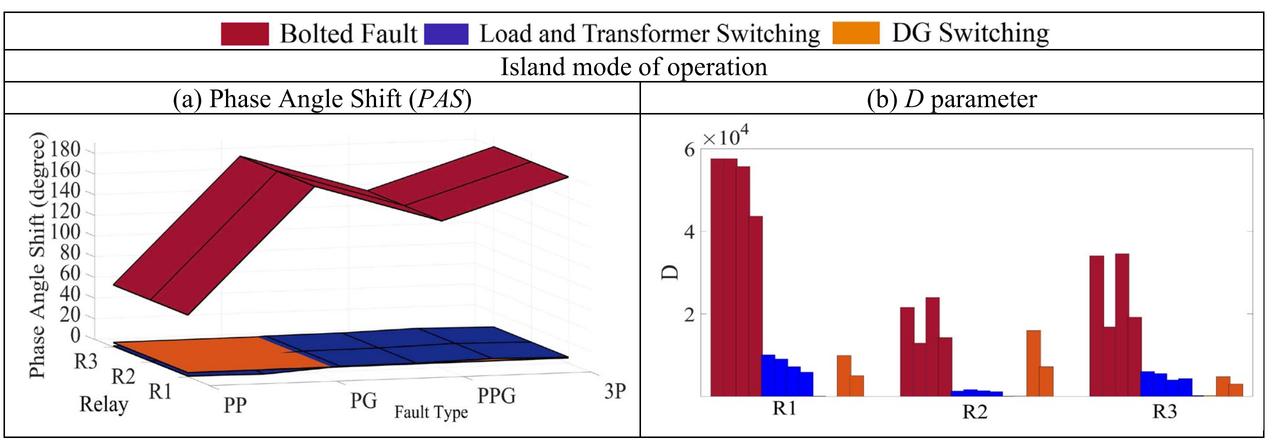

Figure 5-5: Maximum voltage *PAS* and *D* parameter measured by relays for the switching and fault scenarios- Island mode

Table 5-4: Maximum voltage PAS and D parameter measured by relays for the switching and fault scenarios- Island mode

	Parameter	Load Switching				Bolted Fault on the Busbar (PP, PG, PPG, 3P)			
R1	PAS	1	5.25	7	4.23	60	180	142	180
	D	7200	9139.2	10080	9979.2	43680	57600	55680	57600
R2	PAS	1	5.25	7	4.23	60	180	142	180
	D	1416	1680	1344	15955.2	14256	21600	23971.2	12931.2
R3	PAS	1	5.25	7	4.23	60	180	142	180
	D	4032	5568	6096	4800	19200	34080	34560	16800

Table 5-5: Fault clearing time of the relays in the island mode

	Bolted Faults			
	3P	PG	PP	PPG
R1	0.0157	0.01595	0.0117	0.0158
R2	0.0157	0.01595	0.0117	0.0158
R3	0.0157	0.01595	0.0117	0.0158

mode. The fault scenarios including bolted PG, PPG, PP, and 3P faults on the feeder are performed. Table 5-4 and Figure 5-5 show *PAS* and *D* parameters obtained by the relays in the C-HIL setup for the performed fault and switching scenarios. As demonstrated in Figure 5-5, *PAS* parameter measured for fault conditions is significantly larger as compared to *PAS* parameter measured for switching events. As an illustration, the minimum *PAS* measured by R1 among fault scenarios is 60 degrees, and the maximum *PAS* measured by R1 among switching scenarios is 7 degrees in the island mode of operation as Figure 5-5 demonstrates. Table 5-5 shows the fault clearing time of the relays in the island mode As Table 5-5 demonstrates, all fault types are cleared by the relays rapidly in the island mode based on the fault detection scheme discussed in section 2.4 and by employing the proposed relay shown in Figure 4-1. For example, all the relays R1, R2, and R3 clear a three-phase fault on the feeder in 0.0157 seconds after the fault in the island mode as depicted by Table 5-5.

5.3.1.2 Grid-connected Mode

In the grid-connected mode, the system is connected to a 25kV, 100MVA main grid. The same switching and fault scenarios as the island mode are performed in the grid-connected mode, and the relays' characteristics are obtained based on the procedure explained in section 2.4 and section 2.5.4. The relays' fault detection characteristics parameters obtained based on the fault detection scheme discussed in section 2.4 are shown in Table 5-6 for the grid-connected mode.

Table 5-7 and Figure 5-6 demonstrate *PAS* and *D* parameters obtained for the performed scenarios in the grid-connected mode in the C-HIL setup. The *PAS* value following a fault is higher than the

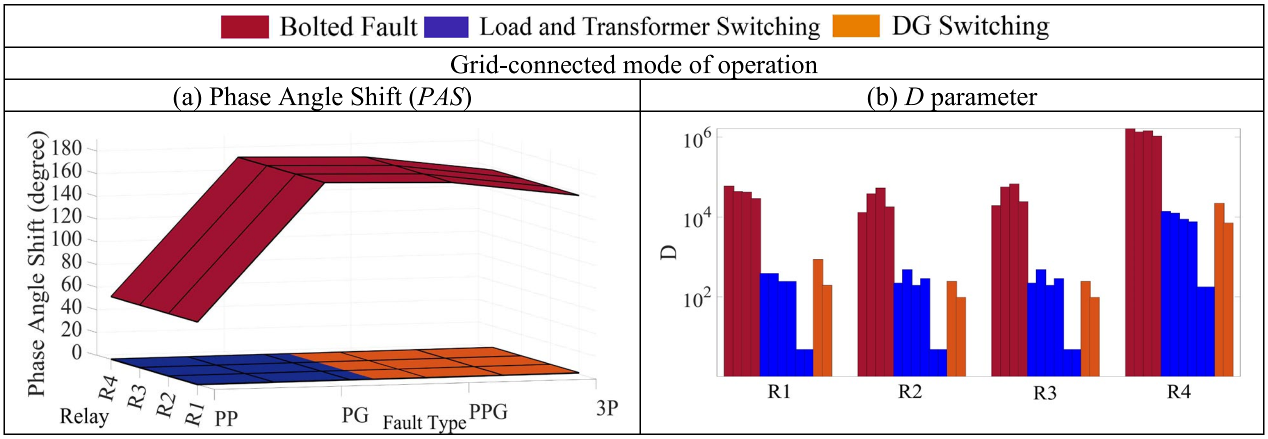

Figure 5-6: Maximum voltage *PAS* and *D* parameter measured by relays for the switching and fault scenarios- Grid-connected mode

Table 5-6: Relays' fault detection characteristics parameters – Grid mode

Relay	Semi major axis	Semi minor axis	Eigenvector 1	Eigenvector 2	D mean	PAS mean
R1	924.62	0.78	(-1, 0)	(0, -1)	312	0.63
R2	485.06	0.96	(-1, 0)	(0, -1)	213.6	0.63
R3	485.06	0.96	(-1, 0)	(0, -1)	213.6	0.63
R4	26849.07	0.76	(-1, 0)	(0, -1)	8998	0.63

Table 5-7: Maximum voltage PAS and D parameter measured by relays for the switching and fault scenarios- Grid mode

	Parameter	Load Switching				Bolted Fault on the Busbar (PP, PG, PPG, 3P)			
R1	PAS	0.01	0.5	0.8	0.4	55.29	175	172	157.4
	D	4.8	240	384	864	28800	43200	41760	59040
R2	PAS	0.01	0.6	1	0.2	55.29	175	172	157.4
	D	4.8	288	480	240	17760	38400	52800	12960
R3	PAS	0.01	0.6	1	0.2	55.29	175	172	157.4
	D	4.8	288	480	240	24000	56160	67200	19200
R4	PAS	0.02	0.86	1.42	0.8	120	153	163	186
	D	176	7568	12496	22000	1056000	1346400	1434400	1636800

Table 5-8: Fault clearing time of the relays in the grid-connected mode

	Bolted Faults			
	3P	PG	PP	PPG
R1	0.04785	0.0452	0.04665	0.04795
R2	0.04785	0.0452	0.04665	0.04795
R3	0.04785	0.0452	0.04665	0.04795
R4	0.04035	0.04255	0.04345	0.04195

PAS value following a switching event as shown in Figure 5-6, verifying that it is possible to differentiate between the fault and switching scenarios by employing *PAS* parameter based on the fault detection scheme discussed in section 2.4 and by using the proposed relay shown in Figure 4-1. As an example, the minimum *PAS* measured by relay R3 is 55 degrees among fault scenarios, and the maximum *PAS* measured by relay R3 among switching scenarios is 1.5 degrees in the grid-connected mode as shown in Figure 5-6. The fault clearing time of the relays for the performed fault scenarios is depicted in Table 5-8. All faults are cleared in less than 4.5 AC cycle in the grid-connected mode as Table 5-8 demonstrates. For example, all the relays R1, R2, R3, and R4 clear a three-phase fault on the feeder in 0.04785 seconds after the fault in the grid-connected mode.

5.3.2 The Modified CIGRE Benchmark System

The modified CIGRE benchmark system [100] includes battery energy storage and three type 4 wind turbines as shown in Figure 2-7. The system parameters are shown in Table A-3 in the Appendix section. More information about the modified CIGRE benchmark system can be found in section 2.5. In the following subsections, the performance of the proposed method for this system is investigated in the island and grid-connected modes.

5.3.2.1 Island Mode

In the island mode of operation, the switching scenarios shown in Table 2-2 are performed, and *PAS* and *D* parameters for each scenario are obtained in the C-HIL setup. Then, the relays' characteristics are obtained based on the procedure explained in section 2.4 and section 2.5.4. The relays' fault detection characteristics parameters obtained based on the fault detection scheme discussed in section 2.4 are shown in Table 5-9 for the island mode.

Several fault scenarios including bolted and impedance ($R_f = 40$) PG, PPG, PP, and 3P faults at point F3 are performed to verify the results obtained by MATLAB Simulink software presented in section 2.5.1. Table 5-10 and Figure 5-7 show *PAS* and *D* parameters obtained by the relays in the C-HIL setup for the performed fault and switching scenarios. As shown in Figure 5-7, *PAS*

Table 5-9: Relays' fault detection characteristics parameters – Island mode

Relay	Semi major axis	Semi minor axis	Eigenvector 1	Eigenvector 2	D mean	PAS mean
R3	331.94	12.1	(-1, 0.02)	(-0.02, -1)	170.98	7.28
R5	136.15	9.46	(-0.99, -0.12)	(0.12, -0.99)	57.62	8.28
R6	150.44	9.7	(-1, -0.08)	(0.08, -1)	61.54	7.02
R9	422.72	14.65	(-1, 0.03)	(-0.03, -1)	95.12	8.28
R10	79.74	8.29	(-0.99, -0.16)	(0.16, -0.99)	35.03	7.02

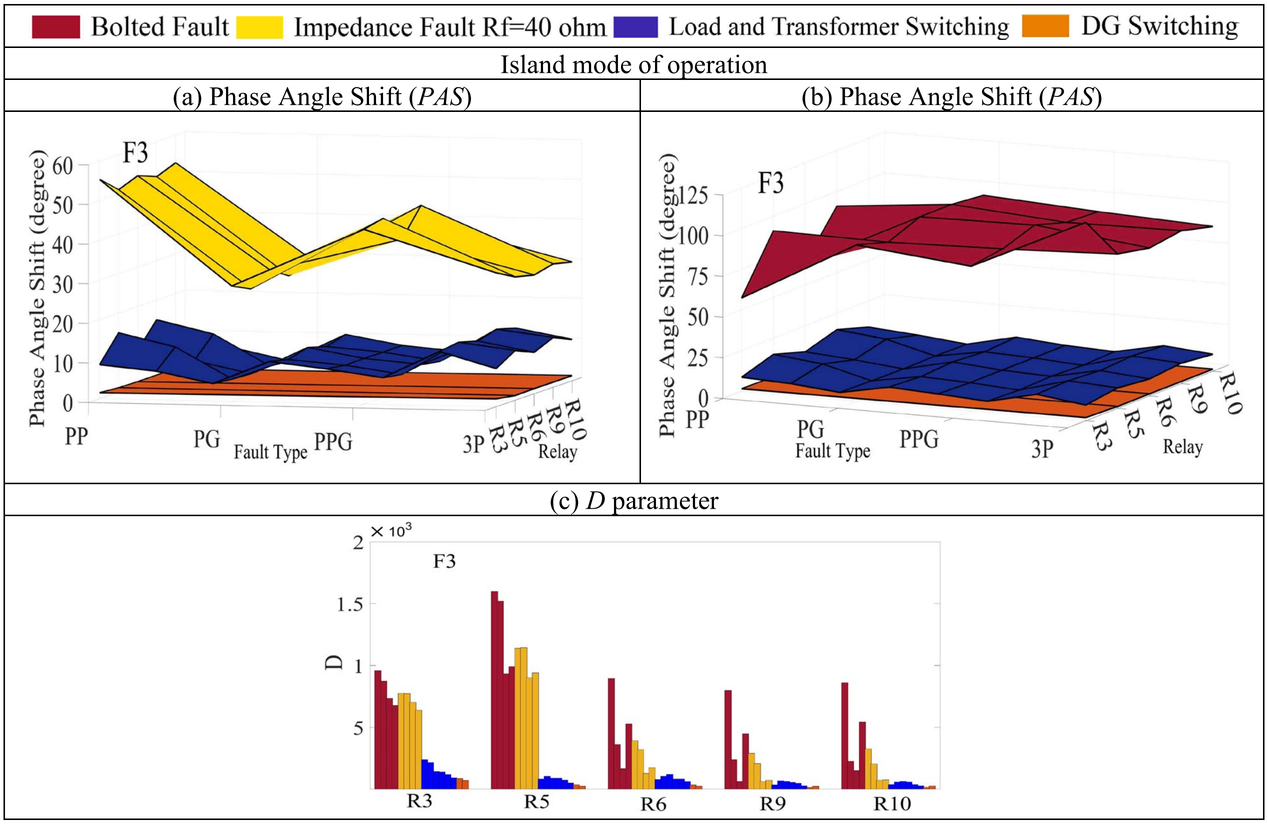

Figure 5-7: Maximum voltage *PAS* and *D* parameter measured by relays for the switching and fault scenarios - Island mode

Table 5-10: Maximum voltage PAS and D parameter measured by relays for the switching and fault scenarios- Island mode

	Parameter	Load Switching					Impedance Fault $R_f = 40$ (PP, PG, PPG, 3P)			
R3	PAS	7.26	10.28	6.77	9.64	1.5	55.37	29.15	44.12	33.83
	D	217.6	144.64	93.12	119.68	348.8	702.72	773.12	775.36	640.96
R5	PAS	11.7	9.09	5.97	12.57	1.1	51.12	26.82	45.21	31.16
	D	105.92	90.24	51.84	75.2	3.52	900.8	1145.6	1139.84	941.76
R6	PAS	6.6	10.5	6.8	10.452	1	53	29.92	38.37	30
	D	106.88	121.6	63.36	83.2	3.52	128	320	393.6	176

following a fault is higher as compared to the *PAS* following a switching event. For example, the minimum *PAS* measured by relay R6 among fault scenarios is 30 degrees, and the maximum *PAS* measured by relay R6 is 13 degrees among switching scenarios in the island mode as demonstrated by Figure 5-7. Table 5-11 shows the fault clearing time of the relays in the island mode based on the fault detection scheme discussed in section 2.4 and by employing the proposed relay shown in Figure 4-1. As an illustration, the primary relays R5 and R6 clear a bolted three-phase fault at point F3 in 0.0654 and 0.0555 seconds after the fault respectively in the island mode. Also, in case that the primary relays do not clear the fault at point F3 for any reason such as breaker failure, the backup relays R3, R9, and R10 clear the bolted three-phase fault at point F3 in 0.2160, 0.4165,

Table 5-11: Fault clearing time of the relays in the island mode

			Bolted Fault				Impedance Fault $R_f = 40$			
			3P	PG	PP	PPG	3P	PG	PP	PPG
F3	Pr	R5	0.0654	0.057	0.0552	0.0626	0.0579	0.0611	0.05425	0.0590
		R6	0.0555	0.0669	0.0527	0.0539	0.0562	0.0534	0.05745	0.0571
	Ba	R3	0.2160	0.21555	0.2143	0.2162	0.2163	0.21595	0.2135	0.2155
		R9	0.4165	0.43175	0.4160	0.4159	0.4194	0.42055	0.4184	0.4206
		R10	0.6262	0.61435	0.6128	0.6244	0.6160	0.61795	0.6154	0.6181

, and 0.6262 seconds respectively as shown in Table 5-11.

5.3.2.2 Grid-connected Mode

The microgrid is connected to a 120kV main grid bus bar with 500 MVA short circuit capacity in the grid-connected mode. The switching scenarios shown in Table 2-2 are performed and the *PAS* and *D* parameters for each scenario are obtained in the C-HIL setup. Then, the relays' characteristics are obtained based on the procedure explained in section 2.4 and section 2.5.4. The relays' fault detection characteristics parameters obtained based on the fault detection scheme discussed in section 2.4 are shown in Table 5-12 for the grid-connected mode.

Fault scenarios including PG, PPG, PP, and 3P bolted and impedance ($R_f = 40$ ohms) faults at point F3 are performed in the grid-connected mode.

Table 5-13 and Figure 5-8 show *PAS* and *D* parameters obtained by the relays in the C-HIL setup for the performed fault and switching scenarios. The *PAS* value measured for a fault is higher than the *PAS* value measured for a switching event, which shows *PAS* parameter can be used to differentiate between the fault and switching scenarios based on the fault detection scheme discussed in section 2.4 and by employing the proposed relay shown in Figure 4-1. As an example, among the fault scenarios, the minimum *PAS* measured by R3 is 6 degrees, and the maximum *PAS* measured by R3 among switching scenarios is 2.6 degrees in the grid-connected mode as depicted in Figure 5-8. Table 5-14 shows the fault clearing time of the relays in the grid-connected mode.

Table 5-12: Relays' fault detection characteristics parameters – Grid mode

Relay	Semi major axis	Semi minor axis	Eigenvector 1	Eigenvector 2	D mean	PAS mean
R3	903.27	3.44	(-1, 0)	(0, -1)	200.96	0.81
R5	140.9	2.76	(-1, -0.01)	(0.01, -1)	49.17	0.78
R6	74.23	3.02	(-1, -0.03)	(0.03, -1)	20.98	0.89
R9	479.53	3.3	(-1, 0)	(0, -1)	79.73	0.78
R10	72.62	3.79	(-1, -0.01)	(0.01, -1)	20.53	0.89

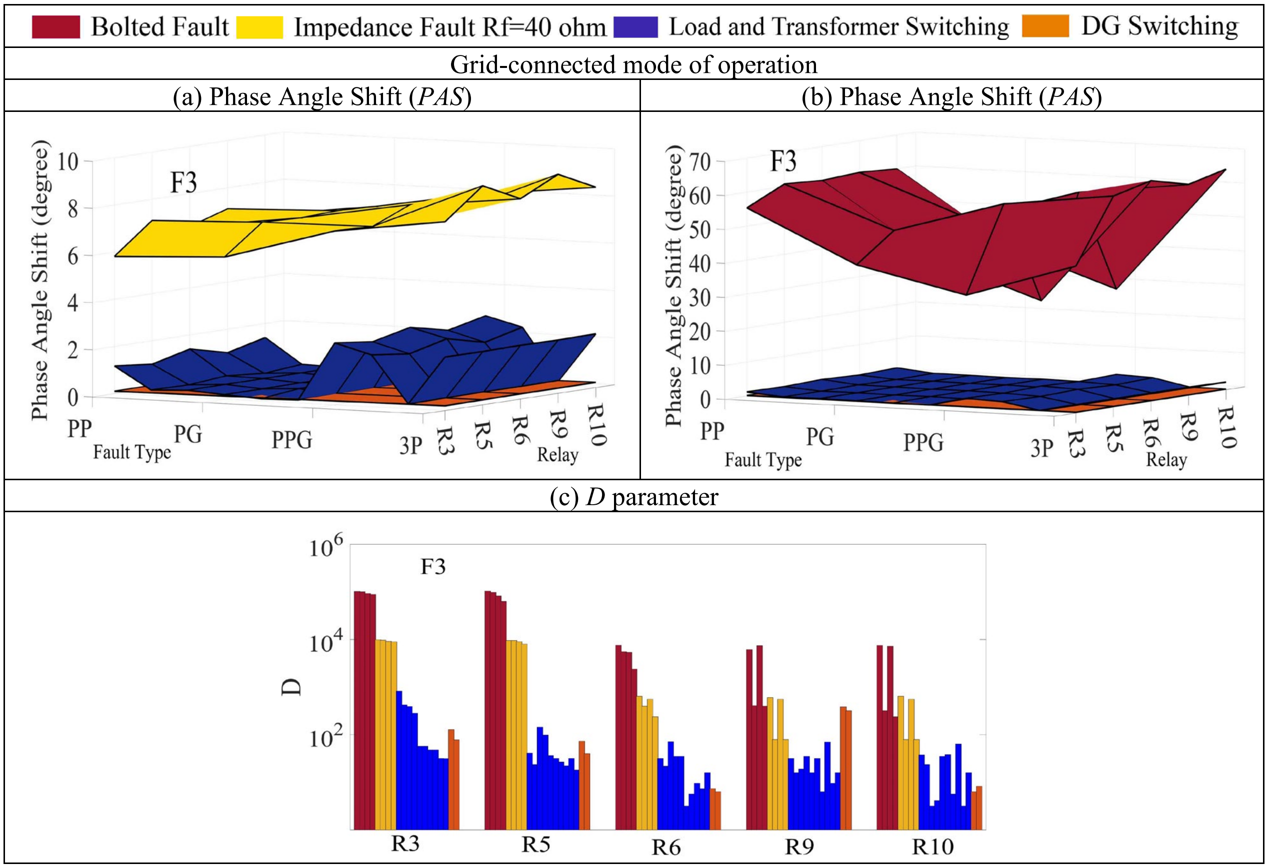

Figure 5-8: Maximum voltage *PAS* and *D* parameter measured by relays for the switching and fault scenarios - Grid-connected mode

Table 5-13: Maximum voltage PAS and D parameter measured by relays for the switching and fault scenarios- Grid mode

	Parameter	Load Switching				Impedance Fault $R_f = 40$ (PP, PG, PPG, 3P)			
R3	PAS	1.17	0.3	2.63	0.2	5.82	6.034	7.379	8.009
	D	422.4	48	31.68	286.08	8841.6	9096	9936	9640
R5	PAS	1	0.3	2.43	0.22	7.1	7.26	7.32	9.29
	D	23.68	26.88	18.24	99.2	8000	8960	9600	9600
R6	PAS	1.4	0.3	2.8	0.23	6.6	7.2	8	8.5
	D	22.016	5.76	16	35.2	240	560	640	400

Table 5-14: Fault clearing time of the relays in the grid-connected mode

			Bolted Fault				Impedance Fault $R_f = 40$			
			3P	PG	PP	PPG	3P	PG	PP	PPG
F3	Pr	R5	0.0467	0.0492	0.0478	0.0511	0.0529	0.0544	0.0547	0.0556
		R6	0.0452	0.0424	0.0404	0.0429	0.0482	0.0512	0.0547	0.0522
	Ba	R3	0.2066	0.20885	0.2081	0.2059	0.2144	0.21846	0.2127	0.2135
		R9	0.4064	0.4059	0.4060	0.4055	0.4119	0.41440	0.4137	0.4135
		R10	0.6048	0.6068	0.6055	0.6064	0.6120	0.61195	0.6126	0.6129

As an illustration, the primary relays R5 and R6 clear a bolted three-phase fault at point F3 in 0.0467 and 0.0452 seconds after the fault respectively in the grid-connected mode. Also, in case that the fault at point F3 is not cleared by the primary relays, the backup relays R3, R9, and R10 clear the bolted three-phase fault at point F3 in 0.2066, 0.4064, and 0.6048 seconds respectively as depicted in Table 5-14.

5.3.3 The Double Feeder Microgrid

As shown in Figure 3-1, the double feeder microgrid [106] includes a battery energy storage and three wind turbines. The system parameters are shown in Table A-2 in the Appendix section. More information about the double feeder microgrid can be found in section 3.2. In the following subsections, the performance of the proposed method for this system is investigated in the island and grid-connected modes.

5.3.3.1 Island Mode

The switching scenarios shown in Table 4-1 are performed in the island mode of operation, and *PAS* and *D* parameters for each scenario are obtained. Then, based on the procedure explained in section 2.4 and section 2.5.4, the relays' characteristics are obtained. The relays' fault detection characteristics parameters obtained based on the fault detection scheme discussed in section 2.4 are shown in Table 5-15 for the island mode.

Fault scenarios including bolted and impedance (R_f = 40 ohms) PG, PPG, PP, and 3P faults at point F4 are performed in the island mode. Figure 5-9 shows *PAS* and *D* parameters obtained by the relays in the C-HIL setup for the performed fault and switching scenarios. As demonstrated in Figure 5-9, the *PAS* value following a fault is larger than the *PAS* value following a switching event. For example, the minimum *PAS* measured by relay R9 among fault scenarios is 28 degrees,

Table 5-15: Relays' fault detection characteristics parameters – Island mode

Relay	Semi major axis	Semi minor axis	Eigenvector 1	Eigenvector 2	D mean	PAS mean
R9	418.06	11.7	(-1, 0)	(0, -1)	256	4.85
R11	699.24	9.77	(-1, 0.01)	(-0.01, -1)	176.32	4.61
R12	676.44	13.04	(-1, 0.01)	(-0.01, -1)	174.46	5.45
R14	740.35	12.81	(-1, 0.01)	(-0.01, -1)	168.8	4.74
R16	306.01	10.83	(-1, 0.02)	(-0.02, -1)	120.58	4.7

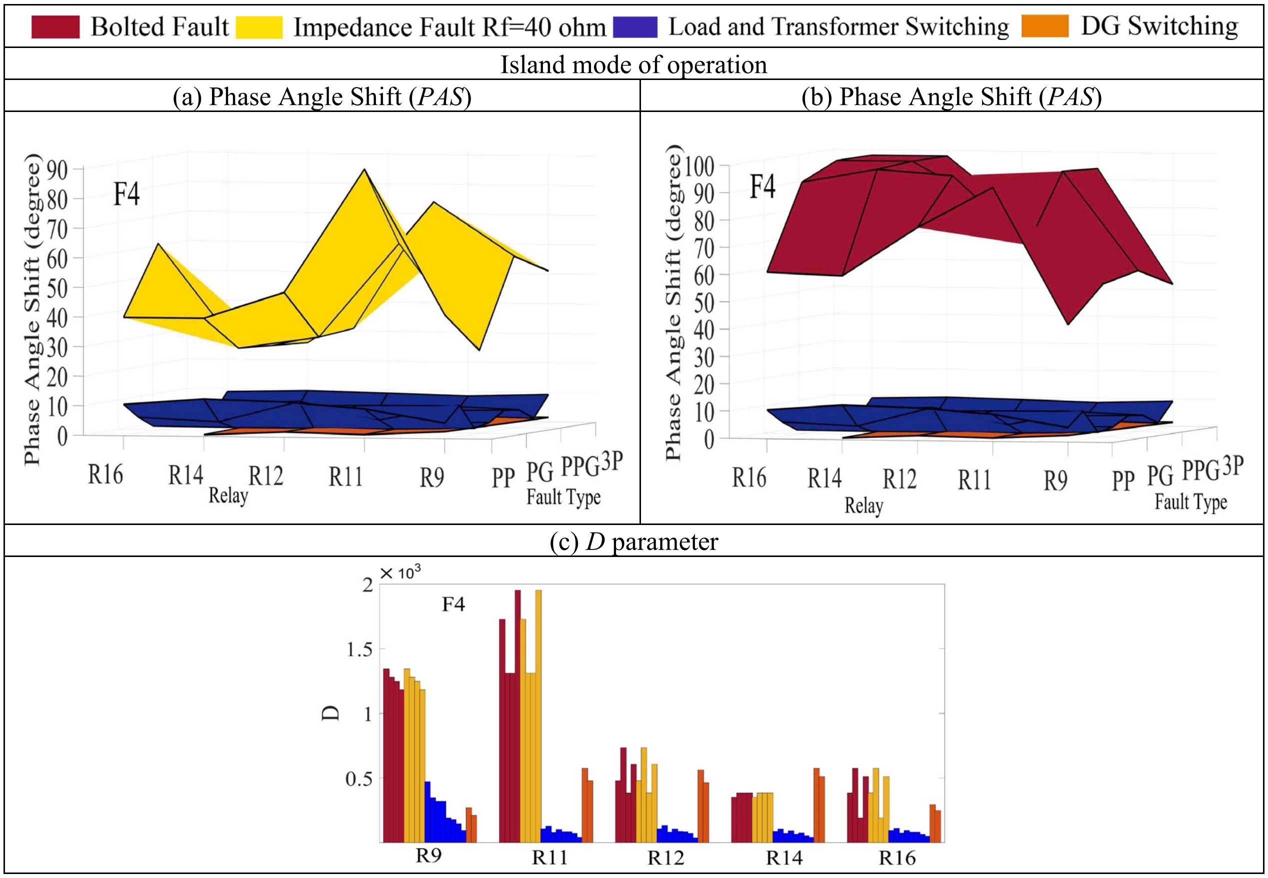

Figure 5-9: Maximum voltage *PAS* and *D* parameter measured by relays for the switching and fault scenarios - Island mode

Table 5-16: Fault clearing time of the relays in the island mode

			Bolted Fault				Impedance Fault $R_f = 40$			
			3P	PG	PP	PPG	3P	PG	PP	PPG
F4	Pr	R11	0.0533	0.0554	0.0494	0.0582	0.0555	0.0577	0.0549	0.0593
		R12	0.0527	0.0461	0.0423	0.0511	0.0533	0.0516	0.0516	0.0511
	Ba	R9	0.4152	0.4162	0.4964	0.4144	0.4152	0.4160	0.4128	0.4144
		R16	1.0152	1.0128	1.0096	1.0136	1.0168	1.0176	1.0136	1.0160
		R14	1.2160	1.2152	1.2136	1.2144	1.2160	1.2168	1.2136	1.2152

and the maximum *PAS* measured by R9 among switching scenarios is 10.5 degrees as Figure 5-9 demonstrates. Table 5-16 shows the fault clearing time of the relays in the island mode based on the fault detection scheme discussed in section 2.4 and by employing the proposed relay shown in Figure 4-1. As an illustration, the primary relays R11 and R12 clear a bolted three-phase fault at point F4 in 0.0533 and 0.0527 seconds after the fault, respectively as depicted in Table 5-16. In addition, if the primary relays do not clear the fault at point F4 for any reason such as breaker failure, the backup relays R9, R16, and R14 clear the bolted three-phase fault at point F4 in 0.4152, 1.0152, and 1.2160 seconds after fault, respectively.

5.3.3.2 Grid-connected Mode

In the grid-connected mode, the microgrid is connected to a 120kV main grid bus bar with 700 MVA short circuit capacity. The switching scenarios shown in Table 4-1 are performed, and *PAS* and *D* parameters for each scenario are obtained. Then, based on the procedure explained in section 2.4 and section 2.5.4, the relays' characteristics are obtained. The relays' fault detection characteristics parameters obtained based on the fault detection scheme discussed in section 2.4 are shown in Table 5-17 for the grid-connected mode.

Several fault scenarios including bolted and impedance ($R_f = 40$ ohms) PG, PPG, PP, and 3P faults at point F4 are performed in the grid-connected mode. Figure 5-10 shows *PAS* and *D* parameters obtained by the relays in the C-HIL setup for the performed fault and switching scenarios. There is a margin between *PAS* parameter obtained for fault conditions and *PAS* parameter obtained for switching events. Therefore, the obtained C-HIL results verified the results obtained by the simulation as shown in Figure 5-10. As an illustration, the minimum *PAS* value measured by R9 is 6 degrees among fault scenarios, and the maximum *PAS* value measured by R9 among switching scenarios is 2.2 degrees in the grid-connected mode of operation as shown in Figure 5-10.

Table 5-17: Relays' fault detection characteristics parameters – Grid mode

Relay	Semi major axis	Semi minor axis	Eigenvector 1	Eigenvector 2	D mean	PAS mean
R9	4300.57	3.64	(-1, 0)	(0, -1)	689.01	1.9
R11	4300.57	2.2	(-1, 0)	(0, -1)	689.01	1.39
R12	599.45	2.38	(-1, 0)	(0, -1)	90.74	1.14
R14	316.6	2.29	(-1, 0)	(0, -1)	53.3	1.29
R16	318.86	2.44	(-1, 0)	(0, -1)	57.67	1.26

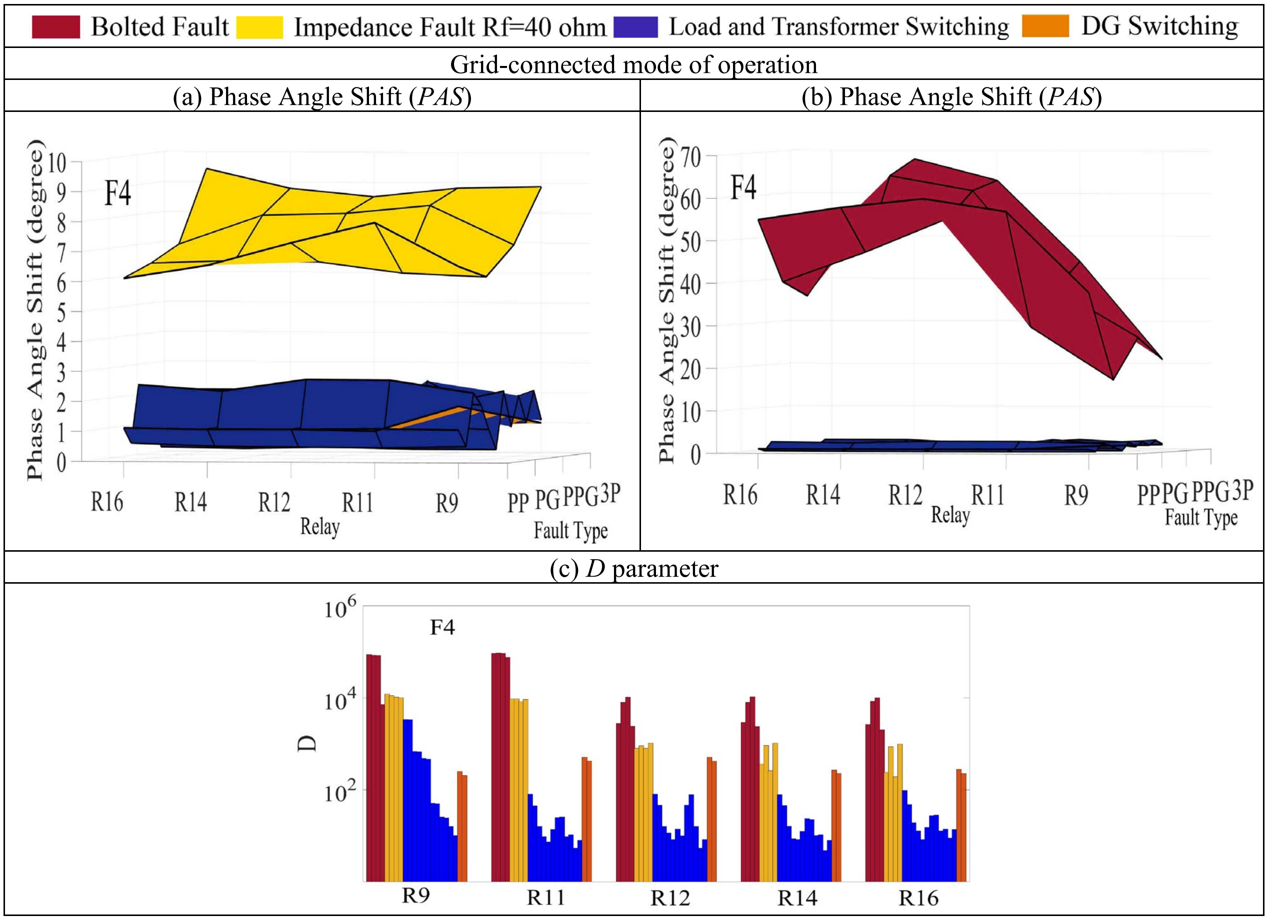

Figure 5-10: Maximum voltage *PAS* and *D* parameter measured by relays for the switching and fault scenarios- Grid-connected mode

Table 5-18: Fault clearing time of the relays in the grid-connected mode

			Bolted Fault				Impedance Fault $R_f = 40$			
			3P	PG	PP	PPG	3P	PG	PP	PPG
F4	Pr	R11	0.0456	0.0461	0.0449	0.0441	0.0527	0.0533	0.0533	0.0538
		R12	0.0406	0.0390	0.0423	0.0390	0.0461	0.0505	0.0456	0.0471
	Ba	R9	0.4048	0.4072	0.4072	0.4048	0.4072	0.4080	0.4080	0.4080
		R16	1.0056	1.0048	1.0056	1.0064	1.0104	1.0128	1.0112	1.0104
		R14	1.2048	1.2049	1.2047	1.2050	1.2104	1.2120	1.2104	1.2104

Table 5-18 shows the fault clearing time of the relays in the grid-connected mode based on the fault detection scheme discussed in section 2.4 and by employing the proposed relay shown in Figure 4-1. As an example, the primary relays R11 and R12 clear a bolted three-phase fault at point F4 in 0.0456 and 0.0406 seconds after the fault respectively in the grid-connected mode. Also, if the fault at point F4 is not cleared by the primary relays, the backup relays R9, R16, and R14 clear the bolted three-phase fault at point F4 in 0.4048, 1.0056, and 1.2048 seconds after the fault respectively as depicted in Table 5-18.

5.4 Comparison of the Simulation Results and C-HIL Results

In this section, the simulation results and the results obtained in the C-HIL setup for the double feeder microgrid (shown in Figure 3-1) [106] are compared. As mentioned, the sampling frequency for the C-HIL results is 33 samples per cycle (1.97 kHz). The sampling frequency for the simulation results presented in chapters 2 to 4 is 333 samples per cycle (19.98kHz). To compare the simulation results and the C-HIL results, the simulation results are obtained again with 33 samples per cycle (1.97 kHz).

Figure 5-11 and Figure 5-12 compare *PAS* and *D* parameters obtained using simulation and the C-HIL setup for bolted faults (BF) at point F4, impedance faults with $R_f = 40$ ohms (IF) at point F4, Load and DG Switching (LS) events in the island and grid-connected mode, respectively. As an illustration, the *PAS* value measured by R11 for a bolted PPG fault in the grid-connected mode at point F4 (shown in Figure 3-1) is 42 degrees obtained through simulation and 44 degrees obtained through C-HIL as Figure 5-12(a) shows; the *D* parameter measured by R11 for a bolted PPG fault in the grid-connected mode at point F4 (shown in Figure 3-1) is 9.07e4 obtained through simulation and 9.28e4 obtained through C-HIL as shown in Figure 5-12(b). Based on the obtained results, the difference between the simulation results and the C-HIL results is in the margin of 5 percent.

Island mode of operation

(a) Phase Angle Shift (*PAS*)

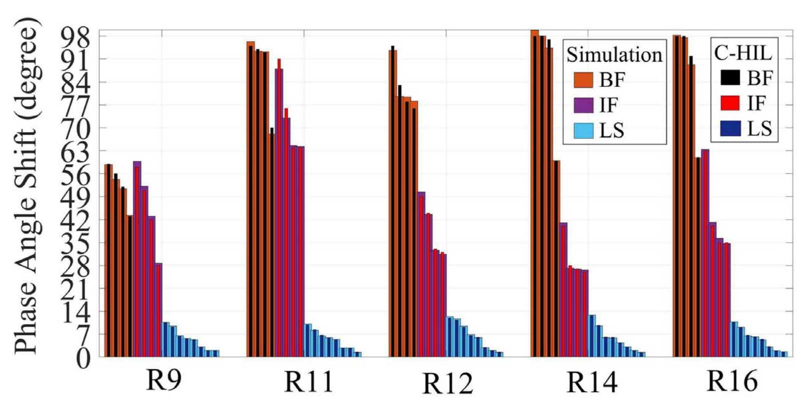

(c) *D* parameter

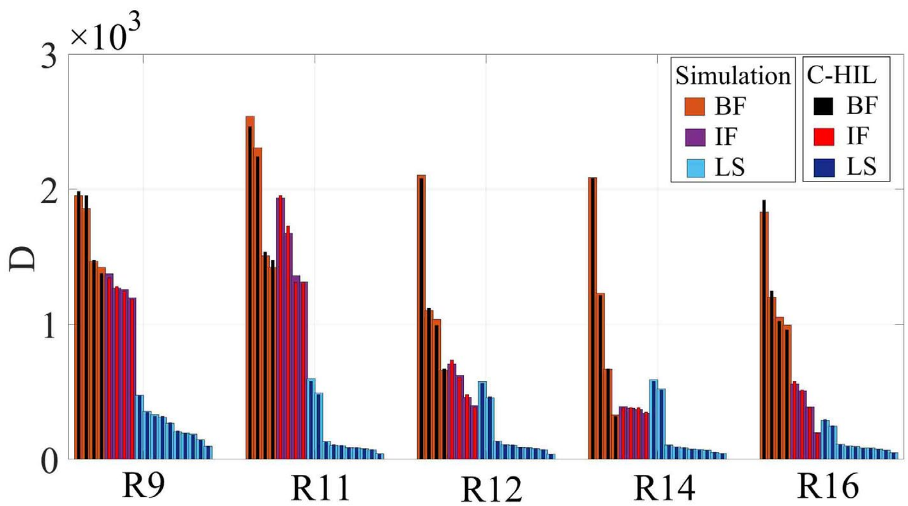

Figure 5-11: Comparison of the *PAS* and *D* parameters measured using simulation and C-HIL in the Island mode

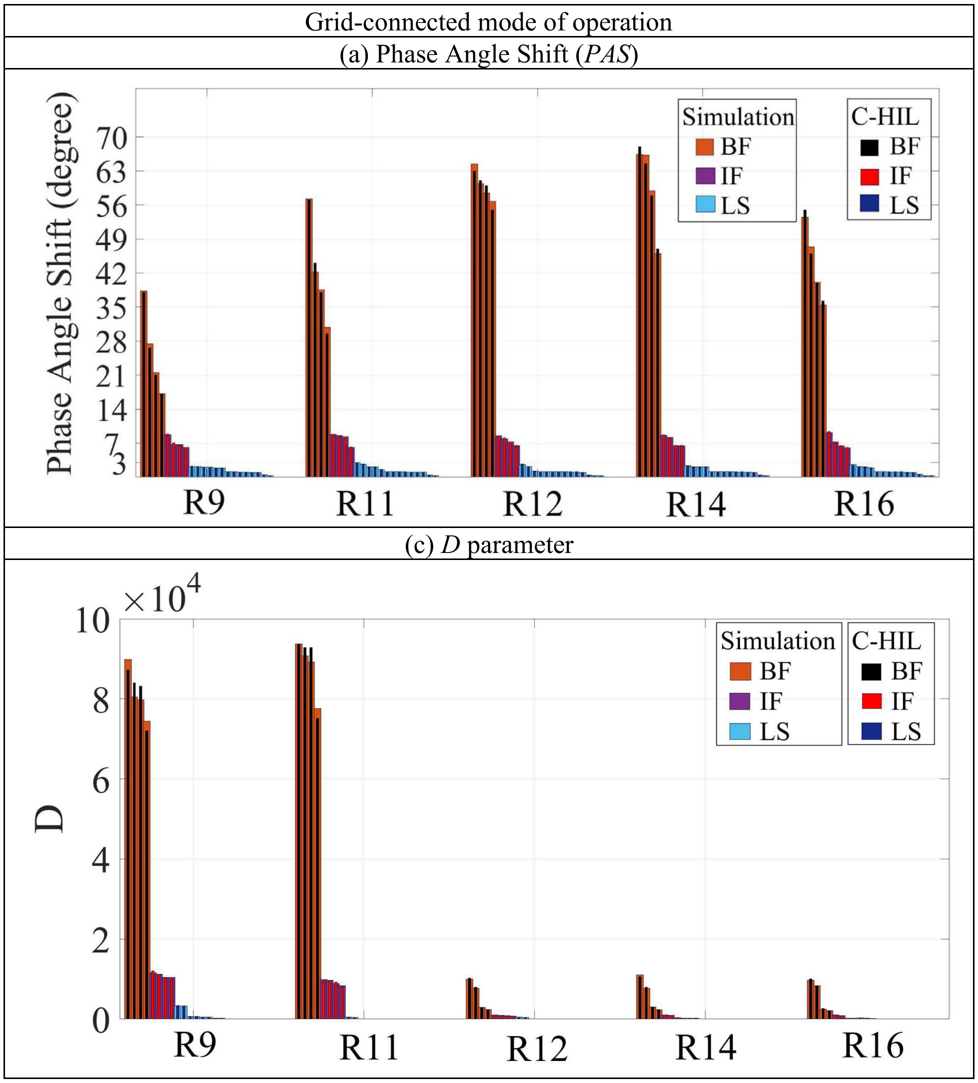

Figure 5-12: Comparison of the *PAS* and *D* parameters measured using simulation and C-HIL in the grid-connected mode

5.5 Comparison of the Proposed Scheme with the Directional Overcurrent Protection (67) and Voltage-restrained Overcurrent Protection (51V)

In this section, 3P, PG, PP, PPG bolted and impedance faults (R_f = 40 ohms) are applied to the double feeder microgrid (shown in Figure 3-1)[106] at point F4, and the fault detection time of the proposed protection scheme is compared with the directional overcurrent protection (67) and voltage restrained overcurrent protection (51V) [4], [136], [137].

Table 5-19 and Table 5-20 compare the fault clearing time of the proposed scheme with directional overcurrent protection (67) and voltage-restrained overcurrent protection (51V) for 3P, PG, PP, PPG bolted and impedance faults ($R_f = 40$ ohms) at point F4 in the island mode. NT in Table 5-19 to Table 5-22 stands for No Trip which means the relay was unable to detect the fault. As Table 5-19 and Table 5-20 demonstrate, the proposed method clears the faults including the impedance faults ($R_f = 40$ ohms) in less than 4 AC cycles with the primary relays in the Island mode. Directional overcurrent protection (67) and voltage restrained overcurrent protection (51V) are mostly unable to detect the fault in the island mode. Although 51V protection shows a better performance as compared to 67 protection for the bolted faults, 51V performance significantly decreases for impedance faults as Table 5-19 and Table 5-20 show.

Regarding the backup protection, the backup relays also detect the faults and operate in a coordinated manner with the primary protection for the bolted and impedance faults in the proposed scheme, whereas 67 and 51V protections are unable to provide backup protection for most of the fault scenarios, especially in case of impedance faults.

Table 5-21 and Table 5-22 also provide the comparison of the proposed scheme's fault clearing time with directional overcurrent protection (67) and voltage restrained overcurrent protection (51V) for 3P, PG, PP, PPG bolted and impedance fault ($R_f = 40$ ohms) at point F4 in the grid-connected mode. As Table 5-21 and Table 5-22 depict, in the proposed method, the bolted and impedance faults with $R_f = 40$ ohms is cleared by the primary relays in less than 4 AC cycles; in addition, in the proposed scheme, the backup relays detect and clear the bolted and impedance

Table 5-19: Primary and backup relays' fault clearing time for bolted faults at point F4 in the island mode

			Proposed protection scheme (Sec)				51 V (Sec)				67 (Sec)			
			3P	PG	PP	PPG	3P	PG	PP	PPG	3P	PG	PP	PPG
F4	Primary	R11	0.0533	0.0554	0.0494	0.0582	0.1534	0.0510	NT	0.0808	NT	0.442	NT	NT
		R12	0.0527	0.0461	0.0423	0.0511	NT	0.321	NT	0.859	NT	NT	NT	NT
	Backup	R9	0.4152	0.4162	0.4964	0.4144	1.839	0.176	NT	0.437	NT	NT	NT	NT
		R16	1.0152	1.0128	1.0096	1.0136	NT	0.440	NT	1.1764	NT	NT	NT	NT
		R14	1.2160	1.2152	1.2136	1.2144	NT	0.520	NT	1.258	NT	NT	NT	NT

Table 5-20: Primary and backup relays' fault clearing time for impedance faults ($R_f = 40$ ohms) at point F4 in the island mode

			Proposed protection scheme (Sec)				51 V (Sec)				67 (Sec)			
			3P	PG	PP	PPG	3P	PG	PP	PPG	3P	PG	PP	PPG
F4	Primary	R11	0.0555	0.0577	0.0549	0.0593	1.427	1.826	NT	1.466	NT	NT	NT	NT
		R12	0.0533	0.0516	0.0516	0.0511	NT	NT	NT	NT	NT	NT	NT	NT
	Backup	R9	0.4152	0.4160	0.4128	0.4144	NT	NT	NT	NT	NT	NT	NT	NT
		R16	1.0168	1.0176	1.0136	1.0160	NT	NT	NT	NT	NT	NT	NT	NT
		R14	1.2160	1.2168	1.2136	1.2152	NT	NT	NT	NT	NT	NT	NT	NT

Table 5-21: Primary and backup relays' fault clearing time for bolted faults at point F4 in the grid-connected mode

			Proposed protection scheme (Sec)				51 V (Sec)				67 (Sec)			
			3P	PG	PP	PPG	3P	PG	PP	PPG	3P	PG	PP	PPG
F4	Primary	R11	0.0456	0.0461	0.0449	0.0441	0.131	0.134	0.142	0.139	0.114	0.106	0.146	0.105
		R12	0.0406	0.0390	0.0423	0.0390	NT	0.277	NT	0.256	NT	NT	NT	NT
	Backup	R9	0.4048	0.4072	0.4072	0.4048	0.266	0.270	0.275	0.261	0.260	0.245	0.313	0.243
		R16	1.0056	1.0048	1.0056	1.0064	NT	0.4	NT	0.370	NT	NT	NT	NT
		R14	1.2048	1.2048	1.2048	1.2048	NT	0.3877	NT	0.3712	NT	NT	NT	NT

Table 5-22: Primary and backup relays' fault clearing time for impedance faults ($R_f = 40$ ohms) at point F4 in the grid-connected mode

			Proposed protection scheme (Sec)				51 V (Sec)				67 (Sec)			
			3P	PG	PP	PPG	3P	PG	PP	PPG	3P	PG	PP	PPG
F4	Primary	R11	0.0527	0.0533	0.0533	0.0538	2.397	NT	3.3	3.01	NT	NT	NT	NT
		R12	0.0461	0.0505	0.0456	0.0471	NT	NT	NT	NT	NT	NT	NT	NT
	Backup	R9	0.4072	0.4080	0.4080	0.4080	NT	NT	NT	NT	NT	NT	NT	NT
		R16	1.0104	1.0128	1.0112	1.0104	NT	NT	NT	NT	NT	NT	NT	NT
		R14	1.2104	1.2120	1.2104	1.2104	NT	NT	NT	NT	NT	NT	NT	NT

faults in a coordinated manner in the grid-connected mode.

The performance of the 51V and 67 protection functions improved in the grid-connected mode for the bolted faults because of the high fault current coming to the microgrid in the grid-connected mode. However, the fault detection problem still exists for 67 and 51V protection functions in the grid-connected mode, especially for the relays that only see the current coming from the DGs like R12, R14, and R16 as Table 5-21 shows. As demonstrated in Table 5-22, 67 and 51V protection functions are unable to detect the impedance fault with $R_f = 40$ ohms in most of the scenarios in the grid-connected mode.

5.6 The Effect of Measurement Accuracy on the Performance of the Proposed Scheme

In this section, the effect of measurement accuracy on the performance of the proposed scheme is investigated in the double feeder microgrid (shown in Figure 3-1) by adding a random error to the voltage and current samples measured by the controller. First, 10%, 15%, and 20% uniform random errors are added to voltage and current samples based on (5-1). In (5-1), $S^{e}_{(in\ pu)}$ is the measured samples with error in per unit; $S_{(in\ pu)}$ is the measured sample in per unit, and ME stands for the value of the measurement error. Second, the voltage and current samples are contaminated with white Gaussian noise with SNR = 25 dB [35], [41].

$$S^{e}_{(in\ pu)} = S_{(in\ pu)} \pm (ME * Rand(0,1)) \tag{5-1}$$

As an illustration, Figure 5-13(a) demonstrates the measured voltage waveform by R9 for 0, 10, 15, and 20% measurement errors and the measured voltage waveform with SNR = 25 dB. Figure 5-13(b) shows *PAS* under normal operating mode corresponding to voltage measurement with different measurement errors along with the *PAS* fault detection threshold values for relay R9. Figure 5-13(c) demonstrates relay R9 characteristic for the grid-connected mode of operation and (*D*, *PAS*) trajectory for different measurement errors. As shown by Figure 5-13(b), the maximum *PAS* error is about 4 degrees whereas the threshold values for fault detection are about 5.5 degrees in the grid-connected mode and 14 degrees in the island mode; as demonstrated by Figure 5-13(c), (*D*, *PAS*) trajectory remains insides the relay characteristic which shows the normal operating area. As a result, the proposed scheme can correctly operate when there is measurement error.

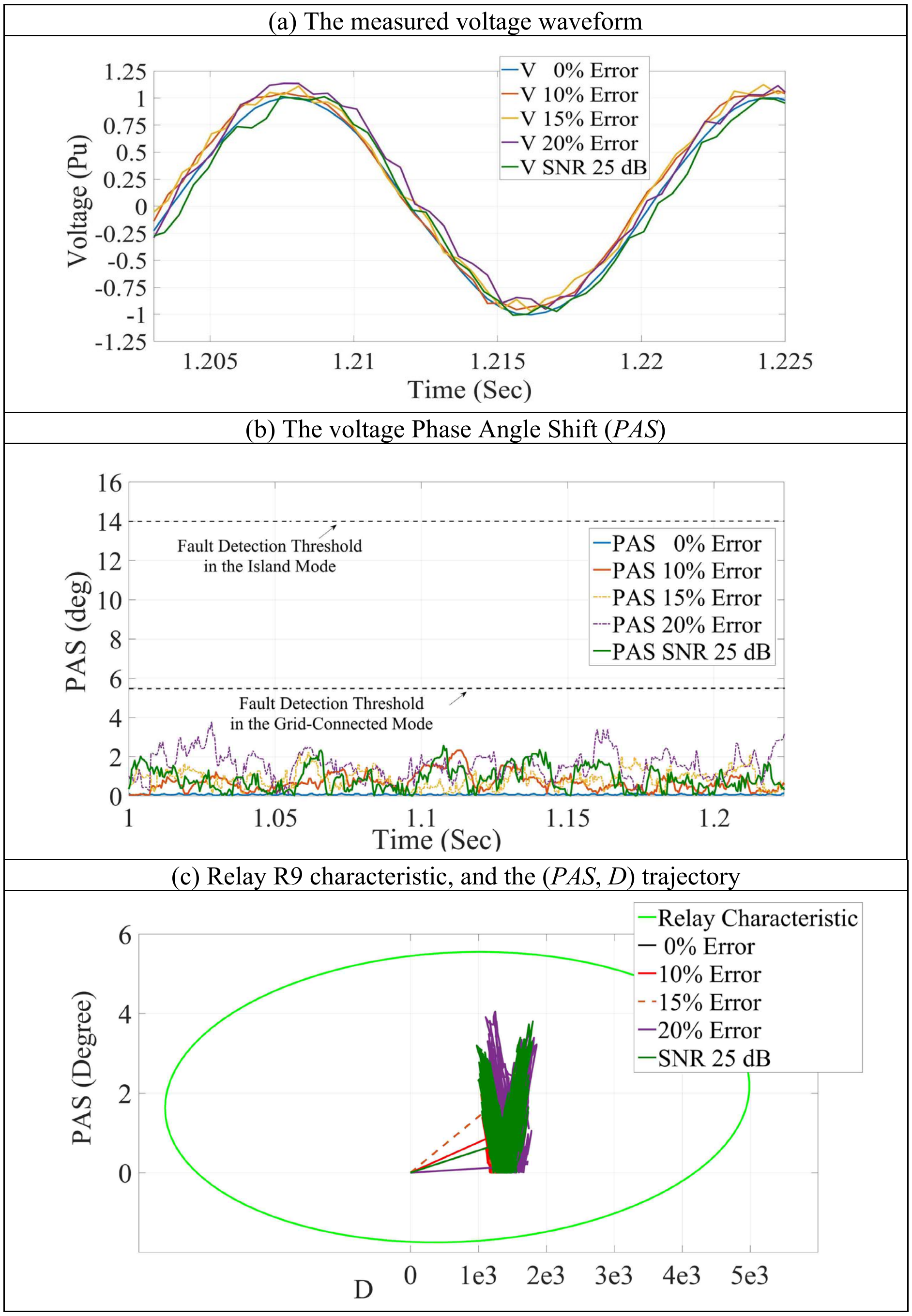

Figure 5-13: a) The measured voltage waveform for 0, 10,15, and 20% measurement error and SNR = 25dB; b) The voltage phase angle shift (*PAS*) under normal operating mode corresponding to voltage measurement with different measurement errors c) Relay R9 characteristic for the grid-connected mode of operation, and the (*D*, *PAS*) trajectory for different measurement errors

5.7 Experimental Measurements for Faults in a Distribution Grid

The experimental results are obtained on a 25 kV distribution test line. The system has two overhead lines which are approximately 100m long. The test line includes a synchronous generator, motors, BES, and controllable RLC load. The BES is 100kWh in total, and it is connected to the system through an inverter. The experimental setup to examine the performance of the proposed protection scheme is shown in Figure 5-14. The experimental setup includes BES and load demonstrated in Figure 5-14. The green cycle in Figure 5-14 shows where the measureme-

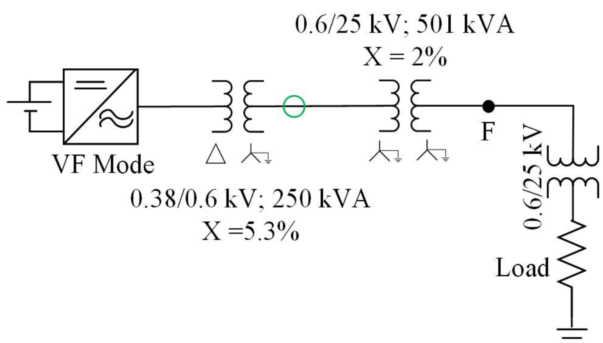

Figure 5-14: Experimental setup © 2021 IEEE [1]

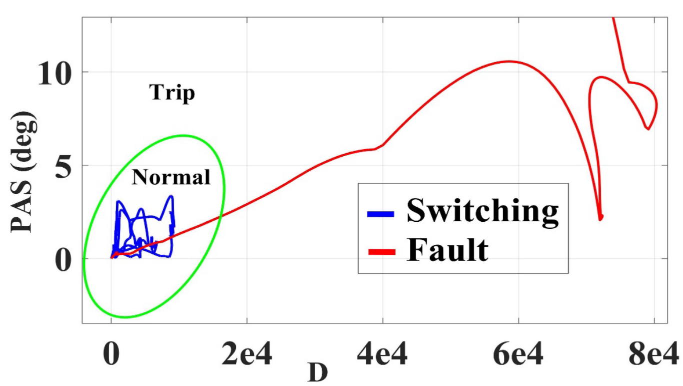

Figure 5-15: Relay characteristic and (*D*, *PAS*) trajectory for the switching and fault scenarios © 2021 IEEE [1]

Table 5-23: *PAS* and *D* for fault and switching scenarios © 2021 IEEE [1]

	PAS (Degrees)	D parameter
Phase to ground fault (PG) at point F	12.94	8.030e04
Load switching (R=100kW)	3.36	9.437e03
Load switching (R=50kW)	1.1	4.428e3
Load switching (C=50kVar)	2.68	6.575e03

-nts are taken. Four scenarios are investigated which include the phase to ground fault, resistive load switching with R= 100kW, R=50kW, and capacitive load switching with C=50kVar. The mentioned scenarios are performed in the island mode, and the inverter is working in VF control mode. The phase-to-ground fault is applied to the system at point F (shown in Figure 5-14) when the inverter is working in full load condition. For the switching scenarios, the load is connected to the inverter when the inverter has no load. The mentioned experiments are performed on the distribution test line, and the voltages and currents data are stored; then, the proposed method is applied to this data, and *PAS* and *D* parameters are calculated in the lab to examine the performance of the method. Figure 5-15 shows the relay characteristic, (D, *PAS*) trajectory for switching scenarios (blue line), and (D, *PAS*) trajectory for the fault scenario (red line). As Figure 5-15 shows, the fault is detected in 4.22 milliseconds after fault; this is the time that (D, *PAS*) trajectory enters the trip area. The *PAS* and *D* values measured for each scenario are shown in Table 5-23. It is worth mentioning that the *PAS* value measured for the worst-case switching scenario R=100kW (equal to the total BES power) is 3.36 degrees which still has a good margin with *PAS*=12.94 degrees measured for the fault scenario [1].

5.8 Limitations of the Proposed protection scheme

In this section, the limitations of the proposed protection scheme are discussed.

The first limitation of the proposed protection method is that its performance against impedance faults decreases in low-voltage distribution systems (distribution systems with 240V to 600V). Figure 5-16 shows power variations with respect to voltage for R=40 ohms. In low-voltage systems, the load impedance becomes comparable to the fault impedance with Rf =40 ohms. For example, a 10kW load has about 36 ohms impedance in a 600 V system whereas the same load power shows an impedance of 62500 ohms in a 25000V system. Therefore, it is not possible to differentiate load switching from impedance faults in low-voltage systems.

The second limitation of the method is the need for offline calculation. Currently, the relay characteristics for the island and grid-connected modes are calculated offline and stored in the relay. However, the relay can be extended in a way that no offline calculation is needed. In that

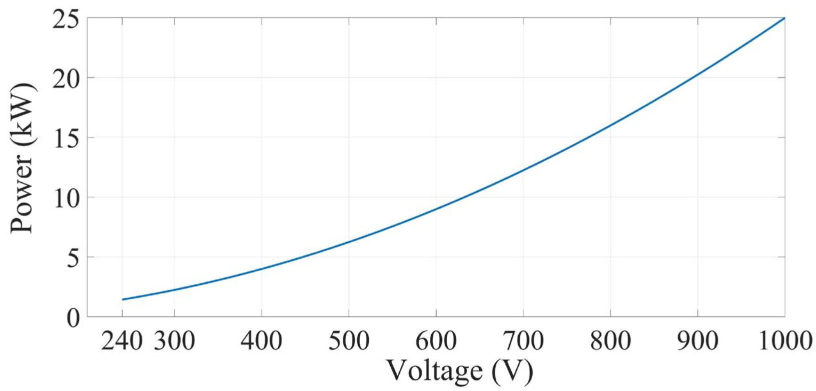

Figure 5-16: Power variations with respect to voltage for R=40 ohms

case, the relay can automatically obtain the fault detection characteristics after performing several load-switching scenarios in the microgrid in the island and grid-connected modes when the relay is installed on the line, and there will be no need to calculate the relay characteristics off-line or performing any simulation studies.

Third, no commercial protection relay is currently capable of performing the calculations required to implement the method. Therefore, the use of a separate controller is necessary to implement the proposed protection scheme.

5.9 Conclusion

In this chapter, the proposed protection relay and the proposed protection scheme were validated in the C-HIL setup. The proposed relay was implemented in an FPGA-based controller and the scheme was tested using a real-time simulator, actual protection relays, and a low-bandwidth communication link. The performance of the proposed scheme was validated for three different microgrid configurations under different scenarios. The C-HIL results closely match the results obtained from the simulation which validate the capabilities of the proposed protection scheme in detecting different types of faults and providing backup protection.

Chapter 6 : Summary and Conclusions

6.1 Thesis Summary

As discussed in chapter 1, the conventional protection schemes are mainly designed based on the behavior of the synchronous generator during faults. In other words, the fault detection process in conventional protection schemes mainly relies on the high current magnitudes that are usually present in conventional distribution systems during faults. However, with the increasing penetration level of the inverter-based renewable energy resources in the distribution system, their limited fault current, and their unconventional behavior in the sequence domain, conventional protection schemes are challenged.

Therefore, the main contribution of this thesis is proposing a protection scheme for microgrids especially microgrids integrating inverter-based DERs that detects the bolted and impedance faults in the island and grid-connected modes.

Since fault detection is an integral part of any protection scheme, a fault detection element is introduced in chapter 2; different system parameters are investigated, and *PAS* and *D* parameters are introduced for fault detection. A fault detection method is designed based on the introduced parameters to detect the fault in the microgrid in both modes of operation. Then, the proposed element is tested under different scenarios using MATLAB Simulink in the second chapter.

In addition to fault detection, determining the fault current direction is also essential in order to have a selective protection scheme in systems with bidirectional power flow like microgrids. As discussed in chapter 1, the conventional directional elements may maloperate in the presence of inverter-based DERs in microgrids. Therefore, a directional element is developed in chapter 3. The proposed directional element employs the current phase shift to determine the current direction under fault conditions. The performance of the proposed directional element is compared with the conventional directional elements under different scenarios in chapter 3.

In chapter 4, the backup protection element and communication element are introduced to have a coordinated protection scheme that can provide backup protection. It is also explained how all these elements work together as a protection relay. A protection scheme that is implemented by the proposed relay is also introduced in chapter 4. The scheme then is tested under different fault scenarios in a microgrid system by using MATLAB Simulink.

Finally, the proposed scheme is validated for three different microgrid systems through Controller-Hardware in the Loop (C-HIL) setup in chapter 5. The microgrid systems are modeled in a real-time simulation platform; the proposed relay is programmed in an FPGA-based controller, and the scheme is implemented using the controller, real-time simulator, protection relays, and serial radio transceivers.

6.2 Conclusions

The main findings and contributions of this thesis are summarized in the following statements:

1. A fault detection element is proposed that detects the faults in microgrids. The fault detection element detects all types of faults including bolted and impedance phase to ground, phase to phase, phase to phase to ground, and three-phase faults. The fault detection time of the proposed fault detection element is much faster than the conventional protection functions such as overcurrent and voltage-restricted overcurrent. The proposed element does not rely on the current level to detect the fault and performs well in the presence of inverter-based DERs in microgrids in the grid-connected and island modes.

2. A directional element is proposed to determine the current direction during fault conditions. The proposed directional element does not rely on the negative sequence current to determine the current direction during fault. Therefore, the proposed element can properly operate in the presence of inverter-based DERs in microgrids where the negative sequence current may be negligible during fault due to the specific fault current characteristics of inverters. It is shown that the proposed element can reliably operate under different scenarios, especially where the conventional directional elements may maloperate.

3. A backup protection element and communication element are proposed, and a protection relay is introduced that defines how all the proposed elements work together. These elements are the fault detection element, directional element, backup protection element, and communication element. Then, a protection scheme implemented by the proposed protection relay is proposed. The proposed scheme can detect all types of faults including impedance faults; it is able to provide backup protection in case of primary relay's breaker failure or communication loss; it can be implemented using a low-bandwidth communication link, and it does not need a relay at every node of the system.

6.3 Recommendation for Future Work

The following areas of interest are recommended for future work:

1. The proposed relay can be extended to be a self-setting relay. Currently, the relay characteristics for the island and grid-connected modes are calculated offline and stored in the relay. However, the relay can be extended in a way that no offline calculation is needed. In that case, the relay can automatically obtain the fault detection characteristics after performing several load-switching scenarios in the microgrid in the island and grid-connected modes when the relay is installed on the line, and there will be no need to calculate the relay characteristics off-line or performing any simulation studies.
2. As discussed in section 5.8, currently the performance of the proposed method against impedance faults decreases in low-voltage distribution systems (distribution systems with 240V to 600V). Improving the performance of the proposed method against impedance faults in low voltage distribution systems can be done as future work.
3. Including an element to detect the open-circuit faults can also be considered in future works as currently the proposed method is not able to detect the open circuit faults.

Appendix. A

A.1: Low voltage distribution feeder

This system is a 600V distribution feeder that can work in the island and grid-connected modes. The feeder includes a 320kW diesel generator, 300kW battery energy storage, 250kW PV, 100kW curtailable load, and 300kW critical load. In the grid-connected mode, the system is connected to a 25kV, 100MVA main grid. The system is demonstrated in Figure 5-4. The system parameters are shown in Table A-1. The microgrid control strategy is based on the Master-slave control strategy; DG 1 (BES) is the Master controller working in Voltage-Frequency (VF) mode, whereas DG2 to DG4 are the slaves working in PQ (active/reactive power) mode. More information on the Master-slave control strategy can be found in [98]. More information on PQ and VF control modes can be found in sections A.4 and A.5 of the Appendix. The inverters' control systems are based on the conventional *dq* (direct-quadrature) control strategy for voltage source converters [98], [99].

Table A-1: Low voltage distribution feeder parameter

Main grid	100 MVA; 25kV	Diesel Generator	320kVA
Grid transformer	12MVA;25/0.6kV; Xt=0.04 pu	Curtailable load	100kVA; pf=1
Battery	300kVA	Critical load	300kVA; pf=1
PV	250kVA; pf=1		

A.2: The double feeder microgrid

This system is a double feeder microgrid inspired by the Canadian urban benchmark distribution system [105]. The double feeder microgrid is shown in Figure 3-1. The system includes three type 4 wind turbines and a Battery Energy Storage (BES). A type 4 wind turbine is a variable-speed wind turbine with a synchronous generator that is connected to the grid through a full-scale power converter. More information on type 4 wind turbine can be found in [126]. Table A-2 shows the system parameters. The microgrid control strategy is based on the Master-slave control strategy; DG 1 (BES) is the Master controller working in Voltage-Frequency (VF) mode, whereas DG2 to DG4 are the slaves working in PQ (active/reactive power) mode. More information on the Master-slave control strategy can be found in [98]. More information on PQ and VF control modes can be found in sections A.4 and A.5. The inverters' control systems are based on the conventional *dq* (direct-quadrature) control strategy for voltage source converters [98], [99]. The system is solidly grounded; the DG transformers configuration are Δ/Yg, and the grid and load transformers configuration are Yg/Yg.

Table A-2: The double feeder microgrid parameters

Main grid	700 MVA; 120kV	DG1	650kVA
Grid transformer	12 MVA;120/25kV; Xt=0.04 pu	DG2	1MVA; pf=1
DG3,4 and load 2,3,4 transformers	500 kVA; 0.6/25kV; Xt=0.05 pu	DG3	250kVA; pf=1
DG1,2 and load 1 transformers	1 MVA; 0.6/25kV; Xt=0.05 pu	DG4	500kVA; pf=1
Lines impedance	0.12+0.383j ohm/km	Load 1	600kVA; pf=1
Length of lines B2B3;B3B4;B1B6;B8B9	1.2 km	Load 2	400kVA; pf=1
Length of lines B1B2;B7B8	1 km	Load 3	300kVA; pf=1
Length of lines B4B5;B6B7	0.8 km	Load 4	450kVA; pf=1

A.3: The modified CIGRE benchmark system

The modified CIGRE benchmark system [100] includes a Battery Energy Storage (BES) and three type 4 wind turbines as shown in Figure 2-8. A type 4 wind turbine is a variable-speed wind turbine with a synchronous generator that is connected to the grid through a full-scale power converter. More information on type 4 wind turbine can be found in [126]. The system parameters are shown in Table A-3. The inverters control systems in the system under study are the conventional *dq* (direct-quadrature) control strategy for voltage source converters [98], [99]. The microgrid control strategy is based on the Master-slave control strategy; DG 1 (BES) is the Master controller working in Voltage-Frequency (VF) mode, whereas DG2 to DG4 are the slaves working in PQ (active/reactive power) mode. More information on PQ and VF control modes can be found in sections A.4 and A.5. More information on the Master-slave control strategy can be found in [98]. The system is solidly grounded; the DG transformers configuration are Δ/Yg, and the grid and load transformers configuration are Yg/Yg.

Table A-3: The modified CIGRE benchmark system parameters (chapter 2)

Main grid	500 MVA; 120kV	DG1	300kVA
Grid transformer	24 MVA;120/25kV; Xt=0.04 pu	DG2, DG3, DG4	250kVA; pf=1
DG and load transformers	500 kVA; 0.6/25kV; Xt=0.05 pu	Load 1	150kVA; pf=1
Lines impedance	0.12+0.383j ohm/km	Load 2	350kVA; pf=1
Length of lines	250 m	Load 3	300kVA; pf=1

A.4. PQ (active/reactive power) control diagram

The control diagram of the PQ control is shown in Figure A- 1 [19] .

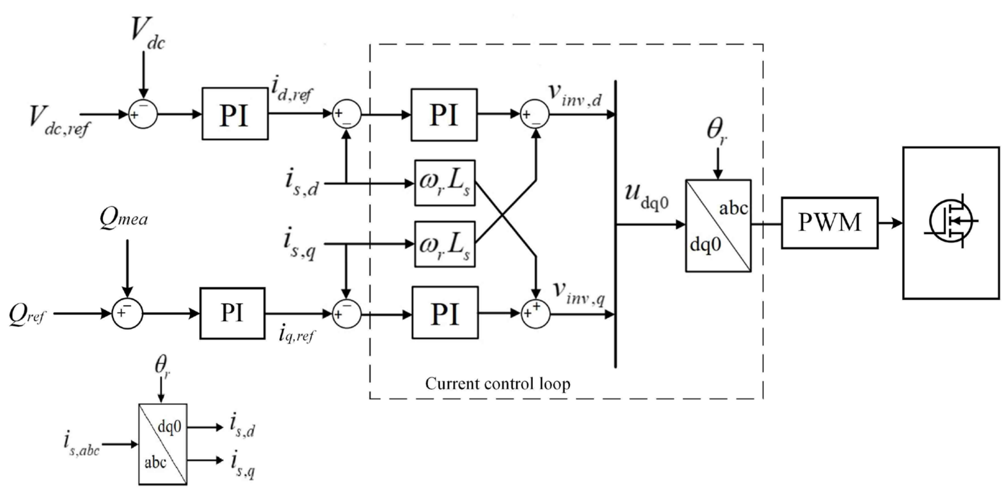

Figure A- 1: PQ (active/reactive power) control diagram

A.5. VF (voltage-frequency) control diagram

The control diagram of the VF control is shown in Figure A- 2 [19].

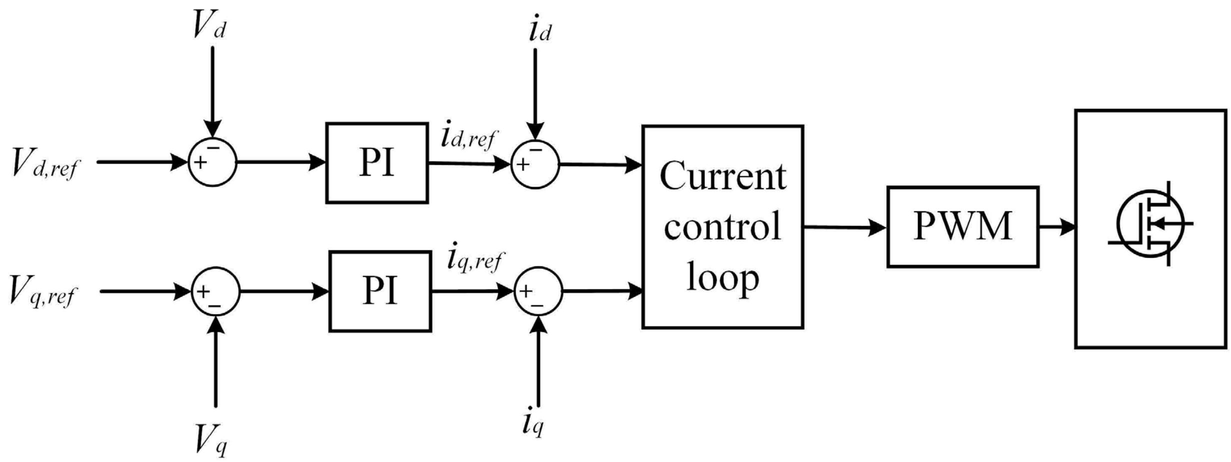

Figure A- 2: VF (voltage-frequency) control diagram

A.6 Research, Software, and Hardware Tools

Research tools:

- Time-domain simulations have been employed to study the fault current characteristics of the inverter-based DERs in different microgrid configurations.
- Linear prediction, a mathematical operation where future values of a discrete-time signal are predicted as a linear function of the previous values, has been employed to obtain a parameter for fault detection.
- Curve fitting, which is the process of constructing a mathematical function or a curve that has the best fit to a series of data points has been employed to design a fault detection characteristic.

Software tools:

The software packages used to perform the aforementioned research are as follows:

- Simulation software and programing: Distribution feeder modeling and data processing.
- Real-time simulation software: Distribution feeder modeling, power hardware-in-the-loop validation of the proposed approach.
- Protection relay software: Setup protection relays and configure the communication link.
- Programing software: Program the real-time and FPGA modules.

Hardware tools:

The hardwares used to perform the aforementioned research are as follows:

- Real-time simulator
- Protection relay
- Serial radio transceiver
- FPGA-based controller

References

[1] E. Dehghanpour, M. Normandeau, G. Joos, and Y. Brissette, "A Protection System for Inverter Interfaced Microgrids," *IEEE Transactions on Power Delivery*, vol. 37, no. 3, pp. 2314–2325, Jun. 2022, doi: 10.1109/TPWRD.2021.3110199.

[2] E. Dehghanpour, M. Normandeau, and G. Joos, "Protection of Inverter Interfaced Microgrids: Challenges and Solutions," in *2022 IEEE/PES Transmission and Distribution Conference and Exposition (T&D)*, IEEE, Apr. 2022, pp. 1–4. doi: 10.1109/TD43745.2022.9817011.

[3] S. S. (Mani) Venkata, M. J. Reno, W. Bower, S. Manson, J. Reilly, and G. W. Sey Jr., "Microgrid Protection: Advancing the State of the Art," Mar. 2019.

[4] A. Hooshyar and R. Iravani, "Microgrid Protection," *Proceedings of the IEEE*, vol. 105, no. 7, pp. 1332–1353, Jul. 2017, doi: 10.1109/JPROC.2017.2669342.

[5] D. Ton and M. A. Smith, "The U.S. Department of Energy's Microgrid Initiative."

[6] R. Lasseter and et al., "White paper on Integration of consortium Energy Resources," *The CERTS MicroGrid Concept, CERTS, Rep. LBNL-50829*, 2002.

[7] M.-T. Kuo and S.-D. Lu, "Design and Implementation of Real-Time Intelligent Control and Structure Based on Multi-Agent Systems in Microgrids," *Energies (Basel)*, vol. 6, no. 11, pp. 6045–6059, Nov. 2013, doi: 10.3390/en6116045.

[8] S. Chowdhury, S. P. Chowdhury, and P. Crossley, *Microgrids and Active Distribution Networks*. Institution of Engineering and Technology, 2009. doi: 10.1049/PBRN006E.

[9] H. M. Sharaf, H. H. Zeineldin, and E. El-Saadany, "Protection Coordination for Microgrids With Grid-Connected and Islanded Capabilities Using Communication Assisted Dual Setting Directional Overcurrent Relays," *IEEE Trans Smart Grid*, vol. 9, no. 1, pp. 143–151, Jan. 2018, doi: 10.1109/TSG.2016.2546961.

[10] M. Mishra and P. K. Rout, “Detection and classification of micro-grid faults based on HHT and machine learning techniques,” *IET Generation, Transmission & Distribution*, vol. 12, no. 2, pp. 388–397, Jan. 2018, doi: 10.1049/iet-gtd.2017.0502.

[11] N. Pogaku, M. Prodanovic, and T. C. Green, “Modeling, Analysis and Testing of Autonomous Operation of an Inverter-Based Microgrid,” *IEEE Trans Power Electron*, vol. 22, no. 2, pp. 613–625, Mar. 2007, doi: 10.1109/TPEL.2006.890003.

[12] W.-M. Guo, L.-H. Mu, and X. Zhang, “Fault Models of Inverter-Interfaced Distributed Generators Within a Low-Voltage Microgrid,” *IEEE Transactions on Power Delivery*, vol. 32, no. 1, pp. 453–461, Feb. 2017, doi: 10.1109/TPWRD.2016.2541344.

[13] J. Keller and B. Kroposki, “Understanding Fault Characteristics of Inverter-Based Distributed Energy Resources,” Jan. 2010. doi: NREL/TP-550-46698.

[14] Z. Shuai, C. Shen, X. Yin, X. Liu, and Z. J. Shen, “Fault Analysis of Inverter-Interfaced Distributed Generators With Different Control Schemes,” *IEEE Transactions on Power Delivery*, vol. 33, no. 3, pp. 1223–1235, Jun. 2018, doi: 10.1109/TPWRD.2017.2717388.

[15] N. D. Tleis, “Power Systems Modelling and Fault Analysis.,” U.K.: Newnes, : Oxford, 2008.

[16] S. F. Zarei, H. Mokhtari, and F. Blaabjerg, “Fault Detection and Protection Strategy for Islanded Inverter-Based Microgrids,” *IEEE J Emerg Sel Top Power Electron*, vol. 9, no. 1, pp. 472–484, Feb. 2021, doi: 10.1109/JESTPE.2019.2962245.

[17] Z. Liang, X. Lin, Y. Kang, B. Gao, and H. Lei, “Short Circuit Current Characteristics Analysis and Improved Current Limiting Strategy for Three-phase Three-leg Inverter under Asymmetric Short Circuit Fault,” *IEEE Trans Power Electron*, vol. 33, no. 8, pp. 7214–7228, Aug. 2018, doi: 10.1109/TPEL.2017.2759161.

[18] Z. Chen, X. Pei, M. Yang, L. Peng, and P. Shi, “A Novel Protection Scheme for Inverter-Interfaced Microgrid (IIM) Operated in Islanded Mode,” *IEEE Trans Power Electron*, pp. 1–1, 2017, doi: 10.1109/TPEL.2017.2769559.

[19] A. Yazdani; and R. Iravani, *Voltage-Sourced Converters in Power Systems: Modeling, Control, and Applications*. Wiley-IEEE Press, 2010.

[20] B. Mahamedi, J. G. Zhu, M. Eskandari, J. E. Fletcher, and L. Li, “Protection of inverter-based microgrids from ground faults by an innovative directional element,” *IET Generation, Transmission & Distribution*, vol. 12, no. 22, pp. 5918–5927, Dec. 2018, doi: 10.1049/iet-gtd.2018.5469.

[21] A. N. Sheta, G. M. Abdulsalam, B. E. Sedhom, and A. A. Eladl, “Comparative framework for AC-microgrid protection schemes: challenges, solutions, real applications, and future trends,” *Protection and Control of Modern Power Systems*, vol. 8, no. 1, p. 24, Dec. 2023, doi: 10.1186/s41601-023-00296-9.

[22] Cooper Power Systems, *Electrical Distribution System Protection* , 3rd ed. Cooper Power Systems , 1990.

[23] IEEE Committee Report, “Application of Protective Relays and Devices to Distribution Circuits,” *IEEE Transactions on Power Apparatus and Systems*, vol. 83, no. 10, pp. 1034–1042, Oct. 1964, doi: 10.1109/TPAS.1964.4765937.

[24] Edison Electric Institute and the Bell Telephone System, “Engineering Reports of the Joint Subcommittee on Development and Research,” vol. 4, no. Report No. 39, 1937.

[25] Rural Electrification Administration bulletin 61-2, “Guide for Making a Sectionalizing Study on Rural Electric Systems,” 1958.

[26] J. J. Grainger and W. D. Stevenson, *Power system analysis*. New York: McGraw-Hill, 1994.

[27] B. Brusilowicz and N. N. Schulz, “Polarizing Voltage Generating Method for Distance and Directional Protection Elements,” *IEEE Transactions on Power Delivery*, vol. 36, no. 1, pp. 74–83, Feb. 2021, doi: 10.1109/TPWRD.2020.2974737.

[28] X. Liu, M. Shahidehpour, Z. Li, X. Liu, Y. Cao, and W. Tian, “Protection Scheme for Loop-Based Microgrids,” *IEEE Trans Smart Grid*, vol. 8, no. 3, pp. 1340–1349, May 2017, doi: 10.1109/TSG.2016.2626791.

[29] M. A. Zamani, A. Yazdani, and T. S. Sidhu, "A Communication-Assisted Protection Strategy for Inverter-Based Medium-Voltage Microgrids," *IEEE Trans Smart Grid*, vol. 3, no. 4, pp. 2088–2099, Dec. 2012, doi: 10.1109/TSG.2012.2211045.

[30] H. Laaksonen, D. Ishchenko, and A. Oudalov, "Adaptive Protection and Microgrid Control Design for Hailuoto Island," *IEEE Trans Smart Grid*, vol. 5, no. 3, pp. 1486–1493, May 2014, doi: 10.1109/TSG.2013.2287672.

[31] F. Calero, "Rebirth of negative-sequence quantities in protective relaying with microprocessor-based relays," in *57th Annual Conference for Protective Relay Engineers, 2004*, IEEE, 2004, pp. 190–219. doi: 10.1109/CPRE.2004.238492.

[32] A. Haddadi, M. Zhao, I. Kocar, U. Karaagac, K. W. Chan, and E. Farantatos, "Impact of Inverter-Based Resources on Negative Sequence Quantities-Based Protection Elements," *IEEE Transactions on Power Delivery*, vol. 36, no. 1, pp. 289–298, Feb. 2021, doi: 10.1109/TPWRD.2020.2978075.

[33] J. J. Q. Yu, Y. Hou, A. Y. S. Lam, and V. O. K. Li, "Intelligent Fault Detection Scheme for Microgrids With Wavelet-Based Deep Neural Networks," *IEEE Trans Smart Grid*, vol. 10, no. 2, pp. 1694–1703, Mar. 2019, doi: 10.1109/TSG.2017.2776310.

[34] Y.-Y. Hong and M. T. A. M. Cabatac, "Fault Detection, Classification, and Location by Static Switch in Microgrids Using Wavelet Transform and Taguchi-Based Artificial Neural Network," *IEEE Syst J*, vol. 14, no. 2, pp. 2725–2735, Jun. 2020, doi: 10.1109/JSYST.2019.2925594.

[35] S. Baloch, S. S. Samsani, and M. S. Muhammad, "Fault Protection in Microgrid Using Wavelet Multiresolution Analysis and Data Mining," *IEEE Access*, vol. 9, pp. 86382–86391, 2021, doi: 10.1109/ACCESS.2021.3088900.

[36] D. P. Mishra, S. R. Samantaray, and G. Joos, "A Combined Wavelet and Data-Mining Based Intelligent Protection Scheme for Microgrid," *IEEE Trans Smart Grid*, vol. 7, no. 5, pp. 2295–2304, Sep. 2016, doi: 10.1109/TSG.2015.2487501.

[37] J. Gao, X. Wang, X. Wang, A. Yang, H. Yuan, and X. Wei, "A High-Impedance Fault Detection Method for Distribution Systems Based on Empirical Wavelet Transform and

Differential Faulty Energy," *IEEE Trans Smart Grid*, pp. 1–1, 2021, doi: 10.1109/TSG.2021.3129315.

[38] S. A. Saleh, R. Ahshan, M. S. Abu-Khaizaran, B. Alsayid, and M. A. Rahman, "Implementing and Testing d–q WPT-Based Digital Protection for Microgrid Systems," *IEEE Trans Ind Appl*, vol. 50, no. 3, pp. 2173–2185, May 2014, doi: 10.1109/TIA.2013.2290814.

[39] S. A. Saleh, "Signature-Coordinated Digital Multirelay Protection for Microgrid Systems," *IEEE Trans Power Electron*, vol. 29, no. 9, pp. 4614–4623, Sep. 2014, doi: 10.1109/TPEL.2013.2285978.

[40] T. S. Abdelgayed, W. G. Morsi, and T. S. Sidhu, "A New Approach for Fault Classification in Microgrids Using Optimal Wavelet Functions Matching Pursuit," *IEEE Trans Smart Grid*, vol. 9, no. 5, pp. 4838–4846, Sep. 2018, doi: 10.1109/TSG.2017.2672881.

[41] S. Baloch and M. S. Muhammad, "An Intelligent Data Mining-Based Fault Detection and Classification Strategy for Microgrid," *IEEE Access*, vol. 9, pp. 22470–22479, 2021, doi: 10.1109/ACCESS.2021.3056534.

[42] R. Azizi and S. Seker, "Microgrid Fault Detection and Classification Based on the Boosting Ensemble Method with the Hilbert-Huang Transform," *IEEE Transactions on Power Delivery*, pp. 1–1, 2021, doi: 10.1109/TPWRD.2021.3109023.

[43] H. Lin, K. Sun, Z. Tan, C. Liu, J. M. Guerrero, and J. C. Vasquez, "Adaptive protection combined with machine learning for microgrids," *IET Generation, Transmission & Distribution*, vol. 13, no. 6, pp. 770–779, Mar. 2019, doi: 10.1049/iet-gtd.2018.6230.

[44] T. S. Abdelgayed, W. G. Morsi, and T. S. Sidhu, "Fault Detection and Classification Based on Co-training of Semisupervised Machine Learning," *IEEE Transactions on Industrial Electronics*, vol. 65, no. 2, pp. 1595–1605, Feb. 2018, doi: 10.1109/TIE.2017.2726961.

[45] A. Srivastava and S. K. Parida, "A Robust Fault Detection and Location Prediction Module Using Support Vector Machine and Gaussian Process Regression for AC Microgrid," *IEEE Trans Ind Appl*, vol. 58, no. 1, pp. 930–939, Jan. 2022, doi: 10.1109/TIA.2021.3129982.

[46] Y. Seyedi, H. Karimi, S. Grijalva, J. Mahseredjian, and B. Sanso, "A Supervised Learning Approach for Centralized Fault Localization in Smart Microgrids," *IEEE Syst J*, pp. 1–11, 2021, doi: 10.1109/JSYST.2021.3112710.

[47] M. A. Jarrahi, H. Samet, and T. Ghanbari, "Novel Change Detection and Fault Classification Scheme for AC Microgrids," *IEEE Syst J*, vol. 14, no. 3, pp. 3987–3998, Sep. 2020, doi: 10.1109/JSYST.2020.2966686.

[48] R. Bhargav, C. P. Gupta, and B. R. Bhalja, "Unified Impedance-Based Relaying Scheme for the Protection of Hybrid AC/DC Microgrid," *IEEE Trans Smart Grid*, vol. 13, no. 2, pp. 913–927, Mar. 2022, doi: 10.1109/TSG.2021.3129532.

[49] E. Sortomme, S. S. Venkata, and J. Mitra, "Microgrid Protection Using Communication-Assisted Digital Relays," *IEEE Transactions on Power Delivery*, vol. 25, no. 4, pp. 2789–2796, Oct. 2010, doi: 10.1109/TPWRD.2009.2035810.

[50] S. F. Zarei and M. Parniani, "A Comprehensive Digital Protection Scheme for Low-Voltage Microgrids with Inverter-Based and Conventional Distributed Generations," *IEEE Transactions on Power Delivery*, vol. 32, no. 1, pp. 441–452, Feb. 2017, doi: 10.1109/TPWRD.2016.2566264.

[51] H. K. Zadeh and M. Manjrekar, "A novel IEC 61850-based distribution line/cable protection scheme design," in *2012 IEEE PES Innovative Smart Grid Technologies (ISGT)*, IEEE, Jan. 2012, pp. 1–6. doi: 10.1109/ISGT.2012.6175640.

[52] T. S. Ustun and R. H. Khan, "Multiterminal Hybrid Protection of Microgrids Over Wireless Communications Network," *IEEE Trans Smart Grid*, vol. 6, no. 5, pp. 2493–2500, Sep. 2015, doi: 10.1109/TSG.2015.2406886.

[53] H. Gao, J. Li, and B. Xu, "Principle and Implementation of Current Differential Protection in Distribution Networks With High Penetration of DGs," *IEEE Transactions on Power Delivery*, vol. 32, no. 1, pp. 565–574, Feb. 2017, doi: 10.1109/TPWRD.2016.2628777.

[54] S. Kar and S. Ranjan Samantaray, "A Fuzzy Rule Base Approach for Intelligent Protection of Microgrids," *Electric Power Components and Systems*, vol. 43, no. 18, pp. 2082–2093, Nov. 2015, doi: 10.1080/15325008.2015.1070384.

[55] CIGRE JWG B5/C6.26/CIRED, "Protection of distribution systems with distributed energy resources," Paris, France, 2015.

[56] A. Arunan, T. Sirojan, J. Ravishankar, and E. Ambikairajah, "Real-Time Adaptive Differential Feature-Based Protection Scheme for Isolated Microgrids Using Edge Computing," *IEEE Syst J*, vol. 15, no. 1, pp. 1318–1328, Mar. 2021, doi: 10.1109/JSYST.2020.2986577.

[57] W. T. El-Sayed, E. F. El-Saadany, and H. H. Zeineldin, "Interharmonic Differential Relay With a Soft Current Limiter for the Protection of Inverter-Based Islanded Microgrids," *IEEE Transactions on Power Delivery*, vol. 36, no. 3, pp. 1349–1359, Jun. 2021, doi: 10.1109/TPWRD.2020.3006791.

[58] K. Dubey and P. Jena, "Impedance Angle-Based Differential Protection Scheme for Microgrid Feeders," *IEEE Syst J*, vol. 15, no. 3, pp. 3291–3300, Sep. 2021, doi: 10.1109/JSYST.2020.3005645.

[59] E. Casagrande, W. L. Woon, H. H. Zeineldin, and D. Svetinovic, "A Differential Sequence Component Protection Scheme for Microgrids With Inverter-Based Distributed Generators," *IEEE Trans Smart Grid*, vol. 5, no. 1, pp. 29–37, Jan. 2014, doi: 10.1109/TSG.2013.2251017.

[60] S. Kar, S. R. Samantaray, and M. D. Zadeh, "Data-Mining Model Based Intelligent Differential Microgrid Protection Scheme," *IEEE Syst J*, vol. 11, no. 2, pp. 1161–1169, Jun. 2017, doi: 10.1109/JSYST.2014.2380432.

[61] J. Nsengiyaremye, B. C. Pal, and M. M. Begovic, "Microgrid Protection Using Low-Cost Communication Systems," *IEEE Transactions on Power Delivery*, vol. 35, no. 4, pp. 2011–2020, Aug. 2020, doi: 10.1109/TPWRD.2019.2959247.

[62] S. Chen, N. Tai, C. Fan, J. Liu, and S. Hong, "Sequence-component-based current differential protection for transmission lines connected with IIGs," *IET Generation, Transmission & Distribution*, vol. 12, no. 12, pp. 3086–3096, Jul. 2018, doi: 10.1049/iet-gtd.2017.1507.

[63] T. S. Ustun, C. Ozansoy, and A. Zayegh, “Modeling of a Centralized Microgrid Protection System and Distributed Energy Resources According to IEC 61850-7-420,” *IEEE Transactions on Power Systems*, vol. 27, no. 3, pp. 1560–1567, Aug. 2012, doi: 10.1109/TPWRS.2012.2185072.

[64] H. Wan, K. K. Li, and K. P. Wong, “An Adaptive Multiagent Approach to Protection Relay Coordination With Distributed Generators in Industrial Power Distribution System,” *IEEE Trans Ind Appl*, vol. 46, no. 5, pp. 2118–2124, Sep. 2010, doi: 10.1109/TIA.2010.2059492.

[65] D. Ishchenko, A. Oudalov, and J. Stoupis, “Protection coordination in active distribution grids with IEC 61850,” in *PES T&D 2012*, IEEE, May 2012, pp. 1–6. doi: 10.1109/TDC.2012.6281478.

[66] A. M. El-Zonkoly, “Fault Diagnosis in Distribution Networks with Distributed Generation,” *Smart Grid and Renewable Energy*, vol. 02, no. 01, pp. 1–11, 2011, doi: 10.4236/sgre.2011.21001.

[67] N. K. Sharma and S. R. Samantaray, “PMU Assisted Integrated Impedance Angle-Based Microgrid Protection Scheme,” *IEEE Transactions on Power Delivery*, vol. 35, no. 1, pp. 183–193, Feb. 2020, doi: 10.1109/TPWRD.2019.2925887.

[68] N. Perera, A. D. Rajapakse, and T. E. Buchholzer, “Isolation of Faults in Distribution Networks With Distributed Generators,” *IEEE Transactions on Power Delivery*, vol. 23, no. 4, pp. 2347–2355, Oct. 2008, doi: 10.1109/TPWRD.2008.2002867.

[69] U. Orji *et al.*, “Adaptive Zonal Protection for Ring Microgrids,” *IEEE Trans Smart Grid*, vol. 8, no. 4, pp. 1843–1851, Jul. 2017, doi: 10.1109/TSG.2015.2509018.

[70] H. J. Laaksonen, “Protection Principles for Future Microgrids,” *IEEE Trans Power Electron*, vol. 25, no. 12, pp. 2910–2918, Dec. 2010, doi: 10.1109/TPEL.2010.2066990.

[71] T. Strasser *et al.*, “A Review of Architectures and Concepts for Intelligence in Future Electric Energy Systems,” *IEEE Transactions on Industrial Electronics*, vol. 62, no. 4, pp. 2424–2438, Apr. 2015, doi: 10.1109/TIE.2014.2361486.

[72] R. Jain, D. L. Lubkeman, and S. M. Lukic, “Dynamic Adaptive Protection for Distribution Systems in Grid-Connected and Islanded Modes,” *IEEE Transactions on Power Delivery*, vol. 34, no. 1, pp. 281–289, Feb. 2019, doi: 10.1109/TPWRD.2018.2884705.

[73] T. S. Ustun, C. Ozansoy, and A. Zayegh, “A microgrid protection system with central protection unit and extensive communication,” in *2011 10th International Conference on Environment and Electrical Engineering*, IEEE, May 2011, pp. 1–4. doi: 10.1109/EEEIC.2011.5874777.

[74] H. Beder, B. Mohandes, M. S. El Moursi, E. A. Badran, and M. M. El Saadawi, “A New Communication-Free Dual Setting Protection Coordination of Microgrid,” *IEEE Transactions on Power Delivery*, vol. 36, no. 4, pp. 2446–2458, Aug. 2021, doi: 10.1109/TPWRD.2020.3041753.

[75] E. Dehghanpour, H. Kazemi Karegar, R. Kheirollahi, and T. Soleymani, “Optimal Coordination of Directional Overcurrent Relays in Microgrids by Using Cuckoo-Linear Optimization Algorithm and Fault Current Limiter,” *IEEE Trans Smart Grid*, vol. 9, no. 2, pp. 1365–1375, Mar. 2018, doi: 10.1109/TSG.2016.2587725.

[76] M. Usama, M. Moghavvemi, H. Mokhlis, N. N. Mansor, H. Farooq, and A. Pourdaryaei, “Optimal Protection Coordination Scheme for Radial Distribution Network Considering ON/OFF-Grid,” *IEEE Access*, vol. 9, pp. 34921–34937, 2021, doi: 10.1109/ACCESS.2020.3048940.

[77] M. N. Alam, S. Chakrabarti, and A. K. Pradhan, “Protection of Networked Microgrids using Relays with Multiple Setting Groups,” *IEEE Trans Industr Inform*, pp. 1–1, 2021, doi: 10.1109/TII.2021.3120151.

[78] K. Lai, M. S. Illindala, and M. A. Haj-ahmed, “Comprehensive Protection Strategy for an Islanded Microgrid Using Intelligent Relays,” *IEEE Trans Ind Appl*, vol. 53, no. 1, pp. 47–55, Jan. 2017, doi: 10.1109/TIA.2016.2604203.

[79] H. Muda and P. Jena, “Superimposed Adaptive Sequence Current Based Microgrid Protection: A New Technique,” *IEEE Transactions on Power Delivery*, vol. 32, no. 2, pp. 757–767, Apr. 2017, doi: 10.1109/TPWRD.2016.2601921.

[80] K. Allahdadi, I. Sadeghkhani, and B. Fani, "Protection of Converter-Interfaced Microgrids Using Modified Short-Time Correlation Transform," *IEEE Syst J*, vol. 14, no. 4, pp. 5172–5175, Dec. 2020, doi: 10.1109/JSYST.2020.2975633.

[81] K. O. Oureilidis and C. S. Demoulias, "A Fault Clearing Method in Converter-Dominated Microgrids With Conventional Protection Means," *IEEE Trans Power Electron*, vol. 31, no. 6, pp. 4628–4640, Jun. 2016, doi: 10.1109/TPEL.2015.2476702.

[82] A. Hooshyar and R. Iravani, "A New Directional Element for Microgrid Protection," *IEEE Trans Smart Grid*, vol. 9, no. 6, pp. 6862–6876, Nov. 2018, doi: 10.1109/TSG.2017.2727400.

[83] M. H. Cintuglu, T. Ma, and O. A. Mohammed, "Protection of Autonomous Microgrids Using Agent-Based Distributed Communication," *IEEE Transactions on Power Delivery*, vol. 32, no. 1, pp. 351–360, Feb. 2017, doi: 10.1109/TPWRD.2016.2551368.

[84] S. M. Brahma and A. A. Girgis, "Development of Adaptive Protection Scheme for Distribution Systems With High Penetration of Distributed Generation," *IEEE Transactions on Power Delivery*, vol. 19, no. 1, pp. 56–63, Jan. 2004, doi: 10.1109/TPWRD.2003.820204.

[85] F. Zhang and L. Mu, "A Fault Detection Method of Microgrids With Grid-Connected Inverter Interfaced Distributed Generators Based on the PQ Control Strategy," *IEEE Trans Smart Grid*, vol. 10, no. 5, pp. 4816–4826, Sep. 2019, doi: 10.1109/TSG.2018.2868967.

[86] S. Beheshtaein, R. Cuzner, A. Benigni, M. Savaghebi, and J. M. Guerrero, "A New Communication-less Harmonic-based Protection Architecture for Meshed Microgrids," in *2018 IEEE Energy Conversion Congress and Exposition (ECCE)*, IEEE, Sep. 2018, pp. 502–508. doi: 10.1109/ECCE.2018.8557587.

[87] S. Beheshtaein, R. Cuzner, M. Savaghebi, and J. M. Guerrero, "A New Harmonic-based Protection structure for Meshed Microgrids," in *2018 IEEE Power & Energy Society General Meeting (PESGM)*, IEEE, Aug. 2018, pp. 1–6. doi: 10.1109/PESGM.2018.8585807.

[88] X. Aiming, C. Yang, F. Bin, W. Fengyu, and Z. Yuchen, "An Active Protection Scheme for Microgrids Based on the Harmonic Injection," in *2021 IEEE/IAS Industrial and Commercial Power System Asia (I&CPS Asia)*, IEEE, Jul. 2021, pp. 1104–1109. doi: 10.1109/ICPSAsia52756.2021.9621419.

[89] K. A. Saleh and A. Mehrizi-Sani, "Harmonic Directional Overcurrent Relay For Islanded Microgrids With Inverter-Based DGs," *IEEE Syst J*, vol. 15, no. 2, pp. 2720–2731, Jun. 2021, doi: 10.1109/JSYST.2020.2980274.

[90] K. Saleh, M. A. Allam, and A. Mehrizi-Sani, "Protection of Inverter-Based Islanded Microgrids via Synthetic Harmonic Current Pattern Injection," *IEEE Transactions on Power Delivery*, vol. 36, no. 4, pp. 2434–2445, Aug. 2021, doi: 10.1109/TPWRD.2020.2994558.

[91] A. Banaiemoqadam, A. Hooshyar, and M. A. Azzouz, "A Comprehensive Dual Current Control Scheme for Inverter-Based Resources to Enable Correct Operation of Protective Relays," *IEEE Transactions on Power Delivery*, vol. 36, no. 5, pp. 2715–2729, Oct. 2021, doi: 10.1109/TPWRD.2020.3025878.

[92] Y. Yin, Y. Fu, Z. Zhang, and A. Zamani, "Protection of Microgrid Interconnection Lines Using Distance Relay With Residual Voltage Compensations," *IEEE Transactions on Power Delivery*, vol. 37, no. 1, pp. 486–495, Feb. 2022, doi: 10.1109/TPWRD.2021.3063684.

[93] X. Li, A. Dysko, and G. M. Burt, "Traveling Wave-Based Protection Scheme for Inverter-Dominated Microgrid Using Mathematical Morphology," *IEEE Trans Smart Grid*, vol. 5, no. 5, pp. 2211–2218, Sep. 2014, doi: 10.1109/TSG.2014.2320365.

[94] X. Zheng, Y. Zeng, M. Zhao, and B. Venkatesh, "Early Identification and Location of Short-Circuit Fault in Grid-Connected AC Microgrid," *IEEE Trans Smart Grid*, vol. 12, no. 4, pp. 2869–2878, Jul. 2021, doi: 10.1109/TSG.2021.3066803.

[95] M. A. Redfern and H. Al-Nasseri, "Protection of micro-grids dominated by distributed generation using solid state converters," in *IET 9th International Conference on*

Developments in Power Systems Protection (DPSP 2008), IEE, 2008, pp. 669–673. doi: 10.1049/cp:20080119.

[96] W. Huang, T. Nengling, X. Zheng, C. Fan, X. Yang, and B. J. Kirby, "An Impedance Protection Scheme for Feeders of Active Distribution Networks," *IEEE Transactions on Power Delivery*, vol. 29, no. 4, pp. 1591–1602, Aug. 2014, doi: 10.1109/TPWRD.2014.2322866.

[97] F. Katiraei and et al., "Investigation of Solar PV Inverters Current Contributions during Faults on Distribution and Transmission Systems Interruption Capacity," 2012. [Online]. Available: https://silo.tips/download/investigation-of-solar-pv-inverters-current-contributions-during-faults-on-distr

[98] W. C. S. Shan, L. X. Lin, G. Li, and L. Y. Wei, "A seamless operation mode transition control strategy for a microgrid based on master-slave control," in *the 31st Chinese Control Conference*, 2012, pp. 6768–6775.

[99] J. Rocabert, A. Luna, F. Blaabjerg, and P. Rodríguez, "Control of Power Converters in AC Microgrids," *IEEE Trans Power Electron*, vol. 27, no. 11, pp. 4734–4749, Nov. 2012, doi: 10.1109/TPEL.2012.2199334.

[100] Technical Brochure 575, "Benchmark systems for network integration of renewable and distributed energy resources," 2014.

[101] D. Chhetija, I. Khan, Z. H. Rather, and S. Doolla, "Negative Sequence Power based Fault Detection Scheme for Power Islands during Unbalanced Faults," in *2023 IEEE International Conference on Environment and Electrical Engineering and 2023 IEEE Industrial and Commercial Power Systems Europe (EEEIC / I&CPS Europe)*, IEEE, Jun. 2023, pp. 1–5. doi: 10.1109/EEEIC/ICPSEurope57605.2023.10194733.

[102] M. S. Golsorkhi and D. D.-C. Lu, "A Decentralized Control Method for Islanded Microgrids Under Unbalanced Conditions," *IEEE Transactions on Power Delivery*, vol. 31, no. 3, pp. 1112–1121, Jun. 2016, doi: 10.1109/TPWRD.2015.2453251.

[103] D. Gutierrez-Rojas, I. Demidov, A. Kontou, D. Lagos, S. Sahoo, and P. J. Nardelli, "Operational Issues on Adaptive Protection of Microgrids Due to Cyber Attacks," *IEEE*

Transactions on Circuits and Systems II: Express Briefs, vol. 70, no. 8, pp. 2994–2998, Aug. 2023, doi: 10.1109/TCSII.2023.3245664.

[104] L. Chavarro-Barrera, S. Perez-Londono, and J. Mora-Florez, “An Adaptive Approach for Dynamic Load Modeling in Microgrids,” *IEEE Trans Smart Grid*, vol. 12, no. 4, pp. 2834–2843, Jul. 2021, doi: 10.1109/TSG.2021.3064046.

[105] E. P. Dick and A. Narang, “Canadian urban benchmark distribution systems,” Varennes, Jul. 2005.

[106] W. T. El-Sayed, M. A. Azzouz, H. H. Zeineldin, and E. F. El-Saadany, “A Harmonic Time-Current-Voltage Directional Relay for Optimal Protection Coordination of Inverter-Based Islanded Microgrids,” *IEEE Trans Smart Grid*, vol. 12, no. 3, pp. 1904–1917, May 2021, doi: 10.1109/TSG.2020.3044350.

[107] T. E. Sati, M. A. Azzouz, and M. Shaaban, “Optimal Protection Coordination of Islanded Microgrids Utilizing an Adaptive Virtual Impedance Fault Current Limiter,” *IEEE Trans Ind Appl*, vol. 59, no. 3, pp. 2866–2876, May 2023, doi: 10.1109/TIA.2023.3244176.

[108] T. E. Sati, M. A. Azzouz, and M. F. Shaaban, “Harmonic Dual-Setting Directional Overcurrent Protection for Inverter-Based Islanded Microgrids,” *IEEE Access*, vol. 11, pp. 34630–34642, 2023, doi: 10.1109/ACCESS.2023.3264842.

[109] E. Nasr-Azadani *et al.*, “The Canadian Renewable Energy Laboratory: A testbed for microgrids,” *IEEE Electrification Magazine*, vol. 8, no. 1, pp. 49–60, Mar. 2020, doi: 10.1109/MELE.2019.2962889.

[110] T. E. Sati and M. A. Azzouz, “Optimal Protection Coordination for Inverter Dominated Islanded Microgrids Considering N-1 Contingency,” *IEEE Transactions on Power Delivery*, vol. 37, no. 3, pp. 2256–2267, Jun. 2022, doi: 10.1109/TPWRD.2021.3108760.

[111] J. Shi, L. Ma, C. Li, N. Liu, and J. Zhang, “A comprehensive review of standards for distributed energy resource grid-integration and microgrid,” *Renewable and Sustainable Energy Reviews*, vol. 170, p. 112957, Dec. 2022, doi: 10.1016/j.rser.2022.112957.

[112] N. W. A. Lidula and A. D. Rajapakse, “Microgrids research: A review of experimental microgrids and test systems,” *Renewable and Sustainable Energy Reviews*, vol. 15, no. 1, pp. 186–202, Jan. 2011, doi: 10.1016/j.rser.2010.09.041.

[113] P. Basak, S. Chowdhury, S. Halder nee Dey, and S. P. Chowdhury, “A literature review on integration of distributed energy resources in the perspective of control, protection and stability of microgrid,” *Renewable and Sustainable Energy Reviews*, vol. 16, no. 8, pp. 5545–5556, Oct. 2012, doi: 10.1016/j.rser.2012.05.043.

[114] M. E. Baran and I. El-Markaby, “Fault Analysis on Distribution Feeders With Distributed Generators,” *IEEE Transactions on Power Systems*, vol. 20, no. 4, pp. 1757–1764, Nov. 2005, doi: 10.1109/TPWRS.2005.857940.

[115] B. Kroposki, C. Pink, R. DeBlasio, H. Thomas, M. Simões, and P. K. Sen, “Benefits of Power Electronic Interfaces for Distributed Energy Systems,” *IEEE Transactions on Energy Conversion*, vol. 25, no. 3, pp. 901–908, Sep. 2010, doi: 10.1109/TEC.2010.2053975.

[116] “IEEE Standard for Interconnection and Interoperability of Distributed Energy Resources with Associated Electric Power Systems Interfaces,” *in IEEE Std 1547-2018 (Revision of IEEE Std 1547-2003)* , Apr. 2018.

[117] “Technical Connection Rules for Medium-Voltage (VDE-AR-N 4110),” 2018.

[118] P. C. Mahalanobis, “On the generalized distance in statistics,” *The Indian Journal of Statistics*, vol. 2, no. 1, pp. 49–55, 1936.

[119] M. H. Bollen, *Understanding Power Quality Problems: Voltage Sags and Interruptions*. Wiley-IEEE Press, 2000.

[120] S. Djoki, J. V. Milanovi, and S. M. Rowland, “Advanced voltage sag characterisation II: point on wave,” *IET Generation, Transmission & Distribution*, vol. 1, no. 1, p. 146, 2007, doi: 10.1049/iet-gtd:20050434.

[121] S. Djoki and J. V. Milanovi, “Advanced voltage sag characterisation. Part I: Phase shift,” *IEE Proceedings - Generation, Transmission and Distribution*, vol. 153, no. 4, p. 423, 2006, doi: 10.1049/ip-gtd:20050350.

[122] R. M. Gardner and Y. Liu, “Generation-Load Mismatch Detection and Analysis,” *IEEE Trans Smart Grid*, vol. 3, no. 1, pp. 105–112, Mar. 2012, doi: 10.1109/TSG.2011.2165566.

[123] Cai Xiaochen, Wang Li, Sun Qiangang, and Meng Zhen, “AC arc fault detection based on Mahalanobis Distance,” in *2012 15th International Power Electronics and Motion Control Conference (EPE/PEMC)*, IEEE, Sep. 2012, p. DS3b.13-1-DS3b.13-6. doi: 10.1109/EPEPEMC.2012.6397333.

[124] S. Nourollah, F. Aminifar, and G. B. Gharehpetian, “A Hierarchical Regionalization-Based Load Shedding Plan to Recover Frequency and Voltage in Microgrid,” *IEEE Trans Smart Grid*, vol. 10, no. 4, pp. 3818–3827, Jul. 2019, doi: 10.1109/TSG.2018.2837160.

[125] J. S. Milton and J. Arnold, *Introduction to Probability and Statistics: Principles and Applications for Engineering and the Computing Sciences*, 3rd ed. New York : McGraw-Hill, 1995.

[126] B. Wu, Y. Lang, N. Zargari, and S. Kouro, “Variable-Speed Wind Energy Systems with Synchronous Generators,” in *Power Conversion and Control of Wind Energy Systems*, Hoboken, NJ, USA: John Wiley & Sons, Inc., 2011, pp. 275–316. doi: 10.1002/9781118029008.ch9.

[127] J. A. P. Lopes, C. L. Moreira, and A. G. Madureira, “Defining Control Strategies for MicroGrids Islanded Operation,” *IEEE Transactions on Power Systems*, vol. 21, no. 2, pp. 916–924, May 2006, doi: 10.1109/TPWRS.2006.873018.

[128] D. Costello and K. Zimmerman, “Determining the faulted phase,” in *2010 63rd Annual Conference for Protective Relay Engineers*, IEEE, Mar. 2010, pp. 1–20. doi: 10.1109/CPRE.2010.5469523.

[129] C. D. Ghilani and P. R. Wolf, *Adjustment Computations: Spatial Data Analysis*, 4th ed. Wiley, 2006.

[130] E. Dehghanpour, H. K. Karegar, and R. Kheirollahi, "Under Frequency Load Shedding in Inverter Based Microgrids by Using Droop Characteristic," *IEEE Transactions on Power Delivery*, vol. 36, no. 2, pp. 1097–1106, Apr. 2021, doi: 10.1109/TPWRD.2020.3002238.

[131] P. Mahat, Z. Chen, and B. Bak-Jensen, "Underfrequency Load Shedding for an Islanded Distribution System With Distributed Generators," *IEEE Transactions on Power Delivery*, vol. 25, no. 2, pp. 911–918, Apr. 2010, doi: 10.1109/TPWRD.2009.2032327.

[132] K. Zimmerman and D. Costello, "Fundamentals and improvements for directional relays," in *2010 63rd Annual Conference for Protective Relay Engineers*, IEEE, Mar. 2010, pp. 1–12. doi: 10.1109/CPRE.2010.5469483.

[133] "Relion Protection and Control: 620 Series—Technical Manual," Zürich, Switzerland, Sep. 2016.

[134] I. Megahed, A. Megahed, E. Ramy, and N. Eassa, "Harmonic evaluation of Alexandria distribution network," in *2001 IEEE/PES Transmission and Distribution Conference and Exposition. Developing New Perspectives (Cat. No.01CH37294)*, IEEE, pp. 247–252. doi: 10.1109/TDC.2001.971242.

[135] A. Sallam and O. Malik, *Electric Distribution Systems, Second Edition*. Hoboken, NJ, USA: John Wiley & Sons, Inc., 2018. doi: 10.1002/9781119509332.

[136] "IEEE Standard for Electrical Power System Device Function Numbers, Acronyms, and Contact Designations," *IEEE Std C37.2-2022 (Revision of IEEE Std C37.2-2008)* , pp. 1–63, 2022.

[137] J. Ciufo and A. Cooperberg, *Power System Protection*, vol. Wiley-IEEE Press. Wiley, 2021. doi: 10.1002/9781119847397.